The Thesis Committee for Sean Robert Klavetter
Certifies that this is the approved version of the following thesis:

Internal Crossflow Effects on Turbine Airfoil Film Cooling Adiabatic Effectiveness with Compound Angle Round Holes

APPROVED BY

SUPERVISING COMMITTEE:

Supervisor:

David G. Bogard

Jason E. Dees

Internal Crossflow Effects on Turbine Airfoil Film Cooling Adiabatic Effectiveness with Compound Angle Round Holes

by

Sean Robert Klavetter, B.S.M.E.

Thesis

Presented to the Faculty of the Graduate School of

The University of Texas at Austin

in Partial Fulfillment

of the Requirements

for the Degree of

Master of Science in Engineering

The University of Texas at Austin

May 2014

Dedication

To my family, whose prayers and support have sustained me.

Acknowledgements

Abstract

Internal Crossflow Effects on Turbine Airfoil Film Cooling Adiabatic Effectiveness with Compound Angle Round Holes

Sean Robert Klavetter, M.S.E.

The University of Texas at Austin, 2014

Supervisor: David G. Bogard

Internal crossflow is an important element to actual gas turbine blade cooling; however, there are very few studies in open literature that have documented its effects on turbine blade film cooling. Experiments measuring adiabatic effectiveness were conducted to investigate the effects of perpendicular crossflow on a row of 45 degree compound angle cylindrical film cooling holes. Tests included a standard plenum condition, a baseline crossflow case consisting of a smooth-walled channel, and various crossflow configurations with ribs. The ribs were angled to the direction of prevailing internal crossflow at 45 and 135 degrees and were positioned at different locations. Experiments were conducted at a density ratio of DR=1.5 for a range of blowing ratios including M=0.5, 0.75, 1.0, 1.5, and 2.0. Results showed that internal crossflow can significantly influence adiabatic effectiveness when compared to the standard plenum condition. The implementation of ribs generally decreased the adiabatic effectiveness when compared to the smooth-walled crossflow case. The highest adiabatic effectiveness measurements were recorded for the smooth-walled case in which crossflow was directed

against the spanwise hole orientation angle. Tests indicated that the direction of perpendicular crossflow in relation to the hole orientation can significantly influence the adiabatic effectiveness. Among the rib crossflow tests, rib configurations that directed the coolant forward in the direction of the mainstream resulted in higher adiabatic effectiveness measurements. However, no other parameters could consistently be identified correlating to increased film cooling performance. It is likely that a combination of factors are responsible for influencing performance, including internal local pressure caused by the ribs, the internal channel flow field, jet exit velocity profiles, and in-hole vortices.

Table of Contents

List of Tables

List of Figures

Nomenclature

<u>Symbols</u>

b	base of surface
C_d	discharge coefficient
d	film cooling hole diameter
D_h	hydraulic diameter
DR	density ratio, ρ_c / ρ_∞
h	convective heat transfer coefficient
I	momentum flux ratio, $(\rho_c U_c)/(\rho_\infty U_\infty)$
k	thermal conductivity
L	film cooling hole length
	or, characteristic length of surface
p	film cooling hole pitch distance
	or, rib pitch distance
$q"$	heat flux
Re	Reynolds number
U	mean velocity
t	thickness of surface
T	temperature
Tu	turbulence level
x	streamwise coordinate distance (x=0 indicates downstream edge of film cooling hole)
y	wall-normal coordinate distance
	or, channel height
z	spanwise-normal coordinate distance

<u>Greek</u>

α	injection angle
β	ratio of orifice diameter to pipe diameter
	or, compound angle
δ	boundary layer thickness
	or, uncertainty
$\delta*$	displacement thickness
η	adiabatic effectiveness
Λ_f	turbulence integral length scale
ρ	density

<u>Subscripts, Accents</u>

$\bar{x}$	lateral average
$\bar{\bar{x}}$	spatial average
aw	adiabatic wall
c	coolant

f	adiabatic surface with coolant
∞	mainstream
	or, freestream
w	wall
0	adiabatic surface without coolant

Chapter One

Introduction and Review of Literature

1.1 GAS TURBINES

Gas turbine engines have fulfilled our country's unceasing demand for an efficient means of power and transport, and their continued technological progression and increased efficiency will ensure they remain an integral part in sustaining our economy. Our society depends on gas turbines in a multitude of every day applications including aeronautical, marine, electrical, and industrial. Gas turbine engines provide thrust for airplanes, turn ship propellers, drive generators for electrical power, and power pumps and compressors. Although these tasks may be accomplished through other portable power systems, namely reciprocating engines, gas turbines have distinct advantages. They have superior power-to-weight ratios, making them ideal for aeronautical and marine applications where weight and space are at a premium. A small dimensional footprint coupled with its high work output similarly makes them more suitable for electrical generation purposes. Depending on the application, turbine engines can be nominally five to twenty times more powerful per unit weight than reciprocating engines. Additionally, they have fewer vibrations and moving parts than a reciprocating engine, reducing unnecessary causes for structural and mechanical failure. Moreover, despite the push for green energy, there remains a need for power on demand that solar and wind cannot currently satisfy. Peak electricity demands, which occur daily and seasonally, can be met more easily and reliably with gas turbines. As a result, gas turbine engines possess the ability to be a key component in society's power and transport sectors for the foreseeable future.

Gas turbines are extremely complex feats of engineering subjected to enormously high temperatures, pressures, and spin rates. Based off the Brayton cycle, they utilize a compressor, combustor, and a turbine which extract the energy from the fuel and convert it to perform useful work. As the gas turbine engine customer has a need to advance the gas turbines in order to meet financial and regulatory constraints, increasing the power output and thermal efficiency is necessary. This can be accomplished by employing any number of different methods of varying degrees of difficulty and feasibility depending upon the customer's gas turbine application. When employed in the power generation sector where room is more readily available to house additional components, gas turbines can recover and re-use energy extracted from the hot exhaust gases. In addition to advancing the engine's design, the Brayton cycle can be improved upon by increasing the pressure ratio or temperature in the compressor stage. In many applications increasing the temperature is the most common and direct way. Consequently, this has pushed the temperatures of the gas exiting the combustor stage well beyond 2000 degrees Fahrenheit, exceeding the capabilities of the turbine blades that receive the air in the subsequent stage. Therefore, one of the main limiting factors for increasing gas turbine efficiency and power is the ability of turbine blades to reduce the heat transfer to the surface in order to withstand these high temperature gases.

There are three general methods employed to protect turbine blades from temperature-based failure. These methods, by themselves, have the ability to allow the turbine blades to withstand significantly higher temperatures; however, they are constrained by their ability to also withstand the high centrifugal loads imposed by the rapidly spinning turbine. Therefore, in order to avoid the failure of turbine blades, a coordinated integration of design, materials, and manufacturing is necessary. To effectively cool the turbine blade, a combination of three general methods is used:

materials science applications using blades made from nickel-based super alloys and ceramic thermal barrier coatings, internal cooling, and external film cooling. Considering the three methods, the interdependence between the latter two is investigated in this thesis. Internal cooling often is accomplished using a series of serpentine passageways within the turbine blade through which coolant flows. Heat is transferred by conduction through the blade, and the coolant in the passageways carries or diffuses heat away from the blade material through the process of convection. Generally, the passageways in the turbine blade are oriented so that internal coolant flows perpendicularly to the mainstream gases. External film cooling is created by establishing a protective layer of cool gas on the blade's surface to shield it from the overlaying hot combustion gases. In order to eliminate variables due to conduction effects, laboratory experiments often consider the blade's surface as adiabatic. The driving potential for film cooling is the temperature difference between the fluid immediately above the adiabatic surface, T_{aw}, and the temperature of the blade's surface, T_w, as seen in the convective heat transfer equation

$$q''_f = h_f(T_{aw} - T_w). \tag{1.1.1}$$

Series of discrete holes through the blade's surface allow coolant within the internal passageways to eject onto the surface to constitute external film cooling. Non-dimensional adiabatic effectiveness is an important parameter when measuring the ability of the jets to protect the surface and can be expressed by

$$\eta = \frac{T_{aw} - T_\infty}{T_c - T_\infty} \tag{1.1.2}$$

where T_∞ represents the hot mainstream gas temperature, and T_c is the temperature of the coolant at the inlet of the hole for an adiabatic surface. Therefore, an η value closer to

3

unity represents a more effective jet as the adiabatic wall temperature is closer to the coolant temperature. However, the effectiveness of film cooling is highly dependent upon the manner in which the coolant ejects out of the holes. Performance is severely degraded when coolant separates from the surface and mixes with the hot external gases. Consequently, the proper design of film cooling maximizes the spreading and adherence of coolant onto the blade's surface.

Both internal and external cooling of turbine blades rely on bleed air produced by the compressor. However, the performances of the compressor and turbine are coupled, as the turbine can divert over half of its power to the compressor which in turn supplies bleed coolant to cool the turbine blades. Therefore, attaining higher exhaust temperatures in order to create more net output power necessitates diverting additional power to the compressor to facilitate the gas turbine blade cooling techniques through the delivery of more bleed coolant. As a result, the power purposed for operating the compressor does not contribute to the useful net output power. Despite this, the overall gas turbine effectiveness gains by using blade cooling methods outweigh the penalty of diverting power to the compressor.

1.2 LITERATURE REVIEW

Testing the effectiveness of blade cooling techniques is extremely costly and difficult under engine operating conditions, and as a result much of the testing is done in scaled laboratory experiments. The number of experiments available in literature reflects the vastness of the combinations of operating conditions, parameters, and dimensions involved in film cooling studies. Many experiments are performed to more accurately replicate real engine conditions, while others quantify the sensitivity of certain parameters in an attempt to make comparisons. For this reason, it is often difficult to

4

exactly compare tests to one another, but an understanding of the relative sensitivity of various parameters can provide a foundation for doing so. The following sections discuss the effects of compound angle holes, internal crossflow, and ribs on film cooling performance.

1.2.1 Compound Angle Hole Effects

A number of experiments have investigated the effects of altering film cooling hole geometries and dimensions in the attempt to maximize film cooling performance. The majority of experiments used cylindrical axial film cooling holes which allow coolant from within the blade to eject onto the blade's surface in a manner oriented co-linearly and in the same direction as the hot mainstream gases. The angle which the coolant is ejected out of the hole, α, may vary for different experiments, but the mainstream tends to deflect the coolant jet back onto the blade's surface. Compound angle holes eject coolant at an angle, β, with respect to the mainstream. Since the mainstream tends to force the upward issuing jet down towards the surface, the additional surface area presented to the mainstream as a result of a compound angle hole promotes the downward force across more of the jet and subsequently enhanced coolant adhesion to the surface. As a result, more coolant can be issued through compound angle holes without sacrificing performance due to additional jet separation, as evidenced by literature discussed later in this section. The amount of coolant forced through the holes may be represented by the mass flux or blowing ratio, M, defined as

$$M = \frac{\rho_c U_c}{\rho_\infty U_\infty}$$
(1.2.1)

However, other non-dimensional variables such as the velocity ratio and momentum flux ratio (Equations 1.2.2 and 1.2.3) can be used by studies instead of blowing ratio to scale

5

experimental conditions to engine conditions or make side-by-side experimental comparisons. Depending on the jet conditions, the velocity ratio, mass flux ratio, or momentum flux ratio may be used to best correlate to the data. The momentum flux ratio is often used to more accurately describe jet separation effects (Sinha (1999)). However, excessively large velocity ratio, blowing ratio, or momentum ratio values result in high velocity jets that penetrate into the mainstream and therefore result in decreased protection of the surface wall.

$$I = \frac{\rho_c U_c^2}{\rho_\infty U_\infty^2} \tag{1.2.2}$$

$$VR = \frac{U_c}{U_\infty} \tag{1.2.3}$$

A number of plenum-fed flat plate studies have been performed to document the beneficial effects of compound angle holes. Flat plate experiments are advantageous when attempting to isolate the performance and foundational physics of film cooling from other factors related to turbine blades, such as pressure gradients, curvature of the blade, or rotational effects. Schmidt et al. (1996) and Sen et al. (1996) conducted flat plate film cooling experiments with 60° compound angle holes to measure the downstream adiabatic effectiveness and heat transfer coefficient enhancement h_f/h_o, where h_f and h_0 are defined as the heat transfer coefficients with and without film cooling, respectively. This quantity is greater than unity, as h_f is greater than h_0 due to increased jet interaction with the mainstream. Coolant emanating from compound angle holes was found to spread significantly more evenly across the surface when compared to axial holes. Even coolant distribution is important because film cooling performance is enhanced by minimizing inefficient local high-velocity jetting, thereby providing greater

6

coverage and reducing unnecessary loss of coolant into the mainstream. Almost no change in laterally averaged adiabatic effectiveness was seen at the lowest blowing ratios tested except for mild improvements in the near-hole region due to increased lateral spreading. Higher blowing ratios yielded significant effectiveness gains for the compound angle holes over axial holes due to the reduction in jet separation from the surface. Although the compound angle holes did produce a more sustained level of high effectiveness over a much larger range of blowing ratios, the study noted that the optimum blowing ratios are at the lower end of those tested in the study where no appreciable effectiveness gains were evidenced. Furthermore the effectiveness gains at high blowing ratios came at the expense of significantly higher heat transfer rates, in some cases to such a degree as to negate the reduction in adiabatic wall temperature and diminish overall film cooling performance. As a result, the authors proposed that film cooling performance could not be accurately represented by the sole presentation of adiabatic effectiveness, but rather by a combination of effectiveness and the heat transfer coefficient as characterized by the Net Heat Flux Reduction (Equation 1.2.4). Ekkad et al. (1997) performed a similar study, investigating the film effectiveness and heat transfer coefficient of 0°, 45°, and 90° compound angle holes using a transient liquid crystal method. Their general findings complemented Schmidt et al. (1996) and Sen et al. (1996), stating that compound angle injection resulted in higher effectiveness levels and produced higher heat transfer coefficients that increased with increasing blowing ratio.

$$NHFR = 1 - \frac{h_f}{h_0}(1 - \eta\theta) \qquad (1.2.4)$$

Ligrani et al. (1994) noted similar increased concentrations of coolant near the surface following 50.5° compound angle cylindrical hole injections, reasoning that the phenomena is derived from the lateral component of momentum from the injectant. Adiabatic effectiveness values were determined through a correlation of measured local Stanton number ratios using a superposition technique (as described in Ligrani et al. (1992)). The augmented concentrations of coolant combined with increased jet spreading in the lateral, or spanwise, direction resulted in significant laterally averaged effectiveness gains when compared to axial holes for x/d<30 in the M=0.50 case and x/d<60 in the M=1.0 and 1.5 cases. Near-hole laterally averaged effectiveness benefits of compound angle injection were substantial, with 41 to 104 percent higher improvements found at a distance of x/d = 6.8 depending on the blowing ratio. It was also evident that, although there were substantially higher levels of effectiveness in the near-hole region, effectiveness values for compound angle holes subsequently dropped off sharply through x/d=30 whereas the axial holes were much more consistent across the full range of x/d. Consequentially, compound angle effectiveness gains were negligible or reversed for x/d>60.

Many authors have studied the vortex structures appearing downstream of the film cooling hole exit and made connections to film cooling performance. One of the first studies to investigate flow structures was Andreopolous and Rodi (1984) who examined a normal jet at high velocity ratio exiting a wall into mainstream crossflow. The existence of a kidney-shaped structure containing counter-rotating vortices was observed about the jet centerline as a result of the incoming mainstream deflecting around the issuing jet. The counter-rotating vortices originated at the jet centerline and moved upward and outward before rotating back down towards the centerline again, entraining some of the hot mainstream gas underneath. This phenomenon is well

documented in literature for axial, cylindrical film cooling holes at various inclination angles. Andreopolous and Rodi (1984) stated that the dominant source of the vortices varied depending upon the velocity ratio. The continuation of vorticity structures within the hole primarily caused the kidney vortices at lower velocity ratios, while interfacial shear between the mainstream and the jet as a result of mismatched velocity gradients generated vortices at high velocity ratios. Coherent unsteadiness was observed in the shear layer by Fawcett et al. (2010), who similarly found a correlation of the blowing ratio rate to the occurrence and sense of rotation of the vortices. However, Andreopolous and Rodi (1984) noted that even the strongest vortices found at the highest velocity ratios were found to decay quickly and eventually turned into weak structures outside of the near-hole region. Pietrzyk et al. (1989) looked at jet-mainstream interaction and found for all blowing ratios tested a wake region downstream of the hole formed by the blockage of the jet. The shear layer formed as a result of the interface of the high velocity jet and the underlying low velocity wake region contained the highest levels of turbulence, an experimentally and computationally documented flow characteristic known to diffuse and dissipate the coolant jet. Consequently this area was susceptible to hot mainstream fluid ingestion, especially for higher blowing ratios. A three-dimensional illustration of jet-mainstream interactions for a normal jet can be found in Figure 1.1.
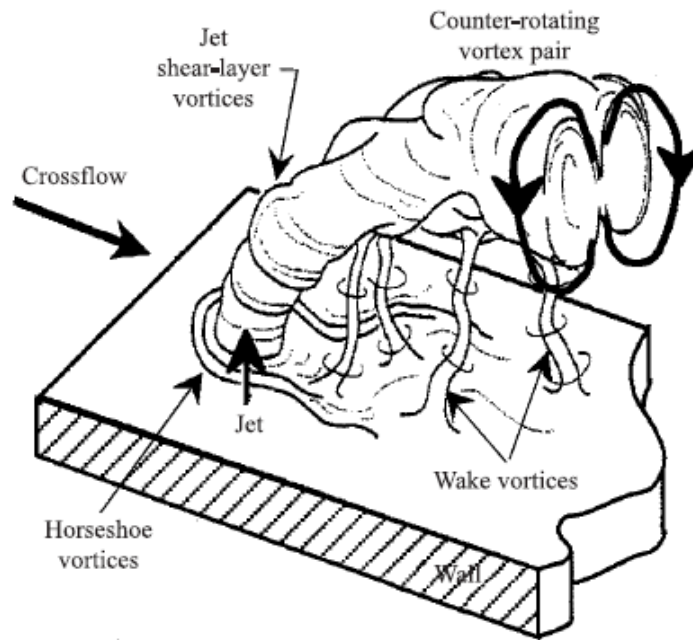
Figure 1.1: Three-dimensional representation of a jet exiting a hole normal to the wall and its downstream flow structures (Peterson, 2003).

The experimental study performed by Pietrzyk et al. was extended by Walters and Leylek (1997) with a computational study, who applied a vorticity-based approach and turbulence models to expand upon film cooling physics. Confirming the Andreopolous and Rodi (1984) study, Walters and Leylek (1997) found that the origins of the observed downstream counter-rotating vortices were attributed to the jet-mainstream shear layers and vorticity structures emanating from within the film hole itself. However, the analysis concluded that the dominant cause was interior film hole vortices. Turbulence models were also used in order to provide insight into the underlying flow physics, and the origins of turbulence were found to be directly related to the severity of the jet-mainstream velocity gradient. Although turbulence levels can negatively affect the coolant jet, the study firmly stated that the counter-rotating vortices were the most significant flow structure mechanisms to degrade film cooling performance despite their inability to exist beyond the near-hole region. Consequently, it was concluded that film

10

cooling performance may be significantly improved by reducing the strength of the counter-rotating vortex pair.

Due to the altered interaction with the mainstream, compound angle jets exhibit different flow structures downstream of the hole. Axial holes produce a pair of symmetric counter-rotating vortices as a result of the direct, collinear interaction of the mainstream with the jet. Compound angle holes inherently skew this interaction as the vortices rotate towards the mainstream, resulting in one of the vortices bearing more of the brunt of the bulk mainstream flow. A computational study by McGovern and Leylek (1997) found that the counter-rotating vortex structure became increasingly asymmetric as the orientation angle increased, eventually collapsing the upstream vortex completely to generate a single large rotating vortex at an orientation angle $\beta=90°$. The extent to which the upstream vortex is weakened by the mainstream depends on both the orientation angle and the blowing ratio. The vortex structure associated with compound angle holes was directly linked to heat transfer augmentation and verified experimentally by Mayhew et al. (2004); however, unlike the supposition made by Walters and Leylek (1997), no direct correlations between the structure and adiabatic effectiveness levels were proposed.

The vortex structures of compound angle holes respond differently to changes in operating conditions than axial holes. Gas turbines operate under high levels of mainstream turbulence which promotes mixing between the mainstream and coolant. A coolant layer adhered to the surface is desirable for higher effectiveness values, so increased interaction between the mainstream and coolant is generally detrimental to film cooling. However, a number of studies including Bons et al. (1994), Schmidt et al. (1996), Mayhew et al. (2002), Saumweber and Schulz (2002), and Kelly and Bogard (2003), found that although higher turbulence levels tend to decrease adiabatic

effectiveness for blowing ratios $M \leq 1.0$ they actually tend to increase effectiveness for blowing ratios $M \geq 1.5$ for both axial and compound holes. This was attributed to the reattachment of separated jets. It should be noted that this increase in effectiveness occurs beyond the range of optimal blowing ratios and is not enough to negate the detrimental effects of jet separation found at elevated blowing ratios. Mayhew et al. (2004) further studied the effects of elevated, 10% mainstream turbulence on coolant structures downstream of a 45° compound angle injection hole and found that high turbulence levels weaken downstream counter-rotating kidney-shaped vortices to a larger degree in compound angle holes than axial holes.

The origin of the influential counter-rotating vortices had been traced by Walters and Leylek (1997) within the film cooling hole, providing implications that changing vortex development within the hole could create favorable structures downstream and allow more coolant to remain closer to the surface. However, Walters and Leylek (1997) was not the first to understand the importance of the flow development inside the cooling hole. A computational study performed by Leylek and Zerkle (1994) examined the entirety of the flow field starting from the plenum source with particular emphasis on the flow development within the film cooling hole. Based off the experimental setup performed by Pietrzyk et al. (1989), the non-dimensionalized length l/d of the cooling hole was set as 3, a more accurate representation of actual turbine blades and a relatively important dimension when considering flow structure development within the hole. A great many early film cooling studies including Crabb et al. (1981), Andreopoulos and Rodi (1984), Kadotani and Goldstein (1979), Le Brocq et al. (1973), Launder and York (1974), and Foster (1980), to name a few, used long coolant supply tubes with l/d values many multiples larger and not necessarily representative of turbine blades. Realizing this disparity, a number of studies including Lutum and Johnson (1999), investigated the

effects of using short hole lengths on film cooling effectiveness and found them to be significant. Leylek and Zerkle (1994) further observed that as a result of the relative proximity of the exit plane of the short cooling hole to its inlet plane, the exit plane conditions are contingent upon the inlet plane conditions. Studies have also consistently shown a strong correlation between the flow field characteristics at the exit plane of the film cooling hole and film cooling results downstream. Therefore, Leylek and Zerkle (1994) concluded that the flow conditions of the entire flow field were dominated by a strong three-way coupling due to the interaction of flow between the plenum, film hole, and jet-mainstream regions. It is therefore important that experiments replicate the coolant inlet conditions found in actual turbine blades, as downstream flow structures associated with film cooling performance are related to the manner in which coolant is delivered into the hole.

1.2.2 Internal Crossflow Effects

Internal coolant crossflow perpendicular to the mainstream alters the flow conditions at the inlet of the film cooling hole and correspondingly affects film cooling performance. All the previously mentioned studies used a quiescent plenum to feed coolant through the film holes, a method not representative of real turbine blade conditions. In order to more accurately depict actual conditions, a number of studies have been performed to examine the effects of internal crossflow on film cooling. One of the first to use internal crossflow in combination with flat plate film cooling was Hay et al. (1983). The discharge coefficient was measured for varying pressure ratios, internal and external Mach numbers, hole inclination angles, hole *l/d*, and internal crossflow directions. Knowing the correct discharge coefficient for film cooling holes is critical to a properly designed turbine, as cooling performance is strongly linked to the flow rate

ejected from the hole. Furthermore, an excess amount of coolant results in unnecessary and efficiency-draining compressor work. The results conclusively showed that the manner in which internal crossflow coolant enters the hole strongly influences the discharge coefficient. Altering the crossflow direction from 0° co-flow to 90° perpendicular flow as well as using 30° and 90° axial hole orientation angles all influenced the coolant attack angle into the hole. The 0° and 90° crossflow directions are studied frequently to simulate the internal cooling schemes of turbine vanes and blades, respectively. Noting some reversed trends when comparing crossflow directions, the authors observed that the discharge coefficient was not as much susceptible to the crossflow direction as it was the internal coolant entrance angle into the hole due to the combination of both crossflow direction and hole inclination. However, the perpendicular crossflow arrangement engendered additional hole losses for both inclination angles as a result of the 90° turn into the hole, negatively affecting the discharge coefficient. This conclusion was verified by Gritsch et al. (2000) and Hay et al. (1983), both of whom noted that the perpendicular crossflow arrangement inherently forced the coolant to make a 90° turn into the hole, as no velocity component of the internal flow is in the same direction as the hole axis. This induces a separation region within the hole on the upstream edge (in relation to the incoming coolant flow) which is very sensitive to and necessarily increases with increasing Mach number, leading to decreased discharge coefficients. This line of investigation was furthered by Gritsch et al. (2001), who examined the effect of compound angle cylindrical holes on film cooling hole discharge coefficients for β=0°, 45°, and 90° in the presence of 0° crossflow. It was found that increasing the orientation angle leads to higher losses in the film cooling hole, especially at the inlet. Similar decreases in the discharge coefficient were found for increasing the hole inclination angle, leading the authors to conclude that the degree by

14

which the coolant turns when it enters the hole dictates the extent of the losses and has a significant impact on the hole's performance.

Flow field, discharge coefficient, and turbulence measurements were taken by Thole et al. (1997) in an investigation of the effects of 0° crossflow on the performance of an axial hole with l/d=6. Measurements were taken throughout the interior of the hole as well as in the external near-hole region, and the internal coolant Mach number was varied for a constant mainstream Mach number. A succession of dependent film cooling events was found; namely that crossflow is related to how the fluid enters the hole, which in turn is linked to how the fluid reacts in the coolant hole by manifestations of separation regions and in-hole turbulence, which is associated with how the coolant exits the hole, which is directly related to the manner in which coolant spreads out onto the blade's surface, which is known to affect the film cooling effectiveness levels. Particular attention was given to the occurrence of separation regions at the inlet of the hole and their effect on the exiting velocity profile. Holes with relatively short l/d ratios are more susceptible to skewed exiting velocity profiles, the existence of which promotes localized penetration into the mainstream, subsequent detachment, and corresponding reduced film cooling effectiveness.

The existence of skewed velocity profiles for very short l/d holes was a significant factor in experiments performed by Hale et al. (2000) and Peterson and Plesniak (2002). The use of 90° inclined holes for alternating co-flow and counter-flow crossflow arrangements showed that although the coolant turning angle into the hole remained the exact same, the interaction of the mainstream with the exiting coolant can significantly alter the exit jet profile as well as the film cooling effectiveness. In agreement with the hypothesis of Pietrzyk et al. (1989) and the computational analysis of Leylek and Zerkle (1994) for plenum fed coolant holes, Thole et al. (1997) observed a separation region on

the downstream side of the cooling hole inlet. This resulted in a skewed exit profile in which the maximum streamwise velocity contours were locations at the top portion of the hole. The existence of high velocity contours at the edges of the hole not only promoted localized penetration into the mainstream but also increased shear due to the larger dU/dy velocity gradients created. This resulted in elevated turbulence levels and detrimental mixing of the coolant with the mainstream which, as Gritsch et al. (1998) similarly found, lead to reduced film cooling effectiveness. The application of internal co-flow crossflow revealed that the in-hole separation regions and velocity contours were sensitive to the crossflow Mach number. As crossflow was applied, the maximum velocity contours moved towards the downstream side of the hole. At the highest internal Mach number tested, a small separation region appeared at the upstream edge of the hole's inlet due to the effectively large turning angle. This skewed the jet exit velocity profile in favor of the downstream edge of the hole and created even more turbulence, as the high velocity jet sheared with the low velocity region downstream of the hole to create even larger dU/dy velocity gradients. As both of the previous two cases had larger coolant turning angles into the hole inlet, the separation regions formed within the hole also created high in-hole turbulence levels and reduced discharge coefficients. However, the study did find an intermediate internal crossflow Mach number that resulted in a jet exit velocity profile more analogous to developed pipe flow, resulting in lower turbulence levels due to reduced dU/dy velocity gradients.

This concept of an optimal internal Mach number for the 0° crossflow arrangement was discussed by Gritsch et al. (2000), who understood the resultant minimization of the separation regions within the hole would cause corresponding minimum losses and a maximum discharge coefficient. However, the findings of Thole et al. (1997), Gristch et al. (2000), and Saumweber and Schulz (2008) conclusively

asserted that the situation for the perpendicular crossflow arrangement is quite different, as maximizing the discharge coefficient would require a minimum internal coolant velocity due to the unchanging nature of the 90° turn the coolant makes when entering the hole. As a consequence, when there is no velocity component of the internal coolant in the direction of the hole axis, as in the case of the application of perpendicular crossflow, there will always result in a decreased discharge coefficient (Hay et al. (1983), Gritsch et al. (2001), Saumweber and Schulz (2008), and Heneka et al. (2010)).

Numerous studies have made it clear that internal crossflow can significantly alter film cooling performance and must be accounted for in proper gas turbine design. Perpendicular crossflow has been shown to increase the film cooling effectiveness for cylindrical holes, the extent of which greatly depends on the internal coolant velocity and velocity ratio. Optimum film cooling effectiveness levels therefore require the correct balance of operating conditions. At low velocity ratios for subsonic conditions, Gritsch et al. (1998, 2003), Peng and Jiang (2011), and Saumweber and Schulz (2008) found that perpendicular crossflow produced either no effect or slight to moderate decreases in laterally averaged effectiveness as compared to the plenum condition. The slight increase in lateral coverage provided by the application of internal crossflow came at the cost of a reduction in the streamwise travel distance of the jets (Gritsch et al. (2003), Saumweber and Schulz (2008)). However. at higher blowing ratios, all studies found significant increases in effectiveness. When 90° crossflow was compared against the plenum condition, Gritsch et al. (1998, 2003) experimentally found slight decreases in laterally averaged effectiveness at the lowest velocity ratio tested but significant gains at higher velocity ratios. Furthermore, the internal crossflow velocity was shown in Gritsch et al. (2003) to influence effectiveness values. A slight 8 percent decrease in laterally averaged effectiveness data was at the lowest velocity ratio tested, VR=0.27, for a coolant-to-

mainstream velocity ratio of $M_c/M_\infty=1$. A gain of about 40 percent was observed at VR=0.54, and increases were found at VR=0.81 and VR=1.08 of about 240 percent. This indicated that the plenum-fed jet detached while a combination of improved lateral spreading and the appearance of separation suppression for the crossflow case allowed more coolant to remain closer to the surface. The significant changes in effectiveness for the different regimes also illustrated the sensitivity to velocity ratio. Despite the well-known sensitivity of cooling performance to the velocity ratio (or blowing and momentum ratio) chiefly due to separation effects, the addition of crossflow makes performance also dependent upon the internal coolant velocity as alluded to in Thole et al. (1997). As a result, Gritsch et al. (2003) further investigated the effects increasing the internal Mach number to attain $M_c/M_\infty=2$. A larger decrease in effectiveness at the lowest velocity ratio VR=0.27 was observed and was nominally a 30 percent loss. A very small gain in laterally averaged effectiveness at VR=0.54 of about 8 percent was found, but significant increases of nominally 300 and 350 percent occurred at VR=0.81 and VR=1.08, respectively. All measurements were within the range $0 \le x/d \le 8$. Similar to the effect of a compound angle hole, the perpendicular crossflow shifted the jet off the centerline, resulting in local maximum effectiveness values occurring on the upstream side of the hole with respect to the direction of the incoming internal coolant. The extent of the shift of effectiveness contours was greatest at low blowing ratios but moved toward the centerline for increasing blowing ratio (Gritsch et al. (1998, 2003), Adami et al. (2002), Saumweber and Schulz (2008)). The reason for this effect was attributed to a combined reflection and swirling motion generated within the hole, as explained by Gritsch et al. (1998) and depicted through in-hole streamlines from a CFD study completed by Adami et al. (2002).

18

Peng and Jiang (2012) numerically studied the effects of 90° crossflow for a coolant-to-mainstream ratio M_c/M_∞=0.5. The study found that the highest disparities in effectiveness for each velocity ratio tested occurred in the near hole region, and the differences decreased rapidly for increasing x/d. In fact, the effectiveness curves converged for x/d>13. The lowest velocity ratio VR=0.42 saw a small loss in effectiveness of nominally 9 percent in the immediate near hole region, but gains of about 75 percent were found for VR=0.83 and VR=1.25.

Saumweber and Schulz (2008) found similar results to both Gristch et al. (1998, 2003) and Peng and Jiang, recording small effectiveness losses for the 90° crossflow case at a low velocity ratio while observing significant gains at higher velocity ratios. A numerical analysis was performed, and results slightly differ quantitatively from Gristch et al. (2003). However, for a coolant-to-mainstream velocity ratio of M_c/M_∞=0.97, a small 6 percent decrease in effectiveness was found at a velocity ratio VR=0.29. Increases in effectiveness of nominally 30 and 100 percent were found for velocity ratios of VR=0.57 and VR=0.86, respectively. The internal coolant crossflow velocity was then altered for a constant mainstream velocity and a velocity ratio of VR=0.57. At the lowest coolant-to-mainstream velocity ratio M_c/M_∞=0.33, a decrease in effectiveness of 30 percent was found when the 90° crossflow case was compared to the plenum condition (compared to the aforementioned 30 percent increase at the same velocity ratio). An increase of about 15 percent was found for M_c/M_∞=0.67, and further increases of nominally 35 to 45 percent were found for coolant-to-mainstream velocity ratios of M_c/M_∞=1.33, 1.67, and 1.97.

An examination of the flow field created by perpendicular crossflow reveals distinct differences from the plenum condition. Foremost, computational studies investigating the velocity contours inside the cylindrical hole show the existence of a

singular rotating or swirling fluid structure (Adami et al. (2002), Peng and Jiang (2011), Saumweber and Schulz (2008), Kohli and Bogard (1997)) in contrast to the counter-rotating vortex pair found within the hole for the plenum case (Saumweber and Schulz (2008), Kohli and Bogard (1997)). The intensity of the singular rotating structure for the crossflow case was dependent upon both the blowing ratio and the internal coolant velocity and determined the effectiveness levels downstream. Increases in the internal coolant velocity increased the swirl velocity, affecting in-hole losses and positively influencing the velocity profile at the exit. The latter was and has previously been shown to govern the jet's interaction with the mainstream, and a consequential increase in lateral distribution on the surface resulted from the increased internal Mach number (Saumweber and Schulz (2008)). A computational analysis conducted by Peng and Jiang (2011) presented a visual representation of this result at M=1.0 comparing the crossflow condition with the plenum condition. Streamlines were shown throughout the course of the hole, and the crossflow case exhibited corkscrew streamlines. These rotated as they moved through the hole and exited in a more dispersed and less tightly bunched manner. The resultant downstream counter-rotational vortices are askew and of different strengths (Peng and Jiang (2011), Saumweber and Schulz (2008)). One of the vortices originated from within the hole as a result of its singular rotating structure, while the other was suggested to have emanated by the induction of vorticity created by the jet-mainstream interaction (Adami et al. (2002)).

1.2.3 Rib Implementation Effects

It is clear that internal crossflow has a significant effect on film cooling performance and that effectiveness levels are sensitive to a number of operating conditions. The feed orientation, with respect to the combination of both the hole axis

and mainstream flow, affects jet characteristics such as trajectory, structural features, and lateral spreading. The data collected as a result of the previous experimental and numerical studies allowed researchers to investigate the foundational physics of crossflow-fed film cooling holes and identify the conditions most likely to produce optimum cooling performance. In order to study the foundational physics of crossflow effects, all the aforementioned studies used smooth walled channels or plenums unimpeded by any interior blockages protruding into the path of the coolant. However, it is common for the internal crossflow passageways in an actual turbine blade to place ribs along the internal walls. The existence of ribs in the serpentine passageways is a secondary mechanism within the internal cooling framework to enhance heat transfer away from the blade's surface by means of increased turbulence and also create more channel surface area for internal heat transfer. Most importantly, the ribs promote turbulence in the passageways, thereby increasing heat transfer rates. As the rib is an obstacle to the oncoming coolant, the flow field within the channel significantly changes. When the coolant approaches a rib, the flow is deflected in a transverse direction and a recirculation region forms against the upstream face. A strong adverse pressure gradient is incurred and forces the fluid to accelerate to pass over the rib, creating a small recirculation region on top of the rib. Due to the abrupt increase of cross sectional area after the rib, an expansion of the fluid occurs and a large third recirculating separation region forms along with a shear layer. The normal flow field can be altered by placing a film cooling hole inside the large recirculation region downstream of the rib. This decreases the size of the recirculation region as flow in the vicinity of the hole is continuously entrained and sucked out. An increase in the blowing ratio or suction ratio of the holes exacerbates this effect and causes earlier flow reattachment (Casarsa and Arts (2005), Cukerel et al. (2013), Kunze and Vogeler (2013)). When considering the

internal flow field's sensitivity to blowing ratio, Kunze and Vogeler (2013) found that the degree of sensitivity was greatest for small internal Reynolds numbers. The flow field effects are drastically reduced at higher Reynolds numbers because the mass fraction of coolant going into the holes is considerably smaller and therefore less susceptible to the effects of the holes.

The structure of the internal flow field as a function of various geometries and operating conditions has a considerable effect on internal cooling performance (Shen et al. (1996), Xiangyun et al. (2013), Cukerel et al. (2013), Han et al. (1985), Chanteloup and Bolcs (2002), Casarsa and Arts (2005)); furthermore as ribs affect the internal flow field, they affect cooling hole inlet conditions and ultimately film cooling performance. Previously mentioned studies have investigated and tried to optimize a great many factors related to cylindrical holes and internal crossflow that influence external performance: arrays of dimensions, angles, geometries, and operating conditions. So, too, have studies concerning ribs. Heneka et al. (2010) used ribs in combination with crossflow (0° and 90°), varying compound angle holes (0°, 45°, and 90°), and different rib positions to measure the discharge coefficient of the holes. The ribs were angled orthogonally to the crossflow fluid. The addition of ribs affected the in-hole separation region and greatly altered the losses depending upon the crossflow direction and hole orientation. A selection of results will be considered. The configuration consisting of 0° crossflow and axial holes resulted in a very significant drop in the discharge coefficient for the ribbed case for all pressure ratios tested. Shifting the holes closer towards the upstream rib, most likely within the recirculation region, caused a further drop in the discharge coefficient. Conversely, shifting them towards the downstream rib increased the discharge coefficient. The configuration consisting of 90° crossflow and axial holes showed very little change in the discharge coefficient for the ribs except for a small loss

22

at very low pressure ratios. However, there was negligible change for the different hole positions. Lastly, both 0° and 90° crossflow configurations paired with 45° compound angle holes resulted in significant discharge coefficient decreases. A decreased discharge coefficient was found when the holes closer to the upstream rib, while an increased discharge coefficient resulted from shifting the holes closer to the downstream rib. Aware of the array of geometrical configuration possibilities, the authors created a discharge coefficient correlation to account for crossflow orientation, hole orientation, and the effect of ribs.

Illustrating the effect of flow field alteration through rib orientation, Sakai and Takahashi (2011) found different results when shifting the holes for the 90° crossflow configuration. Ribs were angled 60° towards ("forward" facing ribs) and against ("backward" facing ribs) the mainstream direction. For both cases in a small pressure ratio range around unity, shifting the holes closer to the upstream rib resulted in lower discharge coefficient values due to the pressure losses caused by recirculation region after the rib. Conversely, shifting hole closer to the downstream rib resulted in a higher discharge coefficient.

Effectiveness values are related to conditions at the hole inlet and therefore similarly affected by the presence of ribs. A series of experimental and numerical studies with 90° crossflow were performed by Sakai and Takahashi (2011), Agata et al. (2012), Agata et al. (2013) in Japan to investigate the influence of different rib configurations on film cooling effectiveness and flow fields. Sakai (2011) obtained spatially averaged effectiveness values for 60° forward and backward facing ribs for $0.4 \leq M \leq 0.7$ and found converging curves. The forward ribs had the highest effectiveness values but decreased with increasing blowing ratio. The backward ribs had the lowest effectiveness values but increased with increasing blowing ratio. This is in agreement with the laterally averaged

data taken by Agata et al. (2012) for the inversion of ribs under similar conditions. Furthermore, an experimental study by Kissel et al. (2007) took laterally averaged data for 45° backwards ribs at a singular blowing ratio of M=0.5 and found lower effectiveness values when compared to a smooth wall case. A much larger range of blowing ratios was tested including $0.5 \leq M \leq 1.25$, and the same convergence trend was found for the laterally averaged effectiveness curves. The convergence point was at a blowing ratio of M=1.0, and at the high blowing ratio M=1.25 the backward ribs did moderately better than the forward ribs. Laterally averaged data curves taken for a smooth wall case at M=0.5 and 0.75 were positioned between the two rib cases. Examination of effectiveness plotted against z/d shows slight alterations in the jet profile compared to previous studies with smooth wall crossflow configurations. Contour plots in literature for perpendicular crossflow show jet maximum effectiveness values favor the upstream side of the hole and shift towards the centerline for increasing blowing ratio. Data taken from Agata et al. (2012) for the backward rib show a similar trend; however, the data for the forward rib suggests that the jet is approximately symmetrical about the centerline. A numerical study by Agata et al. (2013) was performed to provide some explanations for the experimental data collected by Sakai and Takahasi (2011) and Agata et al. (2012). It was concluded that rib orientation significantly affects the film cooling performance as a result of altered temperature and flow structures downstream of the cooling hole. As with many previous authors, this study traced the effects back to the hole inlet. A combination of the separation regions created by the ribs and the suction effects of the hole was found to significantly alter the in-hole streamlines. However, different rib orientations affect the interaction between the flow separation and hole suction effects, leading to differences in film cooling performance. The backwards rib configuration generates a strong spiral motion at the hole inlet which survives through the

hole exit.   When the fluid is injected into the mainstream, a skewed structure consisting of two separate bundles of fluid termed a "wall ward lump" and a "skewed vortical lump" is derived from the exit plane.   This structure was similarly observed by Sakai and Takahashi (2011) through non-dimensionalized temperature measurements of the jet taken in the *y/z* plane for increasing *x/d* locations downstream. The skewed vortical lump itself consists of a pair of vortices and moves farther away from the wall for increasing blowing ratio.   Its decreased contribution to effectiveness is counteracted by the jet wall ward lump which attaches to the wall and remains there for even high blowing ratios. The higher performance of the backward ribs at high blowing ratios is attributed to the wall ward lump's ability to remain close to the surface. Streamlines emanating from the jet exit plane illustrate the much calmer nature of the wall ward lump and depict the enduring corkscrew streamlines of the skewed vortical lump. Contrary to the backward ribs, the forward ribs generate a much simpler flow field more suggestive of a plenum or 0° crossflow configuration. A very small vortical motion is generated at the hole inlet which decays into a un-directional flow pattern aligned with the mainstream by the hole's exit. A much calmer and more coherent cluster of streamlines emanating from the exit results in the classical pair of counter-rotating vortices downstream.

Casting tolerances and film hole machining accuracies can lead to misplaced cooling holes. Inlets can be placed in close proximity of the ribs or even partially cut through a rib edge. It is therefore useful to understand the susceptibility of cooling performance to these realities. Kunze and Vogeler (2013) concluded that the effect on the external flow field as a consequence of rib placement is small. Although varying the rib positioning within the channel significantly affects the internal flow field, it has a very small effect on streamwise vorticity and the formation of jet wake zones. However, there were some minor changes in the overshoot region characterized by the jet core.

25

Normalized velocity profile measurements in the wall-normal direction taken at the centerline varied according to rib position. The case in which the holes were placed closest to the downstream rib had a more significant effect than when the holes were placed near the upstream rib. Of the set of three holes located farther downstream, the two most upstream issued noticeably higher normalized velocities in the jet core region. Rib positioning furthermore affected the coolant extraction of individual holes. It was noted that positioning a hole after a rib has more effect on coolant extraction and the surrounding flow field than prior to the rib. Despite this, the study asserted that the overall effects of rib positioning on downstream jet velocity profiles and the development of the counter-rotating vortex pair were small, mostly limited to the near hole region $x/d \leq 2$.

Understanding that inlet hole conditions have a significant impact on film cooling performance, a number of studies have created internal cooling designs with the expressed purpose of promoting beneficial coolant paths when entering the hole. Some studies have even gone as far as creating vortex generators to feed intentionally induced vortices into the hole (Papell (1984), Lerch et al. (2011)). A study by Wilfert and Wolff (1999) used a staggered 90° rib configuration for 0° crossflow on opposite walls to guide the coolant more axially into the hole in an attempt to accentuate the positive effects of parallel crossflow. It was concluded that the arrangement of ribs resulted in increased effectiveness when compared to a case without ribs. A vortex generator, smoothly redirecting coolant from the horizontal into the holes in an axial manner, was installed to intensify a particular set of in-hole counter-rotating vortices previously been shown by the authors to have a positive influence on the downstream mixing. The use of this vortex generator led to further gains in laterally averaged effectiveness when compared to

the ribbed channel cases, substantiating the exit flow distribution and vortices have a strong influence on the mixing behavior and subsequent film cooling effectiveness.

1.3 OBJECTIVES

The purpose of this study was to investigate the combined effects of various internal rib configurations and alternate directions of spanwise crossflow on the film cooling performance of compound cylindrical holes. There are relatively few studies available in literature which have measured film cooling effectiveness resulting from internal crossflow. Furthermore, there is no literature currently available that has measured film cooling effectiveness for cylindrical, compound angle holes fed by internal crossflow. The study presented in this thesis not only discusses the results of this arrangement but also compares its data to a standard plenum test and three different internal rib configurations. There is also limited data correlating the effects of internal ribs on external jet performance. Moreover, two of the rib configurations tested attempted to simulate and examine the effects of a possible real life circumstance by which a film cooling hole has intersected a rib, representing a configuration that has not yet been tested in literature.

Chapter Two

Experimental Facilities and Procedures

This chapter discusses the modification and validation of experimental facilities, calibrations of equipment, and the experimental testing procedures. Uncertainties for the experimental results are presented.

2.1 EXPERIMENTAL FACILITY

All tests included in this study were performed in a rectangular, closed loop wind tunnel. Previous flat plate film cooling testing in the wind tunnel had utilized a quiescent plenum to feed coolant through the film cooling holes. The test section of the tunnel and its piping system have been modified from its original design in order to accommodate an internal crossflow channel capable of alternating flow direction within the course of a test.

2.1.1 Primary Flow Loop: Mainstream Gas

The primary flow loop consisted of the closed loop wind tunnel which fed low-speed mainstream gas into the test section. The mainstream was driven by a variable speed 5 hp motorized axial fan. Its temperature was regulated by a fin and tube heat exchanger located downstream of the fan and upstream of the test section. Temperature controlled water was used as the secondary energy exchanging medium. Located in each of the four corners were turning vanes to reduce pressure losses. At the nozzle inlet leading into the test section were a series of screens and a precision honeycomb to condition the mainstream flow. A schematic of the wind tunnel facility is depicted in Figure 2.1. A smooth wall contraction and diffuser located on either side of the test section area accelerated and decelerated the mainstream flow, and a series of desiccant packs located downstream of the test section removed a significant amount of humidity

28

from the mainstream. As experimental film cooling temperatures are well below the freezing point of water, excess humidity can cause intermittent buildup of frost and ice in the near-hole region which can disturb the exiting coolant jet flow. A relative humidity indicator was installed in the tunnel to monitor its humidity condition, and the near-hole region was visually inspected throughout the course of a test to check that no frost buildup had occurred. Relative humidity levels of $\varphi \leq 0.6\%$ attained for every test ensured that no frost accumulation would occur for any of the blowing ratios tested.
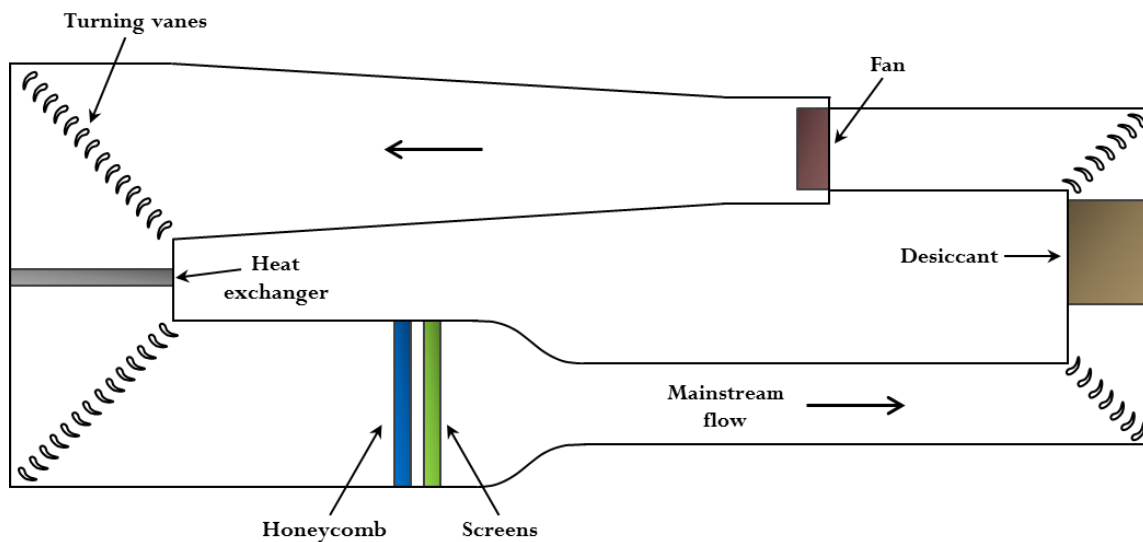
Figure 2.1: Primary flow loop.

2.1.2 Secondary Flow Loop: Coolant

In order to accommodate internal crossflow, the existing secondary flow loop purposed for solely the plenum condition was extensively modified. Pure nitrogen gas coolant, used to reduce the likelihood of frost or ice forming around the holes, was fed through an internal crossflow channel with a portion exhausting through film cooling holes. The remainder passed through the channel and exhausted into the primary flow loop. A number of different coolant exhaustion options were considered including a

recirculation loop to conserve coolant. Piping pressure loss, heat exchanger pressure loss, and heat transfer calculations were performed to evaluate its feasibility and select an appropriate recirculation blower. However the complexity of the recirculating loop, including the purchase of a specialized recirculation blower with blades made for cryogenic temperatures, did not justify the use of this system.
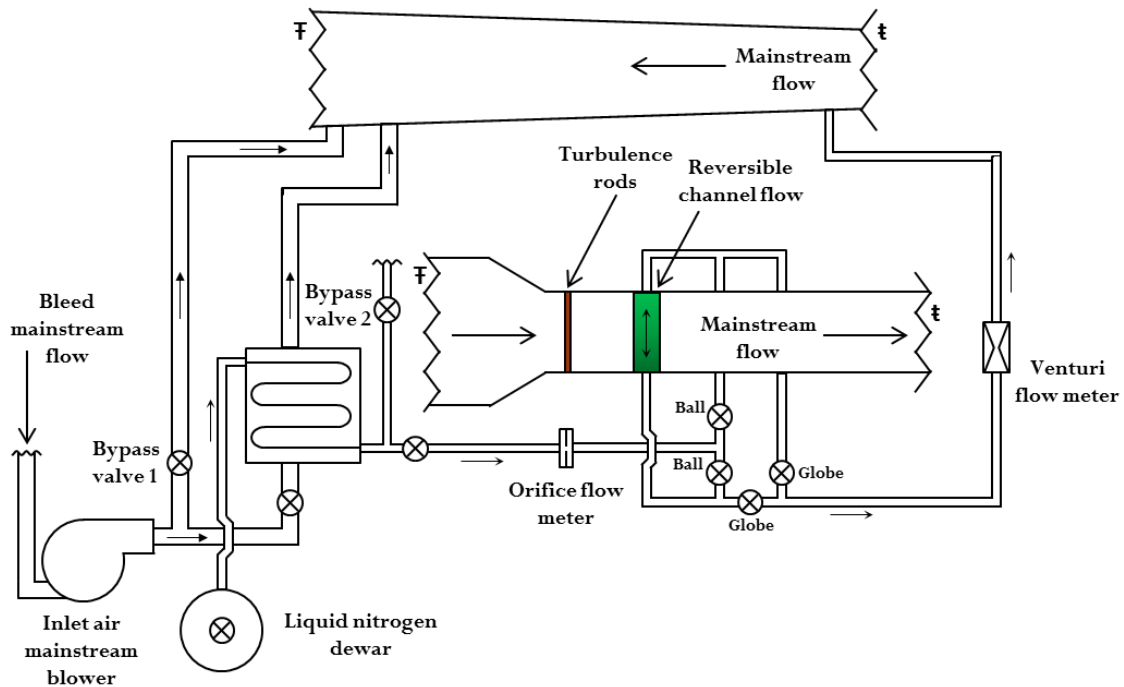
Figure 2.2: Experimental facility schematic, partial representation. Closed loop tunnel connections indicated by Ŧ and ŧ.

The coolant was supplied by a liquid nitrogen dewar at high pressure to overcome the considerable piping losses. Previous calculations confirmed that the dewar had the capacity to deliver coolant to the test section. As shown in Figure 2.2, a 7.5 hp constant speed blower extracted warm mainstream gas from the primary loop to heat and vaporize the liquid nitrogen in a heat exchanger. In order to heat the coolant to the necessary temperature, valves located before the heat exchanger could be adjusted to control the

amount of mainstream gas entering the heat exchanger and therefore the amount of energy transferred to the coolant. The coolant exited the heat exchanger and was transported to the test section by means of a piping system designed to allow channel flow direction to be alternated during the course of an experiment. A series of ball and globe valves were installed in the coolant piping to accomplish the reversal of crossflow direction. Schematics of the valve configurations for corresponding crossflow directions are shown in Figure 2.3. As the liquid nitrogen dewar was not designed for precisely managing coolant discharge, bypass valve 2 (seen in Figure 2.2) was used to more finely regulate a constant coolant mass flow through the channel inlet. The globe valve downstream of the channel exit (indicated in Figure 2.3 in yellow) created a controllable obstruction, thereby altering the pressure of the secondary piping system and allowing a greater or lesser amount of coolant to be forced through the film cooling holes in the test coupon (indicated in Figure 2.3 by the green, rectangular plate). Furthermore, a plenum test was required as part of the experiments. The plenum was to be installed directly underneath test section, and consequently the piping designed for crossflow would not be suitable. To ensure a versatile secondary piping system, union fittings (selected union fittings shown in Figures 2.3 and 2.4) were installed and allowed for sections of piping to be removed. Piping was specially made for the plenum condition and equipped with a female end union fitting, allowing it to be attached to the secondary piping system. A schematic of the plenum condition piping system is shown in Figure 2.4. It should be noted that secondary piping downstream of the orifice flow meter was designed to be removable in the event that subsequent piping renovations were necessary for the small wind tunnel. This was similarly accomplished through the use of union fittings and flanges.

31

(a) In-line crossflow

(b) Counter crossflow
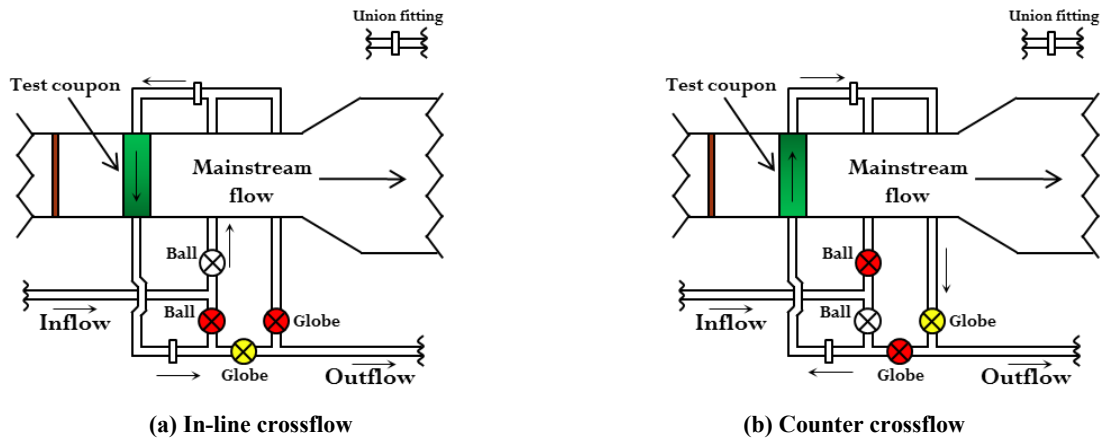
Figure 2.3: Detailed look at valve configurations for tested crossflow directions. Red valves indicate a fully closed position, white ball valves indicate a fully open position, and yellow globe valves indicate partially open valves used for exit mass flow regulation.
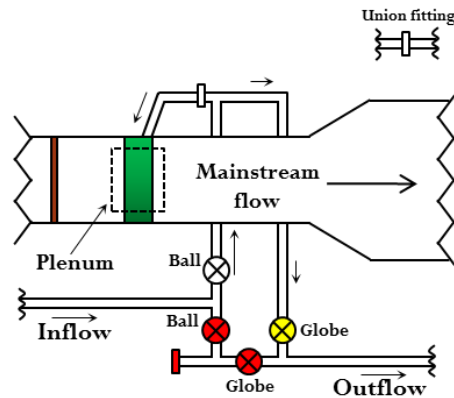
Figure 2.4: Detailed look at piping and valve configurations for plenum condition. Red valves indicate a fully closed position, a white ball valve indicates a fully open position, and a yellow globe valve indicates a partially open valve used for exit mass flow regulation. Coolant enters the plenum from directly underneath the test section by means of an auxilary piping segment connected to the union fitting.

2.1.3 Test Section and Validation of Boundary Conditions

The test section, shown in Figure 2.5, was comprised of the flat plate film cooling surface inside the wind tunnel and the crossflow channel attached directly below. The walls of the wind tunnel were made of Plexiglas so the operator could observe the film cooling area and make adjustments, if necessary, by means of various access ports during the test. The dimensions of the test section were 609 mm across in the spanwise z-direction and 138 mm high in the y-direction.

The test coupon containing the film cooling holes was used to take adiabatic effectiveness measurements and was therefore constructed from a low conductivity, rigid, closed cell polyurethane foam (k~0.048 W/m·K) from General Plastics. Cylindrical film cooling holes, each 5.0 mm in diameter, were machined into the coupon at a streamwise inclination angle of $\alpha=30°$ and a compound angle of $\beta=45°$. To match the client's specifications for realistic engine conditions, hole diameters of 5.0 mm were selected because film mass extraction per hole was desired to be nominally 5% at a blowing ratio $M=3.5$ and a density ratio $DR=\rho_c/\rho_\infty=1.5$. All test section dimensions were based off the cylindrical hole diameter $d = 5.0$ mm in order to appropriately scale the experiment to turbine conditions. Therefore, a row of eight holes, each spaced at a distance of $p/d=6.25$ ($p=31.25$ mm) apart, was machined to more accurately represent the film cooling interaction effects found on a turbine blade. In order to obtain the non-dimensional length $L/d=6$ ($L=30$ mm) for the cooling hole through the coupon, the imposed thickness of the test coupon was made to be $3d$ (15 mm). To ensure uniform surface emissivity, the coupon was painted black.
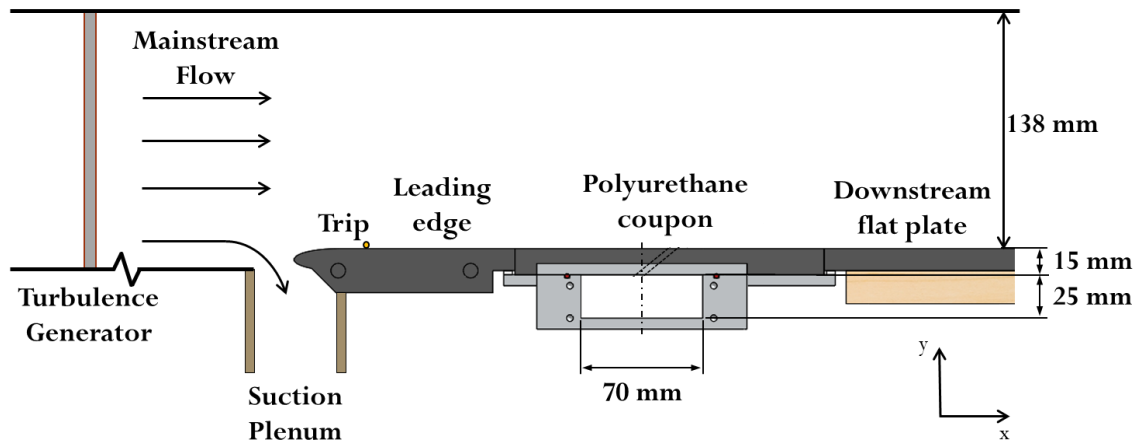
Figure 2.5: Test section schematic, x-y plane.

33

A 2:1 elliptical leading edge was mounted over a suction plenum upstream of the film cooling holes. The upstream boundary layer was removed and the formation of a new boundary layer was initiated on the stagnation point of the leading edge. The stagnation point had previously been verified by Boyd (2014) through the use of particle imagery velocimetry (PIV). Boundary layer conditions were specified to replicate conditions on a film cooled turbine airfoil with showerhead injection. A fully turbulent approach boundary layer was desired and successfully replicated by installing a 3.175 mm diameter cylindrical trip just downstream of the stagnation point of the leading edge, resulting in a thickness of δ/d=2.7, a displacement thickness of δ^*/d=0.36, a momentum thickness of θ/d=0.27, and a shape factor of H=1.33. A series of experiments was performed to obtain the final external boundary layer conditions, and a more detailed description can be found in Section 2.3.2.

Elevated levels of turbulence are commonly found in a first stage turbine blade and were prescribed by the client. Therefore, a passive turbulence generator was inserted just downstream of the tunnel wall contraction but upstream of the coolant holes by a distance of 383 mm. A turbulence level of Tu=5.0% was achieved experimentally by passing the mainstream through a row of 9.525 mm diameter vertical cylinders evenly spaced at 25.4 mm. The turbulence integral length scale was measured to be Λ_f=22 mm or 4.4 times the cooling hole diameter. All turbulence measurements were taken by laboratory member Josh Anderson.

The internal crossflow channel was oriented perpendicularly to the mainstream direction and installed flush with the underside of the test coupon. Considered in the channel's design was its durability to the extreme operating conditions, ease of assembly and installment, and fulfillment of internal flow conditions. The entire channel was constructed out of a few pieces of aluminum 6061-T6, a material commonly used in

cryogenic applications. The dominant part was essentially a large c-channel, and two grooves ran the entire length of the part to house nominal 3/32" silicone o-ring cord stock (see Appendix A.1). Silicone is resistant to cold temperatures, and the ability to retain more elasticity allows it to create a more effective seal at cryogenic temperatures. The grooves were dimensioned according to literature to allow for a face seal to be properly engaged. The remaining parts were bolted into the tapped holes located in the top face of the channel to seal it and complete the enclosure. The test coupon was bolted into the top but, due to its porosity, would not have been able to properly engage the o-ring cord stock and seal the channel. Therefore, rectangular slots were machined into the bottom face of the test coupon to snugly fit two 6.35 mm by 25.4 mm Mic 6 aluminum bars. Mic 6 aluminum is a cast plate used for applications where very small flatness and thickness tolerances are required. Due to the extended length of many parts and the relatively small tolerances required for effective sealing, stock aluminum was dismissed. These two rectangular pieces of aluminum were inserted into the slots flush with the coupon's bottom surface and glued with 3M Scotch Weld 2216, a highly capable epoxy resistant to extreme forces even at cryogenic conditions. A schematic of the test coupon construction in relation to the channel is shown in Figure 2.6. A hole was then essentially countersunk into the test coupon so that the bolt head made contact with the epoxied aluminum bars, and the test coupon was bolted into the channel. Two 6.35 mm thick Mic 6 plates on either side of the test coupon were similarly bolted into the channel to engage the o-ring cord stock. The two junctions formed by the three top plates were susceptible to leaks due to elevated channel pressures; therefore, silicone caulk was applied at the seams to completely seal the upper face of the channel before each test. A leak test was performed for every test as described in Section 2.3.1. The two seams created by the intersections of the leading edge, polyurethane coupon, and the downstream flat plate were susceptible to

air ingestion from the laboratory. This was prevented by installing underneath them two rectangular aluminum lips the length of the test coupon. The lips extended just beyond the seams where extremely pliable weather stripping was added to prevent outside gas ingestion through the seams and into the test section (see Figure 2.7). Live IR camera shots including the seams were inspected during each test for unexpected changes in temperature. Quantified temperatures across the seam were later analyzed and usually followed a consistent trend, and any small changes in effectiveness that did occur at the seam location did not affect the overall laterally averaged effectiveness trend. Each aluminum lip contained through holes and was bolted in simultaneously with the test coupon.
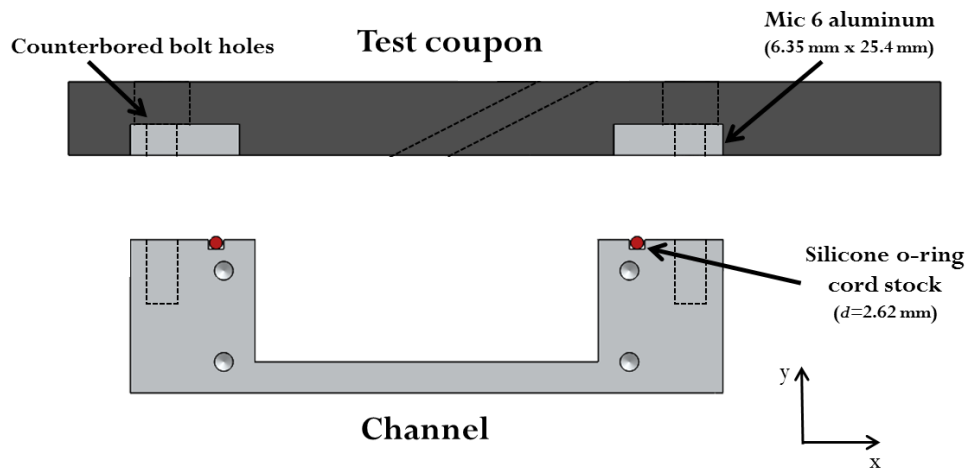
Figure 2.6: Schematic illustrating test coupon construction and channel. Test coupon was screwed into the channel to compress the silicone o-ring cord stock.
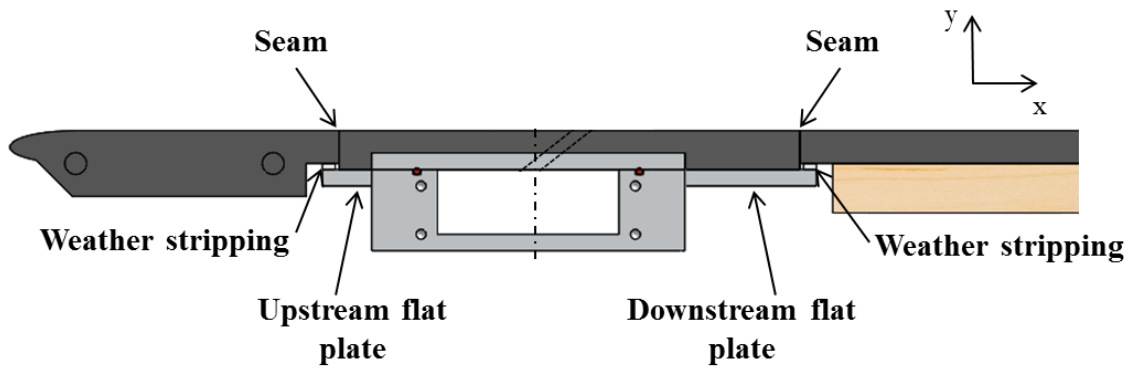
Figure 2.7: Test section design to avoid ambient air ingestion at seams.

The experiments called for a number of internal channel rib configurations, so it was decided that the most economical method was to produce rib plates which were designed to fit inside the channel and be interchangeable from test to test. The ribs needed to be flush with the underside of the test coupon in order to replicate ribs on a turbine blade serpentine wall, so a grooved pocket was machined at the top face of the channel in which the rib plates would rest (see Appendix A.2). The dimensions of the ribs were specified to be a square $1.25d$ (6.25 mm) and the spacing $2 \cdot p/d = 12.50$ (where p=62.50 mm was the spacing of the coolant holes), or two holes per rib pitch. Rib plates were precision water-jetted out of Mic 6 aluminum and lightly sanded until a snug fit inside the channel pocket was produced. Rib edges were lightly deburred to remove any unnecessary protrusions that would interact with the flow or inhibit flush contact with the test coupon. However, care was taken to ensure that the rib edges remained sharp. The ribs were angled to the internal crossflow at an angle of 45°, similar to the compound angled holes.
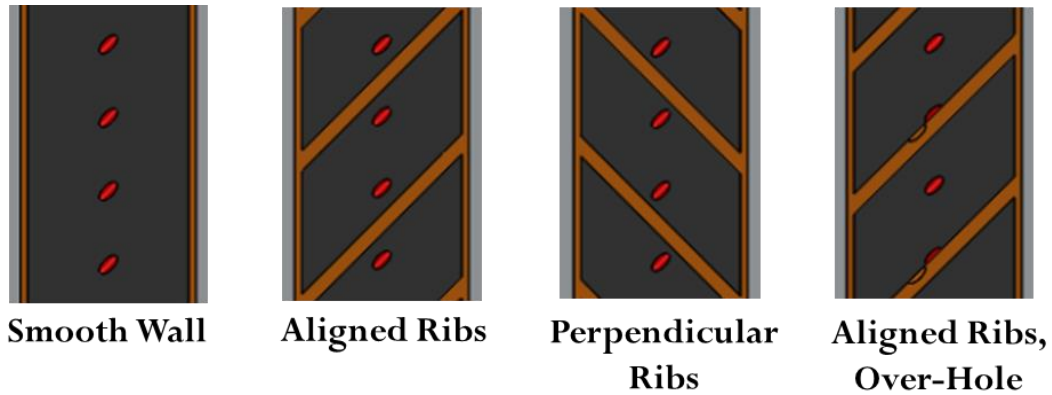
Figure 2.8: Channel rib configurations as seen from inside the channel.

Three different internal crossflow rib configurations, in addition to the smooth-wall baseline case, were produced and are displayed in Figure 2.8: ribs aligned to the hole direction, holes evenly spaced within the rib pitch; ribs perpendicular to hole direction, holes evenly spaced within the rib pitch; and ribs aligned to hole direction, ribs partially over the hole. The aligned and perpendicular rib configurations consisting of holes evenly spaced between the ribs could be accomplished with one rib plate. After disassembling the test coupon from the channel, the plate simply needed to be flipped over to complete the alternate rib configuration. The aligned, over-hole rib configuration was created to replicate the actual possibility of a film cooling hole intersecting a rib. Due to the blade casting tolerances combined with film cooling hole machining accuracies, holes can be shifted from their intended location and even result in hole-rib intersections.
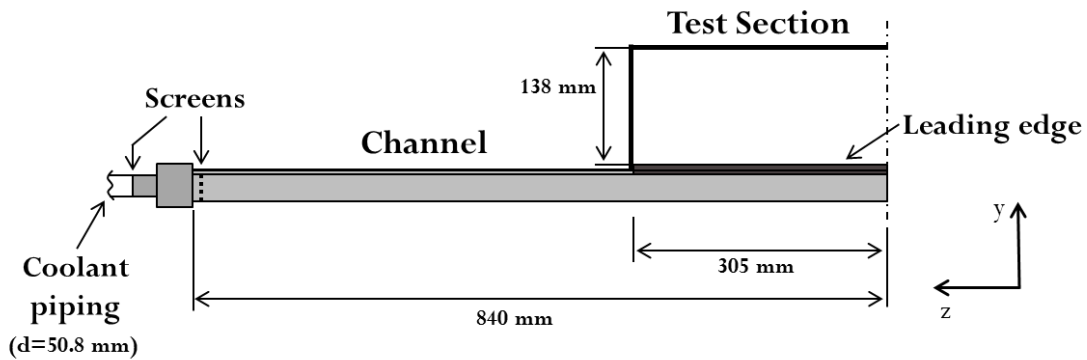
Figure 2.9: Partial schematic of one-half the test section, y-z plane. The screens are explained in detail in Section 2.3.3.

The cross-sectional area of the channel was specified to be $5d$ by $14d$ (25 mm by 70 mm). To help establish fully developed channel flow by the point at which coolant interacted with the ribs, a flow development length of 10.34 D_h (381 mm) was added to both sides. The rectangular channel was fed coolant by nominal 2" diameter (50.8 mm) cylindrical piping (seen in Figure 2.9), and consequently a contraction/diffuser part was specially machined to complete the transition between the dissimilar geometries (seen in Figure 2.10). The contraction/diffuser, termed pipe-to-channel transition piece, required coolant from the piping to expand in one direction and contract in the other in order to form to the cross-section of the channel. Literature was consulted to aid in the design of the piece, and as a result the expansion angles of the pipe-to-channel transition piece were minimized to avoid flow separation. This part was expertly machined by the department machine shop and reduced flow losses at the channel entrance. Both pipe-to-channel parts were bolted on each side normal to channel flow direction and silicone gaskets sealed the interfaces.

(a) Front view (piping side)   (b) Rear view (channel side)
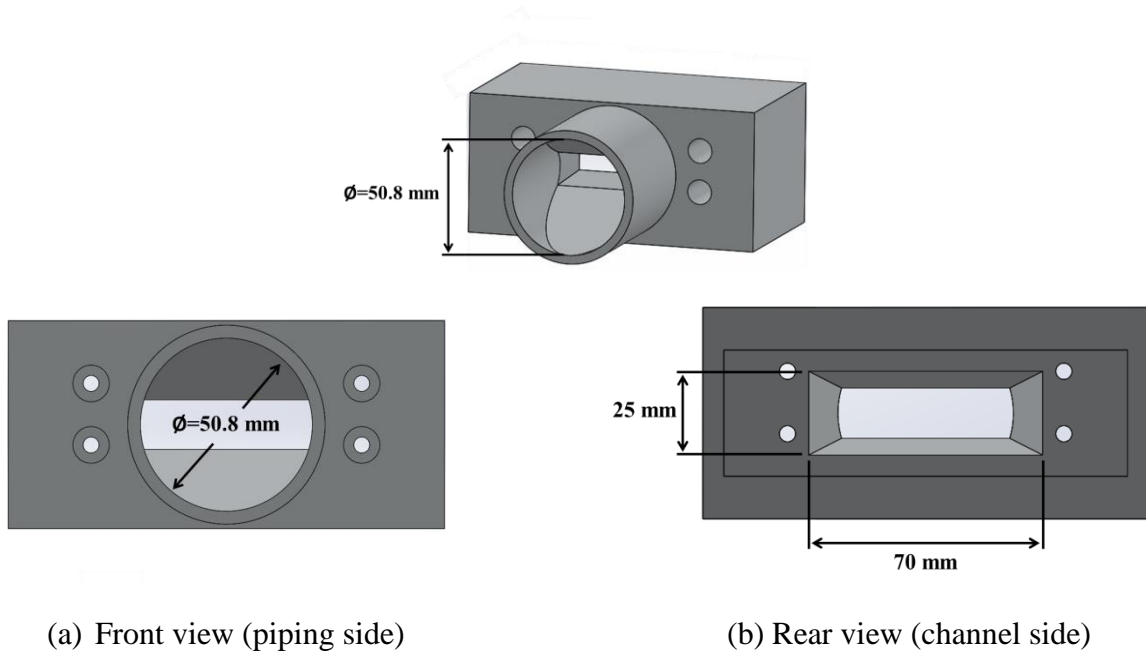
Figure 2.10: Pipe-to-channel transition piece.

The downstream flat plate, seen previously in Figure 2.5, was made to extend the spatial range required for the tests. Depending on the combination of infrared (IR) cameras and lenses used, the spatial range for tests was extended to about $48 \leq x/d \leq 60$. A polyurethane foam piece was fly-cut to ensure a high degree of flatness tolerance and adhered atop a piece of maple wood. Slotted holes were machined into L-brackets, and the brackets were bolted underneath the wood plate. Slotted holes were hand Dremeled into the acrylic tunnel walls into which screws were inserted and fastened to the L-brackets inside of the tunnel. Two screws on each side of the downstream flat plate near the corners allowed for an operator to efficiently level the plate inside the tunnel. Similarly, holes were slotted in the tunnel directly in line with the leading edge into which threaded holes were cut to accept screws. The implementation of slotted holes in the test section design, especially for pieces in which hand tools were used to remove material, allowed for a greater degree of error. Holes could have been drilled into the

acrylic side walls, and the leading edge and downstream flat plate could have been fastened into place. However, the necessary use of hand tools would have made it highly unlikely that each piece would have been level. Therefore, the slotted holes compensated for this by allowing the pieces to freely move independently of one another in the vertical direction until they were fastened in the proper location. Rubber gaskets were added at the interface of the screw head and acrylic wall to prevent the screws from slipping. A computer generated replication of parts of the test section without insulation can be found in Figure 2.11. Note that the washers and rubber gaskets at the interface of the socket head screws and acrylic wall are not shown.
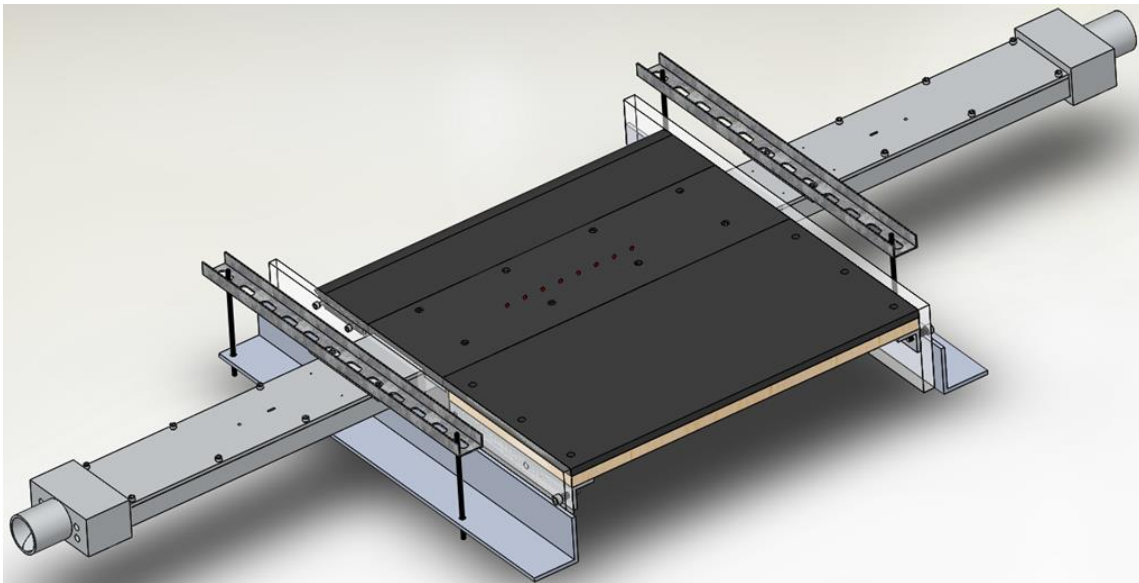
Figure 2.11: Test section area including installed channel. The acrylic side walls and the extended L-brackets are intrinsic to the wind tunnel and have been partially cut away to more easily view the test section.

The plenum condition required a new test coupon to be manufactured. Gas thermocouples were positioned so that coolant temperature was measured at the inlet of selected film cooling holes. The test coupon was adhered to a cut piece of acrylic using 3M Scotch Weld and bolted down to an already-made plenum, between which a 1/8"

silicone gasket ensured the seal. The interior of the plenum was approximately L=19",
W=6.25", and H=20". Insulation of ¾" thickness was adhered to all interior walls of the
plenum. Coolant was fed through the bottom of the plenum by a nominal 3" pipe. A
series of three mesh screens, each spaced 5" apart starting from the top of the plenum,
was installed to condition and create a more even coolant flow through the plenum.

2.2 CALIBRATION OF EQUIPMENT

The obtainment of accurate data required the calibration of a number of flow,
pressure, and temperature measurement devices. This section discusses the types of
equipment calibrated and the general conduct of the calibrations.

2.2.1 Pressure Transducers

A number of pressure transducers were bought and calibrated in order to
accurately measure the gas flows in the primary and secondary loops. Flow calculations
were initially performed so that the Omega Engineering pressure transducers bought were
capable of measuring the appropriate pressure ranges. Pressure transducers used in the
experiments can be found in Table 2.1. A setup was used to measure pressures
simultaneously applied to a manometer and each pressure transducer. A
micromanometer was used to very accurately measure pressure for pressure transducers
in the 0-10 in. range, while an upright manometer was used for the pressure transducers
capable of reading up to 25 in. H_2O. Pressure transducers were securely installed, wired,
and hooked up to a National Instruments data acquisition (DAQ) system. A Labview
program created by previous members of the lab was slightly altered and used to record
pressure transducer voltage outputs for the corresponding applied pressure. Pressure
readings were recorded for increasing and decreasing measurements to check for a
possibility of a hysteresis effect. Pressure transducers were periodically checked and

recalibrated to ensure the accuracy of successive tests but were found to have negligibly different calibration curves. A sample calibration curve is shown in Figure 2.12.

Table 2.1: Pressure transducers used in tests.

Placement	Type	Pressure Range (in. H_2O)
Orifice	Differential	10
Orifice	Static	25
Venturi	Differential	2
Venturi	Static	25
Mainstream	Differential	1
Channel in	Static	±25
Channel out	Static	10
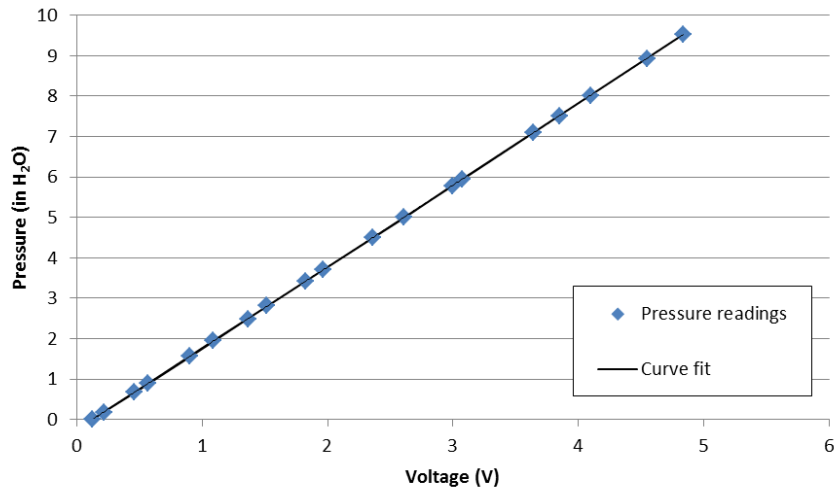
Figure 2.12: Sample pressure transducer calibration.

2.2.2 Orifice Flow Meter

An ORIPAC flow meter from Lambda Square was purchased to measure the mass flow rate of the nitrogen gas coolant entering the channel. Calculations were performed prior to the purchase to determine the appropriate vena contracta diameter based off coolant mass flow calculations. A Type E gas thermocouple was made and installed just upstream of the flow device, and the pressure ports of the ORIPAC were connected to pressure transducers measuring differential and static pressure. The secondary flow loop piping was designed to allow for the recommended upstream and downstream straight piping flow development lengths. The orifice meter was calibrated according to an empirical discharge coefficient correlation from J. Stoltz, shown in Equation 2.2.1, stated to be accurate to within 0.2% (Goldstein (1996)).

$$C_d = 0.5959 + 0.0312\beta^{2.1} - 0.184\beta^8 + 0.0029\beta^{2.5}\left(\frac{10^6}{Re_{D_h}}\right)^{0.75} \qquad (2.2.2.1)$$

$$+ 0.09\frac{L_1\beta^4}{1-\beta^4} - 0.0337L_2'\beta^3$$

The variable β is the dimensionless ratio of orifice hole diameter to pipe diameter, and L_1 and L_2' represent the distances of the centerlines of the pressure-tap holes from the upstream surface of the orifice plate, non-dimensionalized by the internal diameter of the upstream pipe.

2.2.3 Venturi Flow Meter

A Venturi flow meter was used to measure the mass flow rate exiting the channel. Similar to the orifice meter, a gas thermocouple was made and installed just upstream of the flow device, and the pressure ports of the Venturi were connected to pressure transducers measuring differential and static pressure. To ensure accuracy at low blowing ratios where the differences in coolant mass inflow and outflow are at a minimum, the Venturi meter was calibrated using the orifice flow meter as the standard.

44

The channel crossflow section was bypassed, and a direct route from the orifice plate to the Venturi meter was established. This method was used to eliminate any doubt of an inaccurate exit mass flow measurement due to the possibility of coolant leaking from the channel section.

Initially a second orifice meter was installed as the exit flow meter, but lower blowing ratios could not be attained because of combined effects of the low exit flow rates and the high pressure losses accrued in the exit piping. Therefore the exit pressure losses had to be minimized. This problem was confirmed by an experiment in which a makeshift blower was attached to the piping downstream of the exit orifice flow meter. The increased suction resulting from the blower counteracted the pressure losses inherent in the exit piping system and allowed the desired low blowing ratios to be reached. Purchasing a production blower to install permanently as part of the piping system would therefore eliminate the problem, but the resources spent in time and money would have been too costly. As a result, less complicated and more easily implementable methods to solve the problem were investigated. Sources of major and minor pressure losses were identified in the exit piping section and included pipe fittings, valves, pipe diameter, and the orifice. Pipe fittings had already been selected to reduce minor pressure losses. The globe valves had large minor pressure loss coefficients. However, globe valves are excellent at flow regulation, and the exit valves needed this characteristic to control the blowing ratio. Butterfly valves, also widely used for flow regulation, were considered in the initial design of the piping system but disregarded in deference to the proven success of globe valve flow regulation. Pressure losses can also be mitigated by using a larger piping diameter. This was considered a last resort, as much of the original piping system would have to be destroyed and new pipe fittings and valves would have to be installed.

45

Replacing the orifice flow meter was the easiest and most expedient way to reduce pressure losses. Orifice plates force fluid to suddenly contract and expand, resulting in significant pressure losses. Therefore, the exit orifice meter was replaced by a readily available Venturi meter, whose design and high discharge coefficient reduced pressure losses. However, this alteration by itself was not able to sufficiently reduce the pressure in the coolant channel at the film cooling hole location. As a result, the tunnel was modified to create a suction effect similar to the installation of the makeshift blower. This was accomplished by lowering the pressure in the downstream part of the primary loop wind tunnel where the coolant flow exhausted. The desiccant packs situated in wind tunnel were staggered to better obstruct the flow and created a larger pressure drop in the tunnel at the exit flow exhaust region. Measurements from pressure taps installed in the tunnel confirmed this result, and lower blowing ratios were therefore able to be attained.

2.2.4 Infrared Camera

IR cameras are more manageable and provide significantly better spatial surface temperature readings than thermocouple arrays; consequently, two FLIR IR cameras were used to measure test plate surface temperatures. Cameras faced both downstream and upstream in order to capture larger spatial temperature measurements. The cameras were positioned such that their viewing ranges overlapped. To calibrate the IR cameras, surface thermocouples were made and adhered to copper plates using epoxy. The plates were spray painted black to match the emissivity of the test coupon and were situated on the test coupon at different streamwise locations. The thermocouples were wired into the DAQ, and a Labview program was used to record their measurements. As was done for all IR experiments, the cameras were shrouded to prevent reflected infrared radiation into the lens. Two NaCl windows mounted into the test section ceiling provided optical

access for the underlying test surface thermography measurements. The tunnel was operated with a mainstream temperature of 304.5 K, and as the coolant flowed out the film cooling holes over the thermocouples, corresponding IR images were taken. Measurements were taken for the temperature range expected in forthcoming experiments for both decreasing and increasing temperatures to account for the possibility of a hysteresis effect.

To process the IR camera measured temperatures at the location of thermocouples located on the test plate, FLIR software ThermaCAM Researcher Pro 2.7 was used. Raw IR images were inputted into the program, and the positions of the thermocouples were marked. These images were converted into a MATLAB file extension for later use. A MATLAB program written by previous laboratory students read the locating points and produced the IR temperature measurements at those locations. Temperature measurements for each thermocouple location were compiled to generate a final calibration curve. Camera calibrations can be influenced by camera positioning, so any time the camera was moved a new calibration was taken to ensure its accuracy. Over the course of the experiments, three separate FLIR cameras (T620, P20, and A655 models) were calibrated. Changes in the camera position required new calibrations. A sample T620 calibration taken on 11/19/13 is shown in Figure 2.13 for the camera position used in the perpendicular, aligned over-holes, and plenum configurations. Two other calibrations for the same camera position are also shown to illustrate the precision of the calibrations and the sustained repeatability of the camera over time. The T620 camera was always used for the upstream temperature measurements including the near-hole area and therefore had to be calibrated over a much larger temperature range than either the P20 or A655 cameras.
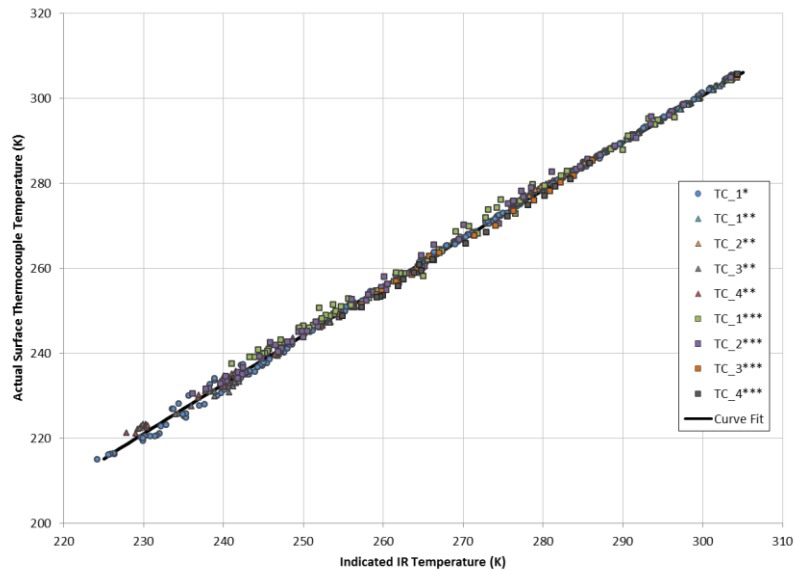
Figure 2.13: FLIR T620 IR calibration measurements for individual thermocouples over the course of 4 months. * Indicates calibration taken on 11/19/13 used for perpendicular, aligned over-holes, and plenum configurations. ** Indicates comparison calibration taken on10/23/13. * Indicates comparsion calibration taken on 02/24/14.**

2.3 VALIDATION OF BOUNDARY CONDITIONS

2.3.1 Leak Test

The exit Venturi flow meter had been calibrated to match the inlet orifice meter mass rate for a direct piping flow route between the two devices. To ensure a leak-proof channel and an accurate measurement of blowing ratio in forthcoming experiments, the channel was installed between the devices and its film cooling holes completely sealed off. Mass inflow and outflow measurements were taken, and the difference of 0.072 g/s resulted in a blowing ratio of M=0.030. These values were within uncertainty, as listed in Appendices D.1–D.4. A detailed description of uncertainty can be found in Section 2.5. A similar test was performed for every experiment to check for a nominally zero blowing ratio.

2.3.2 External Boundary Layer

Desired external boundary layer conditions and thickness were specified by the client. More specifically, a fully turbulent boundary layer was desired with a displacement thickness of δ^*/d=0.35 or an equivalent boundary layer thickness of δ/d=2.8. A Preston tube was mounted to a traverse just above the test ceiling wall and situated to make velocity measurements at the upstream edge of the film cooling holes for various locations normal to the test surface. Preston tube openings have a smaller height than standard pitot tubes, thus enabling measurements to be taken closer to the surface. In order to establish the Preston tube's origin at the surface, it was slowly traversed downward to the wall while looking at the surface through a small telescope. A flashlight illuminating the region of intersection from behind assisted in determining at which point the Preston tube touched the surface, as its shadow would slowly creep towards the tube until the two joined. At this juncture, velocity measurements would be recorded at a distance normal to the wall equal to half the height of the Preston tube. The Preston tube was connected to a differential pressure transducer, and velocity measurements were recorded using Labview. Measurements were recorded starting from the origin point at the test surface and traversing upwards. Once the measurements were clearly seen to be outside of the boundary layer and well into the mainstream, repeat data points were taken as the Preston tube was traversed back down to the wall. Mainstream velocity was set at the specified 13.8 m/s. In an attempt to match the specified approaching boundary layer condition, ten separate experiments were performed using several boundary layer trips with varying diameters at different upstream distances. Installing a 1/8" trip 38 mm downstream of the leading edge stagnation point resulted in a displacement thickness of δ^*/d=0.36 and δ/d=2.7, which were considered to be acceptable. Other external boundary layer parameters were previously listed in Section 2.1.3. Furthermore, the non-

49

dimensionalized velocity curve closely matched the 1/7 power law, indicating a fully turbulent approach boundary layer. Results of the test are displayed in Figure 2.14. Additional boundary layer measurements were performed at distances *x/d*=5 and 10 upstream of the holes to use as boundary conditions for a computational analysis. A graph comparing boundary layer results at different streamwise positions can be found in Appendix B.1.

External Boundary Layer at Film Cooling Holes
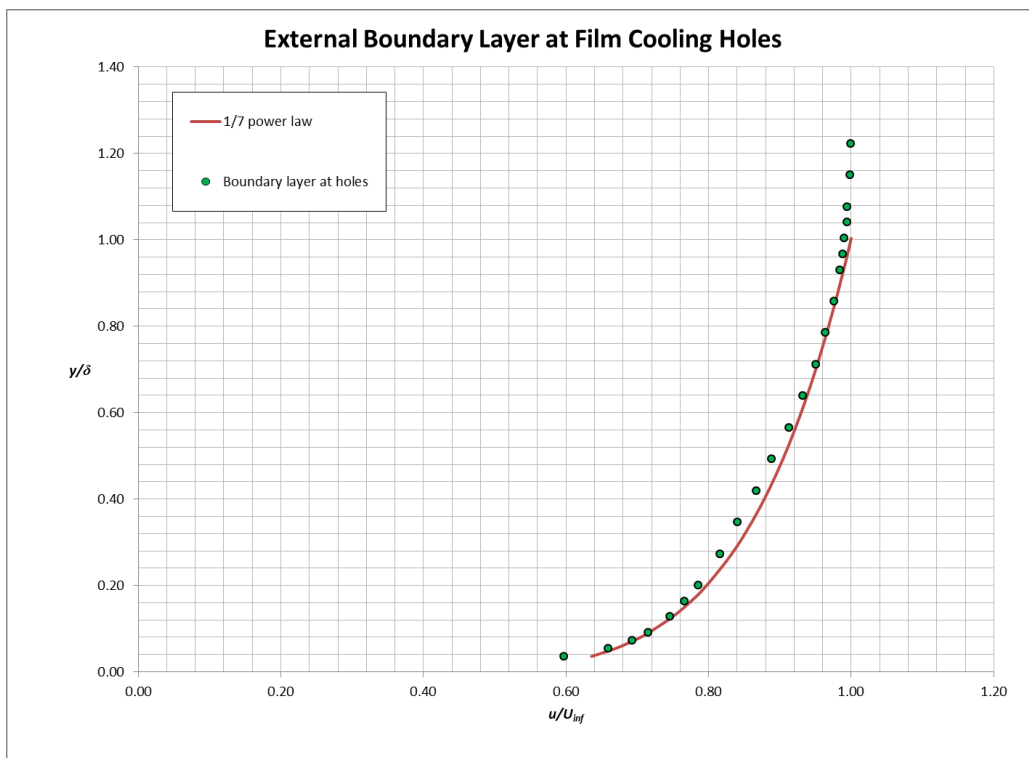
Figure 2.14: External boundary layer velocity profile taken at upstream edge of holes, *δ*=2.7*d.*

2.3.3 Internal Channel Velocity Profiles

A fully developed internal flow was desired to be established by the point at which the coolant first interacted with the rib plate. A series of experiments consisting of internal Preston tube velocity measurements were conducted to validate the fully developed flow condition. Holes had to be machined in the aluminum top plates

mounted to the channel on either side of the test coupon. Slotted through-holes were drilled to accept a Preston tube mounted to a vertical traverse, and counterbored holes were drilled as recommended by literature (Goldstein (1996)) for pressure taps. A schematic of the channel is presented in Figure 2.15. Prior to each test, the pipe-to-channel transition pieces were left aside, and a light was directed through the channel from the side opposite the location of the Preston tube. Similar to the procedure used in the external boundary layer tests, the bottom surface of the channel interior was located and the pipe-to-channel transition pieces were subsequently installed. The internal Reynolds number was matched to the specified internal crossflow condition of 35,000. Labview was used to record the static pressure tap and dynamic Preston tube measurements for each traversed location along the centerline of the channel. The Preston tube was traversed from the bottom of the channel upwards and then reversed back down to the wall to record repeat points.
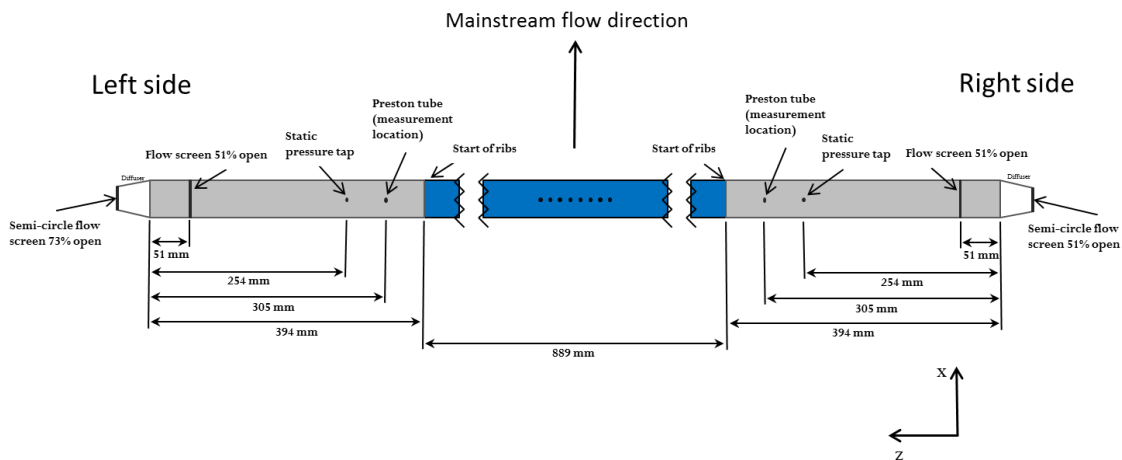
Figure 2.15: Channel schematic for internal velocity profile measurements including locations of permanent screens, x/z plane.

Due to the curvature of the piping immediately before the channel inlets, the measured internal velocity profiles were skewed towards the top of the channel. Limited

laboratory space necessitated either a curved 90° or 180° turn of the fluid before entering the channel and forced lasting skewed velocity profiles detrimental to a fully developed channel flow condition. A great many different internal devices were installed or implemented in an attempt to create a symmetric velocity profile. Screens were installed at various locations in the channel with various porosities to create pressure drops to even out the flow. Trips were placed either on the floor or ceiling or both. Combinations of screen installments and trip installments were used as well as using multiple screens within the channel. Each profile was compared against a fully developed channel velocity profile measured at a location 1.37 m from the inlet on the opposite side of the test section. Despite all of methods employed to even out the flow, none were able to completely produce a symmetric profile and many had little to no effect whatsoever. Ultimately, after 33 experiments, a solution was devised to force the fluid back down towards the floor of the channel by installing screens covering the upper half of the inlet piping in combination with the already installed screens within the channel. This successfully created acceptable internal channel velocity profiles, but due to the differing piping inlet conditions on each side different porosity half-screens were used at either end of the channel. Velocity profiles for the right side of the channel are presented in Figure 2.16, and the left side velocity profiles can be found in Appendix B.2. The x-axis is non-dimensionalized with respect to the middle of the channel, while the y-axis is non-dimensionalized with respect to the maximum velocity located at the middle of the channel y/h=1.00. Curves depicting the 1/7 power law and the velocity profile for the full development length of 1.37 m are presented as references. Note that velocity measurements were not taken beyond $y/h \geq 1.93$. The Preston tube had a hook-like bend near the tube opening that would interact with the channel top before the tube opening

could travel the full channel height. Pictures of the internal channel screens can be seen in Appendices A.1 and A.3.
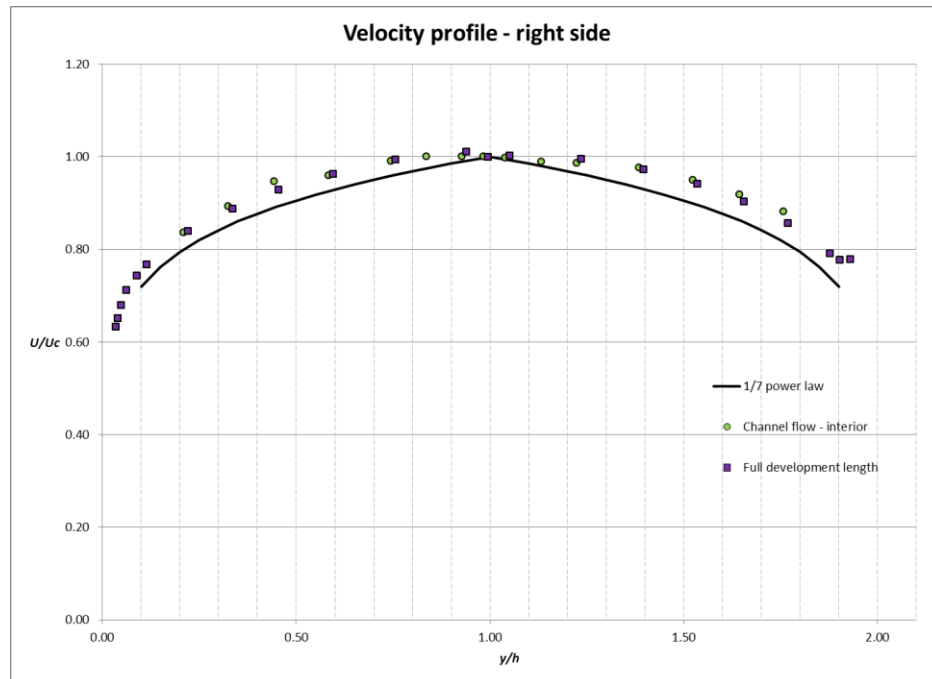
Figure 2.16: Internal channel velocity profiles compared against baseline curves.

2.4 FLAT PLATE EXPERIMENTS

This section will discuss experiment preparation, operations, and the subsequent processing of data.

2.4.1 Test Preparation

The channel was assembled outside of the tunnel according to the rib configuration to be tested. Rib plates were placed in the channel pocket, and the top faces were applied lightly with vacuum grease to ensure that no coolant leaked between the rib and test coupon interface. The smooth wall configuration required two thin water jetted aluminum strips be placed in the pocket grooves. They were held in place by

inserted 1/16" pins which ran through the aluminum top plates on either side of the channel. The test coupon, aluminum lip plates, and aluminum top plates were bolted into place, and silicone caulk was applied at the appropriate interfaces. The counterbored holes in the test coupon were filled with spackle and lightly sanded until flush with the surface. A prepared and assembled channel is shown in Figure 2.17.

Figure 2.17: Assembled channel and test coupon. A layer of black insulation was adhered to the aluminum to constitute a first layer of insulation.

Before installing the channel in the wind tunnel facility, the leading edge and downstream flat plate were leveled using spirit levels and secured into place. The channel was then installed into the tunnel, raised, and leveled on an outrigger system consisting of struts, threaded rods, and nuts (see Figure 2.18). The test section was designed so that the weather stripping (see Figure 2.7) would engage the leading edge

and downstream flat plate pieces as the channel was raised into position, thus preventing ambient air ingestion into the test section. The channel was adjusted until the two seams on either side felt flush to the touch, and a spirit level was used to verify the channel's levelness in both the spanwise and streamwise directions. If necessary, spackling was applied to the seams to ensure uniform smoothness throughout the test section. Piping was connected at the union joints and mated with the pipe-to-channel pieces with rubber couplings to complete the circuit. Extensive insulation around the channel was applied to reduce the rise in the temperature through the channel Tests were performed at the specified density ratio using the same insulation set up and temperature comparisons were made among the film cooling holes. The temperature rise across the holes, nominally less than 1.3 K, was found to be small enough as to not affect the results of the study.

Figure 2.18: Channel leveling system.

2.4.2 Test Operations

Commencement of a test began with inserting heated desiccant packs into the tunnel, ensuring that the interior relative humidity was kept below 5% throughout the test. Nitrogen was allowed to flow through the secondary piping, and following channel cool down completion the drastic changes in temperature experienced by the channel many times required a re-leveling of the test plate coupon. The completion of channel cool down required that both sides of the channel held a steady temperature at approximately 10 to 12 Kelvin apart. Due to the warming of coolant over the length of the channel, the channel inlet would arrive at its desired temperature about 15 minutes before the channel outlet. The specified test conditions and parameters were met and held in a steady state for 5-10 minutes before making surface temperature measurements. This required continual maintenance and adjustments of valves, the manner of which is described in Section 2.1.2. An extensive Labview program written by a previous laboratory member was slightly altered to record pressure and temperature data for each blowing ratio tested. A singular data point recorded by Labview consisted of averaging 1000 data samples over a time period of 2 seconds, and a corresponding IR image was captured during that time period. This was repeated a minimum of 3 times over a minimum 5 minute period for each blowing ratio. Measurements from the first blowing ratio visited were repeated after data from all other blowing ratios had been recorded. Crossflow directions were switched mid test, and the same measurements were repeated. The test plate was continually inspected for uneven conditions and frost. None of the experiments required re-leveling the test plate after the initial re-leveling performed following channel cool down. Frost similarly was never a problem; nevertheless, due to prior user knowledge and experience with frost effects before the tunnel was properly sealed and the desiccant packs functional, operators of the wind tunnel checked the test

section in the event that frost appeared. After completion of the experiment, locating marks of known distances were drawn on the test surface in the x/d direction and captured in the IR cameras.

2.4.3 Data Processing

Processing files were created which used in the Labview output data and calculated the testing conditions. The spatial locations of temperature recorded by the IR images were quantified using the relative positioning of the locating marks previously captured. Positioning data was inputted into a Matlab program created by previous laboratory members but changed by McClintic (2012) to be significantly more powerful, flexible, and user-friendly. The program corrected for a number of camera issues, including converging lines due to the camera's perspective view and camera rotation, and outputted effectiveness values for user inputted spanwise and streamwise locations on the test surface. The data was then paired with the corresponding testing conditions.

All adiabatic measurements were taken with the polyurethane foam coupon, but despite the foam's low conductivity, the measurements needed to be corrected for conduction effects that distorted the temperature readings on the surface. Therefore, two of the film cooling holes were blocked at the end of every experiment and the region imaged in the IR cameras to measure the "effectiveness" without film cooling, η_0, which is defined as

$$\eta_0 = \frac{T_\infty - T_0}{T_\infty - T_c} \qquad (2.4.1.1)$$

where T_0 is the surface temperature without film cooling and T_c is the coolant temperature at the inlet of the hole. One-dimensional heat transfer relations for heat flux into the surface for the cases of a surface with and without film cooling are noted in Equations 2.4.1.2 and 2.4.1.3, respectively.

$$q''_f = h_f(T_{aw} - T_{w,f}) = \frac{k}{L}(T_f - T_{b,f}) \qquad (2.4.1.2)$$

$$q''_0 = h_0(T_\infty - T_{w,0}) = \frac{k}{L}(T_0 - T_{b,0}) \qquad (2.4.1.3)$$

The subscript f signifies the film cooling case, 0 signifies the case without film cooling, w signifies the wall temperature, b signifies the temperature at the base of the plate, L signifies the thickness of the plate, and k signifies the thermal conductivity of the plate (Figure 2.19).
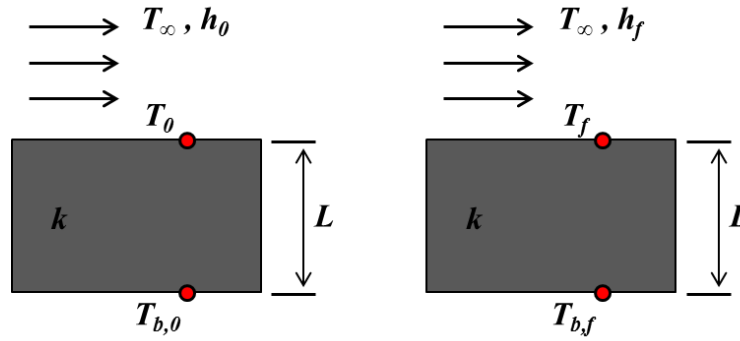
Figure 2.19: Partial representation for a one-dimensional conduction correction

Rearrangement of the previous equations resulted in non-dimensionalized Equations 2.4.1.4 and 2.4.1.5.

$$\frac{h_f L}{k} = \frac{T_f - T_{b,f}}{T_{aw} - T_f} \qquad (2.4.1.4)$$

$$\frac{h_0 L}{k} = \frac{T_0 - T_{b,0}}{T_\infty - T_0} \qquad (2.4.1.5)$$

Normalized adiabatic effectiveness and temperatures without and with film cooling are defined in Equations 2.4.1.1, 2.4.1.6, and 2.4.1.7.

$$\eta_f = \frac{T_\infty - T_{b,f}}{T_\infty - T_c} \qquad (2.4.1.6)$$

$$\theta_0 = \frac{T_\infty - T_{b,0}}{T_\infty - T_c}, \quad \theta_f = \frac{T_\infty - T_{b,f}}{T_\infty - T_c} \qquad (2.4.1.7)$$

58

Combining equations 1.1.2, 2.4.1.1, and 2.4.1.4-2.4.1.7 resulted in equations 2.4.1.8 and 2.1.4.9.

$$\frac{h_f L}{k} = \frac{\theta_f - \eta_m}{\eta_m - \eta} \qquad (2.4.1.8)$$

$$\frac{h_0 L}{k} = \frac{\theta_0 - \eta_0}{\eta_0} \qquad (2.4.1.9)$$

Combining and rearranging equations 2.4.1.8 and 2.1.4.9 resulted in the conduction correction Equation 2.4.1.10.

$$\eta = \eta_f - \frac{\eta_0(\theta_f - \eta_f)}{h_f/h_0\,(\theta_0 - \eta_0)} \qquad (2.4.1.10)$$
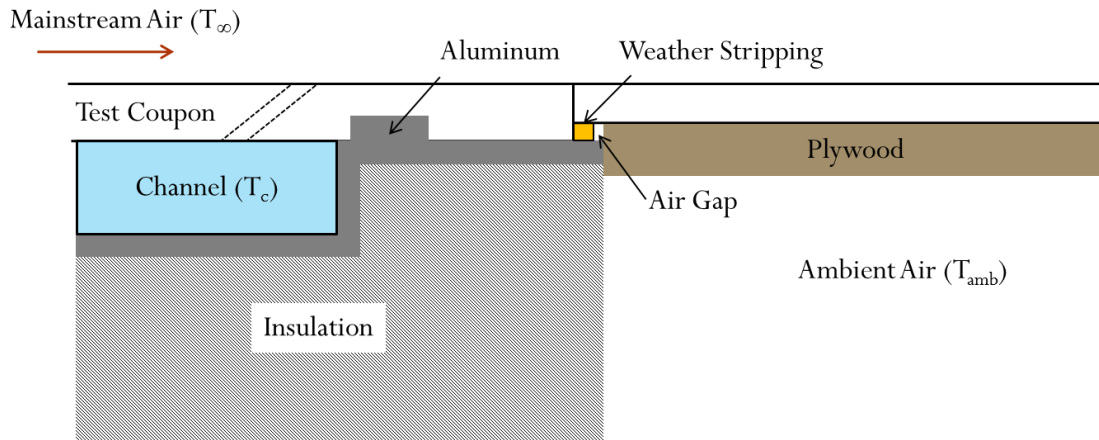
Figure 2.20: Partial representation of conduction correction region

However, a simplified one- or two-dimensional conduction correction could not be applied to the test coupon due to two rectangular aluminum bars slotted in the test coupon as well as the aluminum lip plates underneath (see Figure 2.20). The driving temperature could not be assumed to be the internal coolant temperature, and lateral conduction effects were considered significant. Thus, a three-dimensional conduction correction was applied to the coupon to project the driving temperature using the software Comsol Multiphysics. Heat transfer coefficients were provided by Emily Boyd by means of previously conducted experiments. Simulations were run by John McClintic and resulted

in the determination of the adiabatic wall temperature. The three-dimensional simulations more accurately assessed the conduction correction, especially for $4 \leq x/d \leq 16$ where the one-dimensional conduction correction failed to account for lateral conduction. However, comparisons of the three-dimensional conduction corrections in Comsol and the one-dimensional conduction correction Equation 2.4.1.10 yielded no differences in laterally averaged effectiveness, meaning there were negligible conduction errors in the streamwise direction.

Due to large three-dimensional conduction effects emanating from coolant convection within the holes, the immediate near-hole region was subjected to large errors. Effectiveness values were examined originating from the hole and extending outward on a line normal to the hole. In the most extreme cases, the corrected effectiveness declined to $\eta < 0.021$ ($\delta\eta = \pm 0.021$) at the downstream value of $x/d = 2.4$. A conservative estimate of $x/d = 4$ was then appropriated as the point at which effectiveness data was unaffected by near-hole conduction. Data upstream of that point should only be considered qualitatively. A more detailed explanation of the conduction correction applied to the data can be found in McClintic et al. (2014).

A review of the compound angle hole study from Sen et al. (1996) was used as a reference for heat augmentation values. However, differences in the current experimental setup and conditions required lower heat augmentation values than those measured in Sen et al. (1996). A heat augmentation value for the current study of $h_f/h_0 \approx 1.2$ was estimated at the highest blowing ratio $M = 2.0$, and the lowest blowing ratio $M = 0.50$ was expected to have a value $h_f/h_0 \approx 1.0$. Calculations showed that the largest error resulting from using a value of $h_f/h_0 = 1.0$ for the conduction correction was $\delta\eta = 0.0074$, a relatively small value that only applied to certain local effectiveness values at higher blowing ratios. As a result a heat augmentation value of $h_f/h_0 \approx 1.0$ was assumed, and the errors were accounted for in

the bias uncertainty analysis. Higher values of heat transfer augmentation uncertainty were assigned to higher blowing ratios due to increased jet interaction with the mainstream, and the numerical values were estimated using Sen et al. (1996) as a reference. A more detailed explanation of heat augmentation assumptions can be found in McClintic et al. (2014).

2.5 UNCERTAINTY ANALYSIS

To perform an uncertainty analysis on adiabatic effectiveness, Equation 2.4.1.5 was expanded and is defined in Equation 2.5.1.

$$\eta = \frac{h_f/h_0 (T_0 - T_{Al})(T_\infty - T_f) - (T_\infty - T_0)(T_f - T_{Al})}{h_f/h_0 (T_0 - T_{Al})(T_{\infty,f} - T_{c,f})} \qquad (2.5.1)$$

The temperature of the aluminum T_{Al} was assumed to be approximately equal to the temperature of the coolant inside the channel. The bias uncertainties inherent in the measurement of T_∞ are the same for $T_{\infty,0}$ and $T_{\infty,f}$ and consequently cancelled out. Therefore, only precision uncertainties were considered for T_∞.

It was necessary to quantify the comparability of adiabatic effectiveness measurements among the conducted experiments. A compilation of in-test and test-to-test effectiveness repeatability measurements were taken at M=1.0, and the plenum test-to-test repeatability (Figure 2.21) can be viewed as representative of the 95% uncertainty confidence level. Two streamwise positions, x/d=5 and x/d=25, were chosen to examine the uncertainty in effectiveness, and test-to-test differences in effectiveness measurements at those locations were $\delta\eta$=0.011 and $\delta\eta$=0.005, respectively. These

values can be viewed as the effectiveness uncertainty when comparing any two sets of measurements.
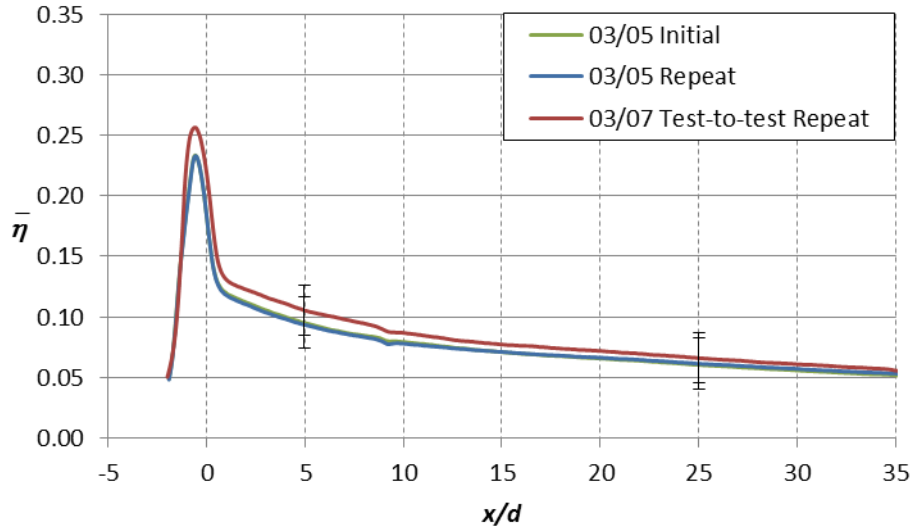
Figure 2.21: Plenum repeatability at *M*=1.0. Initial in-test repeatability was performed on 03/05, and measurements taken for test-to-test repeatability took place on 03/07. Test-to-test repeatability is representative of uncertainty in adiabatic effectiveness. Error bars are based on uncertainty calculations.

There were also some in-test repeatability measurements taken from separate experiments that have similar effectiveness disparities to the plenum test-to-test repeatability. The aligned, over-hole in-test effectiveness repeatability (Figure 2.22) had differences in effectiveness of $\delta\eta$=0.009 and $\delta\eta$=0.004 at x/d=5 and x/d=25, respectively. However, the majority of the other experiments had more repeatable effectiveness measurements for both test-to-test and in-test repeatability. The smooth wall in-test repeatability had differences in effectiveness of $\delta\eta$=0.007 and $\delta\eta$=0.005 at x/d=5 and x/d=25, respectively (Figure 2.23). The plenum experiment (Figure 2.21) had great in-test repeatability, and the perpendicular ribs test-to-test repeatability (Figure 2.24) was also excellent. Both experiments had effectiveness disparities of less than $\delta\eta$=0.002.

The presentation of these repeatability plots justifies using the plenum test-to-test effectiveness repeatability as representative of both test-to-test and in-test repeatability.
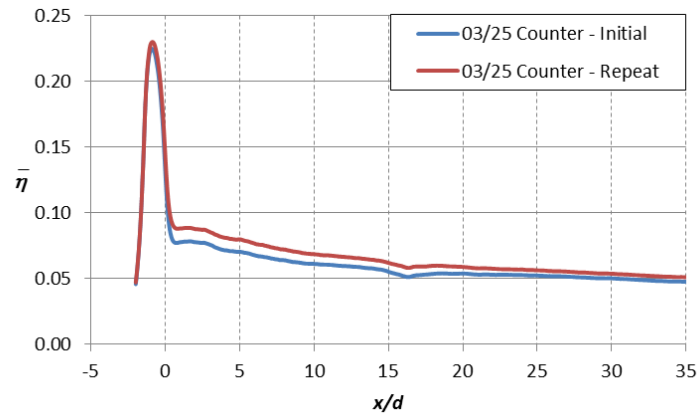
Figure 2.22: Aligned over-hole in-test repeatability.
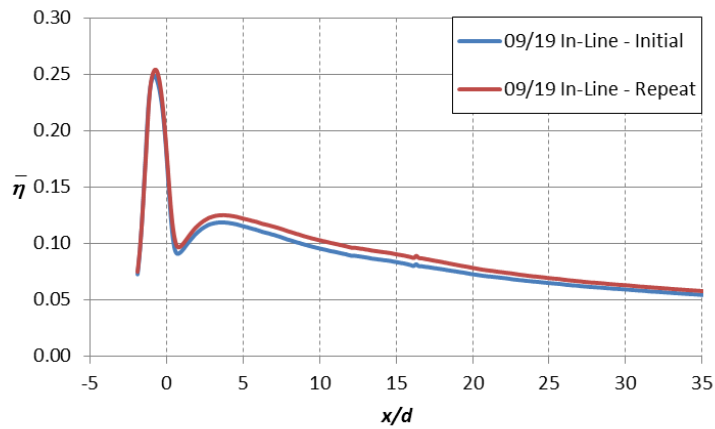
Figure 2.23: Smooth wall in-test repeatability.
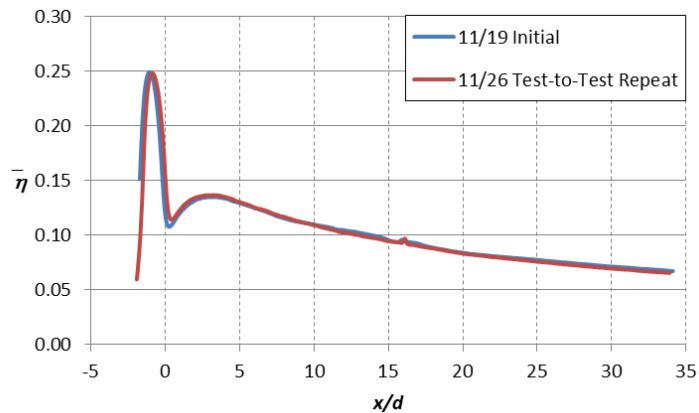
Figure 2.24: Perpendicular ribs test-to-test repeatability.

Calculations were performed to verify the experimental uncertainty evidenced by the plenum test-to-test repeatability. Comparing effectiveness measurement sets to one another necessitated considering only precision uncertainties. As a result, consistent bias uncertainties were disregarded in the uncertainty analysis. The vast majority of contributing precision uncertainties was comprised of temperature and pressure measurements, both of which have very small precision uncertainties. The precision uncertainties were estimated by examining the fluctuations and drift tendencies for both thermocouples and pressure transducers. At certain intervals during every test, a series of points were taken in quick succession at steady operating conditions to ascertain the fluctuations of the measuring devices. The fluctuations of the thermocouples were extremely small, resulting in a measurement precision uncertainty of 0.013 Kelvins. Fluctuations in the outputs of the pressure transducers were similarly small; however, the drift over the course of the test was larger and was therefore used in the uncertainty calculations for the blowing ratio. The precision uncertainty for the blowing ratio was included in the uncertainty estimate by using the method proposed by Kline and McClintock, and the slope $d\eta/dM$ was found by a linear estimation around the laterally effectiveness value at $M=1.0$ (Figure 2.25). Calculations (Tables 2.2 and 2.3) produced

uncertainty estimates of $\delta\eta$=0.021, significantly larger than what the experimental repeatability values would indicate as the actual uncertainty. The extent of the overlapping error bars in Figure 2.21 illustrates this disparity, and as a result the calculated uncertainty value can be considered conservative. The dominating factor in the precision uncertainty calculations was the surface temperature measurement of the IR camera. The measurement uncertainty, 1.5 Kelvins, assigned to the surface temperature was based on the scatter of IR calibrations. However, there are indications that the surface temperature measurements taken within a test have a smaller precision uncertainty. Pairs consisting of almost identical laterally averaged effectiveness measurements were compared. Within each pair, each effectiveness measurement was taken at similar operating conditions spaced a minimum of one minute apart. The differences in the surface temperatures were calculated over the range 4≤x/d≤30 and averaged. The results showed that the average difference in temperature was less than 0.060 Kelvins, indicating minimal fluctuations in the camera reading of surface temperature for nominally the same operating conditions.

As expected, the bias uncertainties for both x/d locations (shown in Tables 2.3 and 2.5) were nominally the same and were estimated to be $\delta\eta$=0.020, or a total uncertainty in a measurement for M=1.0 of $\delta\eta$=0.028. This number is heavily dominated by the large precision and bias errors in the surface temperature measurement.

Table 2.2: Adiabatic effectiveness precision uncertainty calculations at *M*=1.0 and *x/d*=5 for the plenum case.

Measured Parameter	Nominal Value	Measurement Uncertainty	Elemental Uncertainty
Surface Temperature with Film, T_f (K)	289.0	1.500	0.0157
Surface Temperature No Film, T_0 (K)	299.0	1.500	0.0138
Blowing Ratio, M	1.00	0.021	0.0019
Mainstream Temperature with Film, $T_{\infty,f}$ (K)	305.0	0.013	0.0001
Mainstream Temperature No Film, $T_{\infty,0}$ (K)	305.0	0.013	0.0001
Coolant Temperature with Film, $T_{c,f}$ (K)	203.3	0.013	0.0000
Calculated η	**0.105**		
Precision uncertainty, $\delta\eta$	**0.021**		

Table 2.3: Adiabatic effectiveness bias uncertainty calculations at *M*=1.0 and *x/d*=5 for the plenum case.

Measured Parameter	Nominal Value	Measurement Uncertainty	Elemental Uncertainty
Surface Temperature with Film, T_f (K)	289.0	1.20	0.0125
Surface Temperature No Film, T_0 (K)	299.0	1.20	0.0111
Blowing Ratio, M	2.00	0.07	0.0062
Heat Transfer Augmentation, h_f/h_0	1.00	0.20	0.0088
Coolant Temperature with Film, $T_{c,f}$ (K)	203.3	1.00	0.0007
Aluminum Temperature, T_{Al} (K)	203.3	3.00	0.0002
Calculated η	**0.105**		
Bias uncertainty, $\delta\eta$	**0.020**		

Table 2.4: Adiabatic effectiveness precision uncertainty calculations at *M*=1.0 and *x/d*=25 for the plenum case.

Measured Parameter	Nominal Value	Measurement Uncertainty	Elemental Uncertainty
Surface Temperature with Film, T_f (K)	293.0	1.500	0.0157
Surface Temperature No Film, T_0 (K)	299.0	1.500	0.0145
Blowing Ratio, M	1.00	0.021	0.0008
Mainstream Temperature with Film, $T_{\infty,f}$ (K)	305.0	0.013	0.0001
Mainstream Temperature No Film, $T_{\infty,0}$ (K)	305.0	0.013	0.0001
Coolant Temperature with Film, $T_{c,f}$ (K)	203.3	0.013	0.0000
Calculated η	**0.063**		
Precision uncertainty, $\delta\eta$	**0.021**		

Table 2.5: Adiabatic effectiveness bias uncertainty calculations at M=1.0 and x/d=25 for the plenum case.

Measured Parameter	Nominal Value	Measurement Uncertainty	Elemental Uncertainty
Surface Temperature with Film, T_f (K)	293.0	1.20	0.0125
Surface Temperature No Film, T_0 (K)	299.0	1.20	0.0116
Blowing Ratio, M	2.00	0.07	0.0026
Heat Transfer Augmentation, h_f/h_0	1.00	0.20	0.0092
Coolant Temperature with Film, $T_{c,f}$ (K)	203.3	1.00	0.0006
Aluminum Temperature, T_{Al} (K)	203.3	3.00	0.0001
Calculated η	**0.063**		
Bias uncertainty, $\delta\eta$	**0.020**		
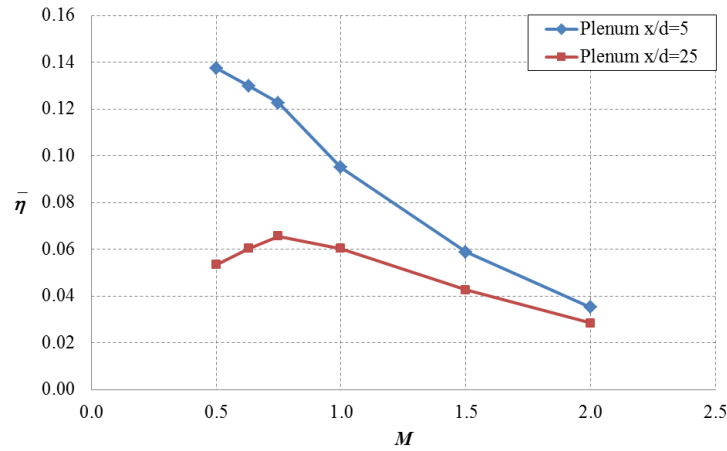
Figure 2.25: Plenum laterally averaged effectiveness for various blowing ratios

The difference in spatially averaged effectiveness for the plenum test-to-test repeatability at a blowing ratio of M=1.0 was calculated from experimental measurements. Effectiveness measurements were averaged over the range $4 \leq x/d \leq 30$, resulting in an experimental uncertainty of $\delta\eta$=0.071. The uncertainty estimate of $\delta\eta$=0.021 was, again, higher due to the dominating precision uncertainty resulting from

the surface temperature measurement. The spatially averaged bias uncertainty is presented in Table 2.7 and is estimated to be $\delta\eta$=0.020. It is similarly dominated by the bias uncertainty in the surface temperature measurement. The total uncertainty is again $\delta\eta$=0.028.

Table 2.6: Precision uncertainty calculations for spatially averaged adiabatic effectiveness.

Measured Parameter	Nominal Value	Measurement Uncertainty	Elemental Uncertainty
Surface Temperature with Film, T_f (K)	292.0	1.500	0.0157
Surface Temperature No Film, T_0 (K)	299.0	1.500	0.0143
Blowing Ratio, M	1.00	0.021	0.0011
Mainstream Temperature with Film, $T_{\infty,f}$ (K)	305.0	0.013	0.0001
Mainstream Temperature No Film, $T_{\infty,0}$ (K)	305.0	0.013	0.0001
Coolant Temperature with Film, $T_{c,f}$(K)	203.3	0.013	0.0000
Calculated η	**0.073**		
Precision uncertainty, $\delta\eta$	**0.021**		

Table 2.7: Bias uncertainty calculations for spatially averaged adiabatic effectiveness.

Measured Parameter	Nominal Value	Measurement Uncertainty	Elemental Uncertainty
Surface Temperature with Film, T_f (K)	292.0	1.20	0.0125
Surface Temperature No Film, T_0 (K)	299.0	1.20	0.0115
Blowing Ratio, M	2.00	0.07	0.0037
Heat Transfer Augmentation, h_f/h_0	1.00	0.20	0.0091
Mainstream Temperature with Film, $T_{\infty,f}$ (K)	305.0	0.00	0.0000
Mainstream Temperature No Film, $T_{\infty,0}$ (K)	305.0	0.00	0.0000
Coolant Temperature with Film, $T_{c,f}$(K)	203.3	1.00	0.0007
Aluminum Temperature, T_{Al} (K)	203.3	3.00	0.0001
Calculated η	**0.073**		
Bias uncertainty, $\delta\eta$	**0.020**		

Chapter Three

Experimental Results

This chapter presents and discusses the adiabatic effectiveness measurements obtained for the various crossflow configurations as well as the standard plenum condition.

3.1 TEST CONDITIONS

The testing parameters for this study are listed in Table 3.1 with the only exception being the plenum condition in which the internal Reynolds number is of no consequence. Relative errors for the parameters are listed beside their values; however, the majority of tests yielded errors significantly less than those listed. Table 3.2 lists the dimensional parameters of the test for reference.

Table 3.1: Test parameters

Test Parameter	Value*
Internal Reynolds	$35{,}000 \pm 2000$
External Reynolds	$4{,}400 \pm 35$
External Turbulence	5.0%
DR	$1.5 \pm .02$
M	$0.50, 0.75, 1.0, 1.5, 2.0 \pm 0.03$
* $\pm$ indicates acceptable experimental operating range	

Table 3.2: Dimensional test parameters

Dimensional parameter	Value
Hole diameter (d)	5 mm
Injection angle (α)	30°
Orientation angle (β)	45°
Hole length (l/d)	6
Number of holes	8
Wall thickness (t)	$3d$ (15 mm)
Hole spacing (P)	$6.25d$ (31.25 mm)
Internal coolant channel cross-section (W x H)	$5d$ x $14d$ (25 mm x 70 mm)
Rib cross-section (W x H)	$1.25d$ x $1.25d$ (6.25 mm x 6.25 mm)
Rib spacing ($2P$)	$12.50d$ (62.50 mm)

Adiabatic effectiveness measurements were taken for a total of nine experiments. Each of the four internal crossflow configurations consisted of two tests with alternating coolant flow directions, each test gathering effectiveness data across the range of blowing ratios. As the test coupon was comprised of compound angled holes, the manner in which the coolant entered the hole differed according to the direction of perpendicular crossflow. The direction of coolant crossflow was either in-line or counter to the spanwise direction of the compound angled holes Figure 3.1, and the terms "in-line" and "counter" will be used in this analysis to describe the respective internal crossflow directions. The plenum configuration, having no internal crossflow, consisted of only one test. Each test gathered adiabatic effectiveness data for a range of blowing ratios from $M = 0.5$ to 2.0 ($I = 0.17$ to 2.7) at a density ratio $DR = 1.5$. Test-to-test repeatability

was performed for selected cases. Effectiveness data for selected blowing ratios common between tests had fairly good to excellent repeatability within uncertainty. In-test repeatability results at M = 1.00 were consistently within uncertainty and confirmed that uncertainty was dominated by biases.
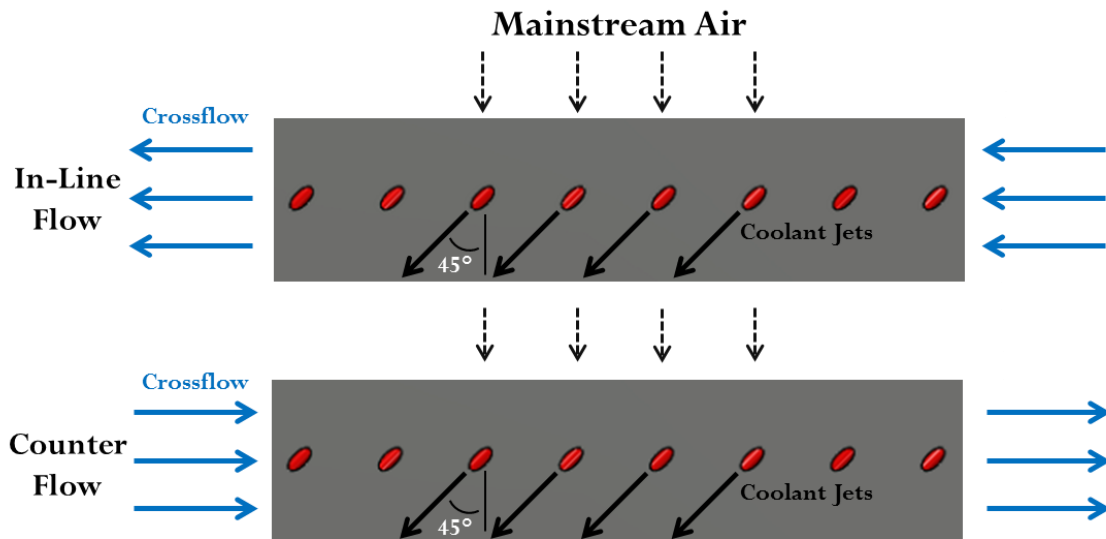
Figure 3.1: Terminology used in this study describing the direction of internal crossflow relative to the ejection angle of the film cooling holes

3.2 PLENUM AND SMOOTH-WALLED CROSSFLOW COMPARISONS

Film cooling adiabatic effectiveness measurements were made for cylindrical compound angled holes fed coolant by means of a quiescent plenum or spanwise internal crossflow. A comparison of spatially averaged adiabatic effectiveness data between the plenum and crossflow, smooth-walled tests are shown in Figure 3.2. The presented spatially averaged adiabatic effectiveness values are based on averaging over a streamwise range $2 \leq x/d \leq 30$ for corresponding blowing ratios to provide an overview of the experimental results. The addition of crossflow resulted in higher adiabatic effectiveness levels for all tested blowing ratios except for at the blowing ratio $M=0.50$ where the plenum case had a small advantage.

71
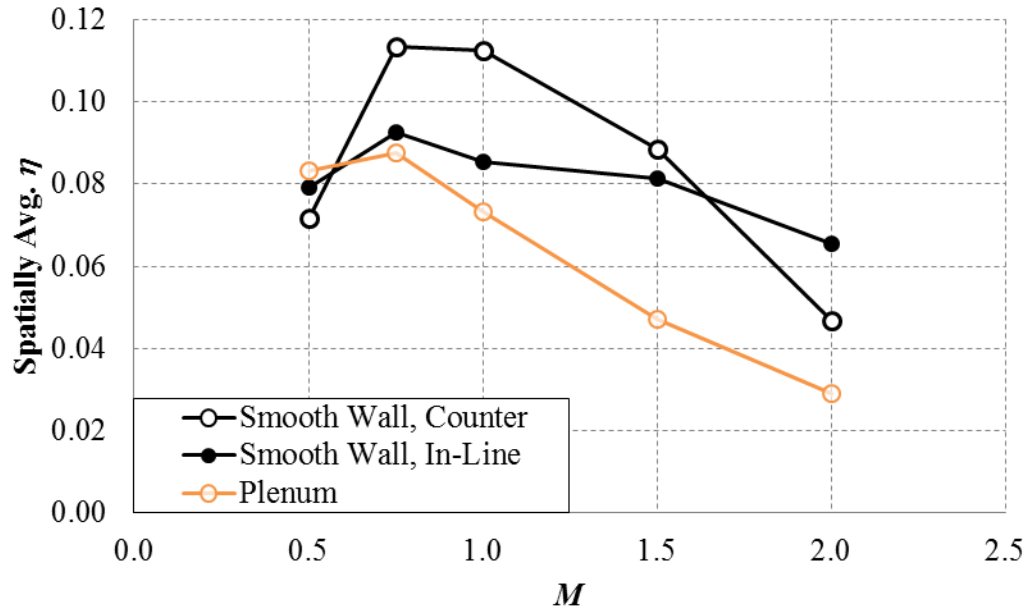
Figure 3.2: Comparison of spatially averaged effectiveness for plenum and crossflow, smooth wall configurations

For all three cases, peak adiabatic effectiveness levels occurred at M=0.75, but ensuing blowing ratios resulted in decreased adiabatic effectiveness, indicating increasing jet separation. However, the crossflow cases had extended optimum blowing ratio ranges with adiabatic effectiveness levels at M=1.0 similar to its peak levels at M=0.75. Both the plenum case and the smooth-walled counter flow cases were more sensitive to the blowing ratio and exhibited sharp declines in adiabatic effectiveness for increasing M following the optimum blowing ratio range. In contrast, the smooth-walled in-line crossflow case had more sustained levels of effectiveness throughout the range of blowing ratios, resulting in higher levels of adiabatic effectiveness at M=2.0. Considering the smooth-wall internal crossflow cases, note that the direction of crossflow significantly affects the adiabatic effectiveness levels especially in the optimum blowing ratio range $0.75<M<1.0$. Spanwise or laterally averaged adiabatic effectiveness at M=0.75 presents the first indications of jet separation and reattachment in the near-hole

72

region for the crossflow cases (Figure 3.3). The local minima for the crossflow cases suggest jet separation, and the subsequent local maxima suggest additional coolant covering the surface from partial jet reattachment. The higher adiabatic effectiveness values for the in-line crossflow for $5<x/d<50$ coupled with its lower local minimum suggests a larger degree of jet separation and reattachment. The local minimum persists for increasing blowing ratios and is more prominent for the in-line case at $M=2.0$ (Figure 3.4). A full family of laterally averaged ($\bar{\eta}$) curves for the plenum and smooth-walled crossflow cases can be found in Appendices C.1 and C.2. Note that the small irregularities in the adiabatic effectiveness curves seen at $x/d = 16$ are the result of an abrupt change in physical boundary conditions. That location marks the junction between the test coupon and downstream flat plate, of which the latter experiences no internal coolant conduction effects through its surface. The jump in the data around $x/d = 32$ occurred due to the stitching of the upstream and downstream images from two cameras. The cameras agreed within uncertainty.
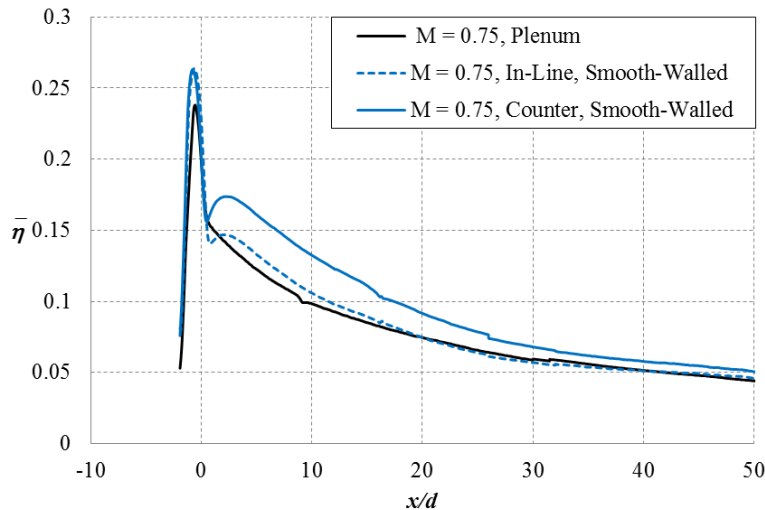
Figure 3.3: Comparison of laterally averaged data at *M*=0.75

73
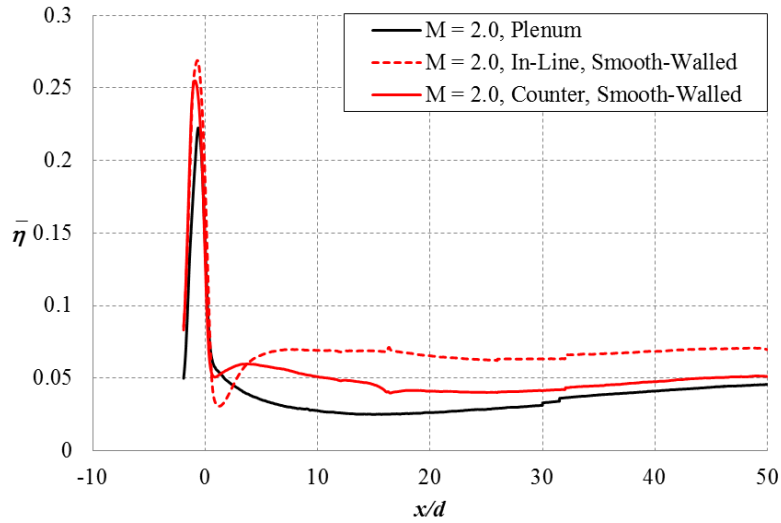
Figure 3.4: Comparison of laterally averaged data at *M*=2.0

Considering the adiabatic effectiveness contour plots help explain observations made from the averaged adiabatic effectiveness data. Plots were selected in Figure 3.5 at blowing ratios of *M*=0.75 and 2.0 because they represented the cases with maximum effectiveness and most significant jet separation, respectively. It should be noted that the in-hole contour levels for the plenum jet differ from the remaining compilation due to a change in camera angle, for which a calibration was performed. At a blowing ratio of *M*=0.75, the counter jet outperforms the in-line jet with increased lateral spreading and downstream coverage. While the counter jet is easily turned by the mainstream, the in-line jet resisted turning. This indicates that the coolant immediately adjacent to the surface for the counter case had lower localized momentum than the in-line case, despite the fact that the average fluid momentum exiting out the holes was the same. For *M*=2.0, the increased average momentum of the jets caused greater separation and an increasingly asymmetrical profile. The in-line jet separates more from the surface than the counter jet and exhibits a more pronounced shift in the spanwise direction. Despite its increased detachment the in-line jet has a wider profile with greater downstream coverage,

74

suggesting that jet reattachment more than made up for its initial separation. This supports the laterally averaged effectiveness graph in Figure 3.4 and the previous interpretation of the in-line crossflow jet separation and reattachment. This may be the result of jet flow structures more positively interacting with the mainstream to force the coolant back to the surface.

Although instinctively counterintuitive due to the sharp turn in which the coolant entered the hole, the performance of the smooth-walled counterflow case was significantly better than the in-line crossflow for the optimum blowing ratio range. This result appears to be contrary to the Wilfert and Wolff (2000) study described in Chapter 1.2.3, which found that aligning the internal coolant flow with the hole's axis resulted in significant effectiveness gains. However, the comparisons made within the study might not be as straightforward due to the addition of ribs and a vortex generator. Both of these factors introduce complex, three-dimensional flow structures into the flow field; therefore, it would be difficult to conclude how the coolant entered the holes with respect to the baseline case without additional flow field measurements. However, Gritsch et al. (1998) found that 90° crossflow, which would require the coolant to make a sharp turn into the hole's inlet, resulted in significantly better adiabatic effectiveness levels when compared to 0° crossflow, which would allow the coolant to enter the hole's inlet more aligned with the hole's axis. This study from Gritsch et al. (1998) provides a better comparison to the current experimental results, as it was similarly performed with a smooth-walled channel. Adiabatic effectiveness differences could also be explained by skewed exit jet profiles and in-hole vertical structures, both of which are discussed further in section 3.4.
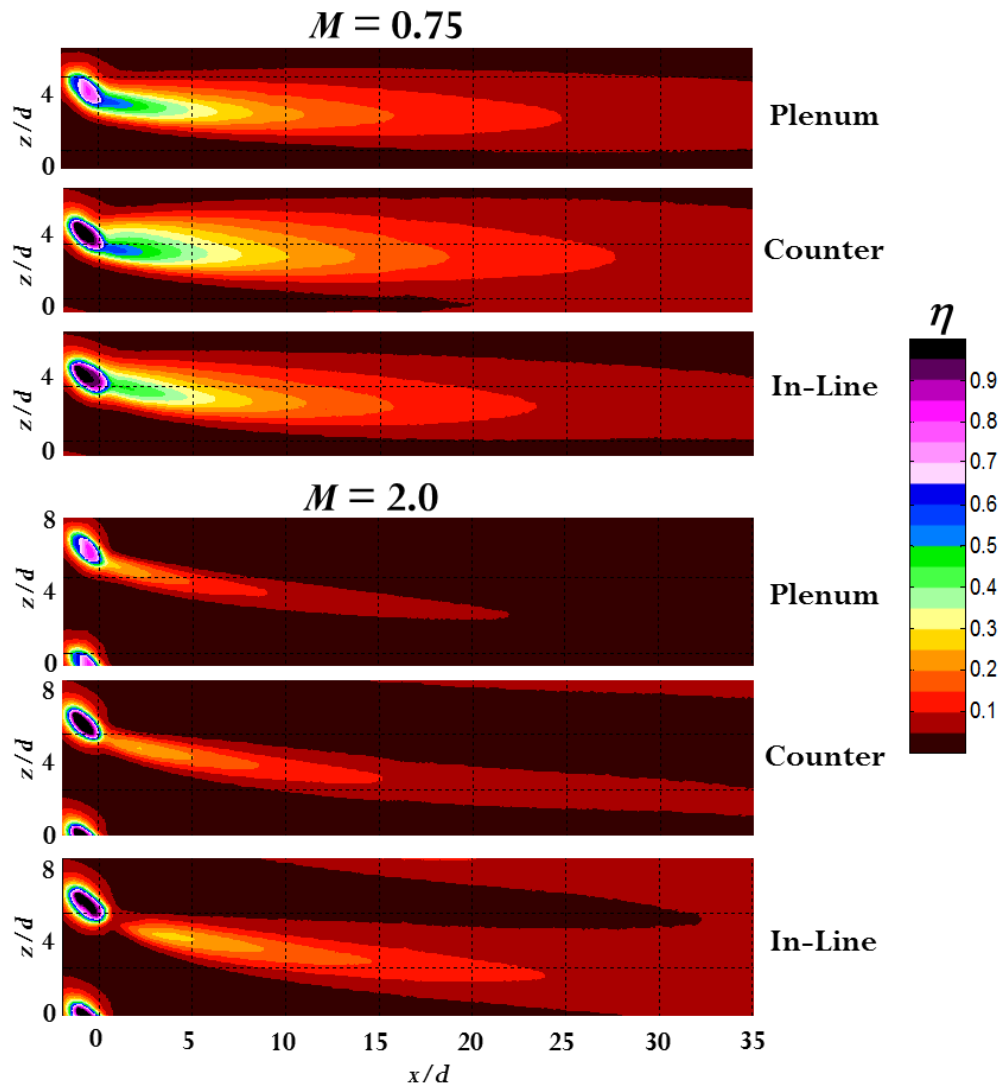
Figure 3.5: Contour plots for plenum and smooth wall crossflow configuration at *M*=0.75 and 2.0.

Adiabatic effectiveness measurements from the plenum case with compound angled holes can be compared to literature. Mayhew et al. (2004) had more similar testing and geometric conditions but had limited effectiveness data suitable for convenient comparisons. A single film cooling hole was used for the experiments, and spatially averaged effectiveness data was compiled from $-3 \leq z/d \leq 3$ for the low turbulence case and $-1.5 \leq z/d \leq 2.5$ for the high turbulence case. Singular data points for each

turbulence condition are shown in Figure 3.6 along with a more complete set of spatially averaged adiabatic effectiveness from Schmidt et al. (1996). All data points are representative of effectiveness measurements from $3 \leq x/d \leq 15$. The general trend of decreasing adiabatic effectiveness for both the current experiment and Schmidt et al. (1996) agree reasonably well, and quantitative differences in the effectiveness values can likely be attributed to the different operating conditions used by the various tests. Schmidt et al. (1996) used a row of holes with a slightly larger 60° compound angle. An increased orientation angle has been generally shown experimentally by Ekkad et al. (1997) and numerically by McGovern et al. (1997) to enhance adiabatic effectiveness. Note also the discrepancy between turbulence levels among the tests, a factor which at high levels can significantly diminish performance, especially at lower blowing and momentum ratios. However, Lutum and Johnson (1999) documented the effects of varying non-dimensionalized hole lengths l/d for axial holes and found that shorter length holes generally underperformed when two holes of $l/d \leq 5$ were compared. Holes with non-dimensionalized lengths longer than $l/d \geq 5$ and at higher momentum flux ratios showed little to no difference in effectiveness values. Despite this, no studies have documented the effects of varying the hole length l/d for compound angle holes. A second plenum comparison between the current experiment and Ligrani et al. (1994) can be found in Figure 3.7 for laterally averaged effectiveness data for varying mass flux ratios, which scaled better to the current experiment than momentum flux ratios. Ligrani et al. (1994) also had low levels of turbulence in addition to a more shallow injection angle of $\alpha=24°$ and a slightly larger hole spacing dimension. The hole spacing for Ligrani et al. (1992) was $p/d=7.8$ compared to the current experiment's $p/d=6.25$; therefore, the laterally averaged adiabatic effectiveness values for Ligrani et al. (1992) were correlated for comparison purposes according to the direct correlation found in

Schmidt et al. (1996). Due to the limited data points in Ligrani et al. (1994), accurate spatially averaged effectiveness comparisons could not be made with Figure 3.3.7.
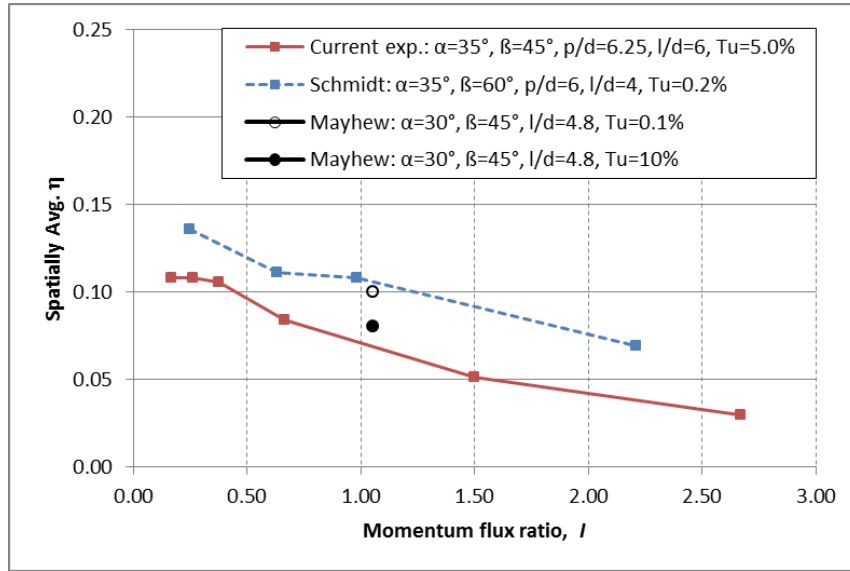
Figure 3.6: Spatially averaged effectiveness comparison between current experiment, Schmidt et al. (1996), and Mayhew et al. (2004).
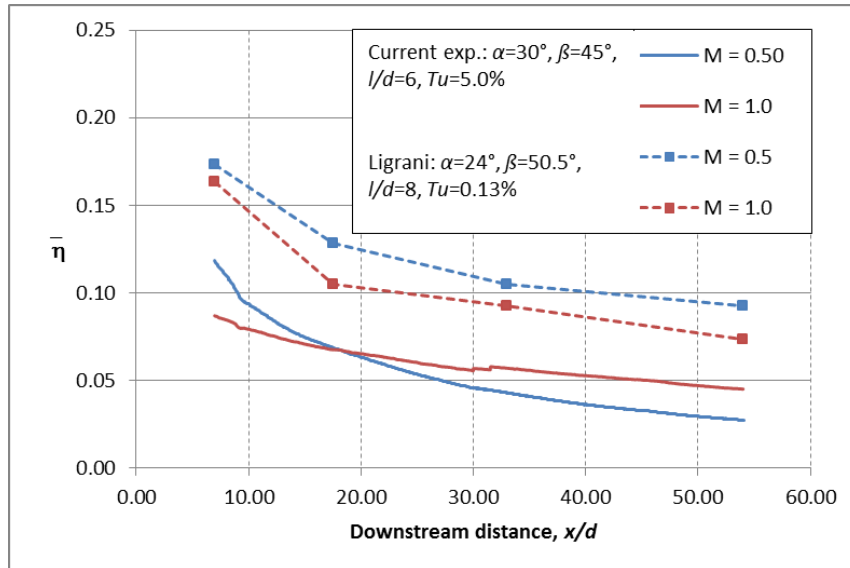
Figure 3.7: Laterally averaged effectiveness comparison between current experiment and Ligrani et al. (1992). The adiabatic effectiveness values for Ligrani et al. (1992) with a hole spacing _p/d_=7.8 has been correlated to the hole spacing _p/d_=6.25 for the current experiment.

78

3.3 INFLUENCE OF RIB CONFIGURATIONS

Adiabatic effectiveness measurements were taken for three different rib configurations termed aligned mid-pitch, aligned over-hole, and perpendicular mid-pitch. Ribs were angled to the direction of incoming internal crossflow and diverted the coolant either forwards or backwards with respect to the direction of the mainstream, shown in Figure 3.8. Therefore, the terms "forward" and "backward" may be used to distinguish the crossflow orientation within each rib configuration. Comparisons of adiabatic effectiveness among all tested configurations will be made with a special emphasis on the influence of ribs within the channel.
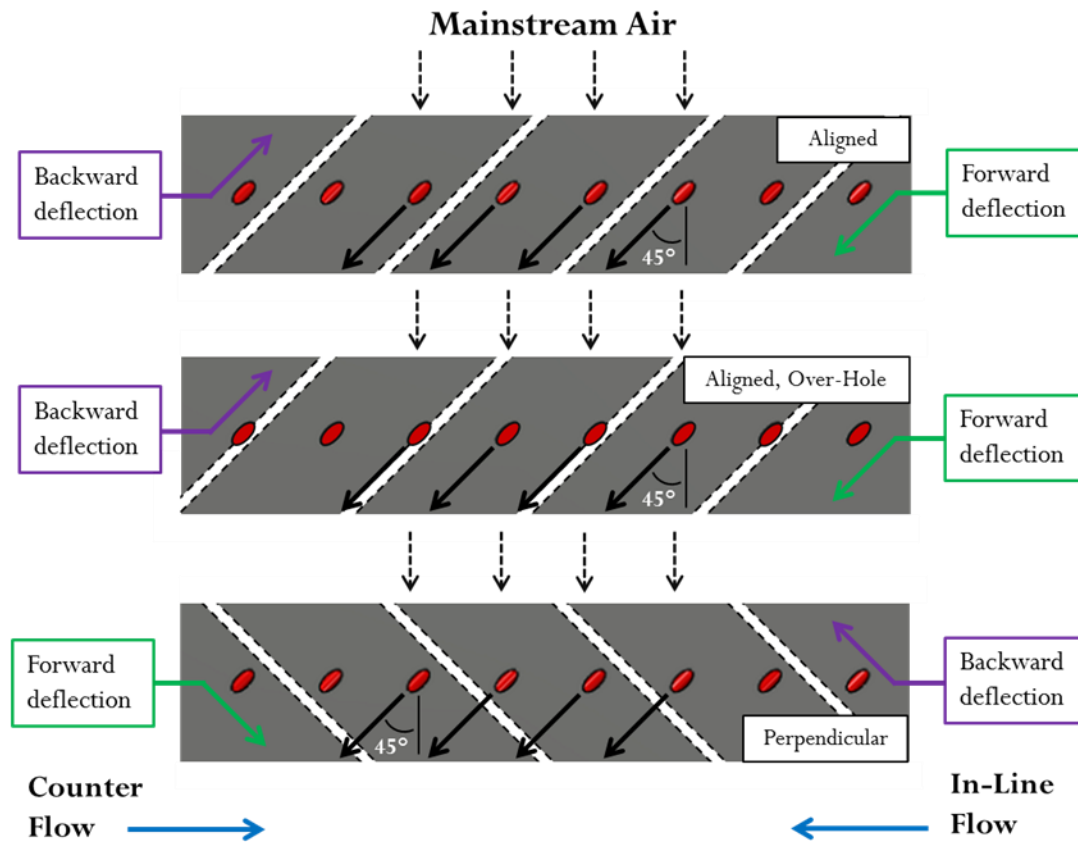
Figure 3.8: Schematic of rib configuration terminology.

Due to the large number of experiments completed, spatially averaged adiabatic effectiveness ($\overline{\overline{\eta}}$) distributions are shown in Figure 3.9. The spatial average was taken across one rib pitch containing two film cooling holes and over the range $4 \leq x/d \leq 30$. The smooth-walled, counterflow case retains the highest levels of adiabatic effectiveness in the optimum blowing ratio range among all configurations tested. Even when considering the comparison to the worse-performing no ribs case with in-line crossflow, the addition of ribs in all cases but one had either decreased or similar adiabatic effectiveness for $M>0.50$. The only rib configuration that performed similarly or better than the no ribs in-line case was the perpendicular ribs, counter (forward deflecting) case at a blowing ratio of $M=1.0$. As a result, the perpendicular rib case with counter crossflow is the best performing rib configuration for the range of optimum blowing ratios. Peak adiabatic effectiveness levels for the remaining plenum and rib cases were very similar, although the majority occurred closer to a blowing ratio of $M=0.75$. Only the aligned and perpendicular ribs with counter crossflow had the optimum blowing ratio shifted closer to $M=1.0$. The majority of the cases exhibited steep drop-offs in effectiveness for blowing ratios outside of their respective optimal ranges. The smooth-walled, inline case was the least affected by jet separation resulting from higher blowing ratios.
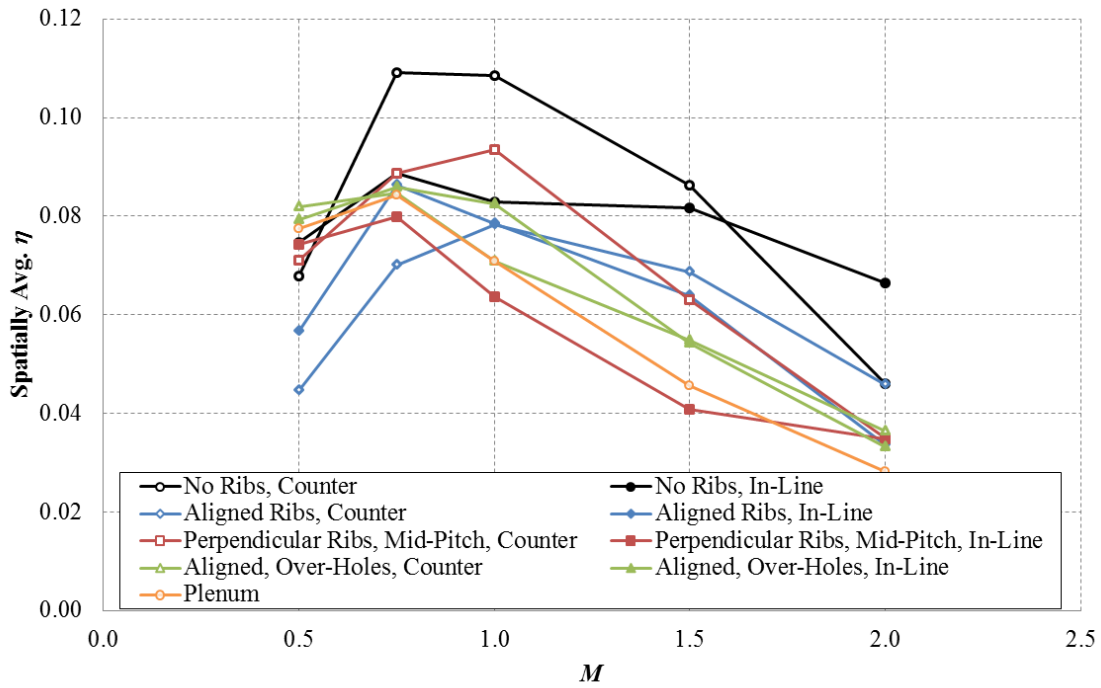
Figure 3.9: Compiled spatially averaged adiabatic effectiveness measurements for all tests for 4≤x/d≤30.

Although no generalizations can be made about optimum effectiveness values preferential to a particular crossflow direction in relation to the hole, it can be observed that it favors a particular rib deflection. The optimum crossflow direction within each rib orientation promoting higher and more sustained peak effectiveness levels consisted of forward deflecting ribs. Furthermore, forward deflecting ribs are less sensitive to crossflow direction.

Not only did the perpendicular rib configuration attain the highest levels of peak effectiveness among all rib configurations, but it shares a few common characteristics with other configurations. Change in crossflow direction was only significantly important for the no ribs and perpendicular cases and to a greater extent in the region of optimum blowing ratios. A blowing ratio of M=1.0 for both configurations yielded the greatest disparities in effectiveness levels found among any of the crossflow cases. The perpendicular ribs were exceptionally sensitive to crossflow direction, as its in-line

81

crossflow case exhibited a steep decline in effectiveness after its peak around *M*=0.75. Rather than mirroring the effectiveness drop following the peak effectiveness experienced by the in-line crossflow case, the spatially averaged effectiveness for the counter crossflow case slightly increased until its peak was attained around *M*=1.0. A graph comparing laterally averaged data for the perpendicular crossflow tests is shown in Figure 3.10 to further illustrate this point. The counter crossflow cases exhibited local minima in the near hole region starting at *M*=0.75, indicating jet separation from the surface. Increasing the blowing ratio to *M*=1.0 furthered this effect and resulted in decreased effectiveness in the near hole region; however, increases in effectiveness beyond *x/d*=6 resulted in slightly better spatially averaged effectiveness levels. Considering in-line crossflow at *M*=1.0, $\bar{\eta}$ values conversely had consistently worse levels than for *M*=0.75 through *x/d*=38. This reversal contributed to the significant disparity in effectiveness levels between the two crossflow cases at *M*=1.0.
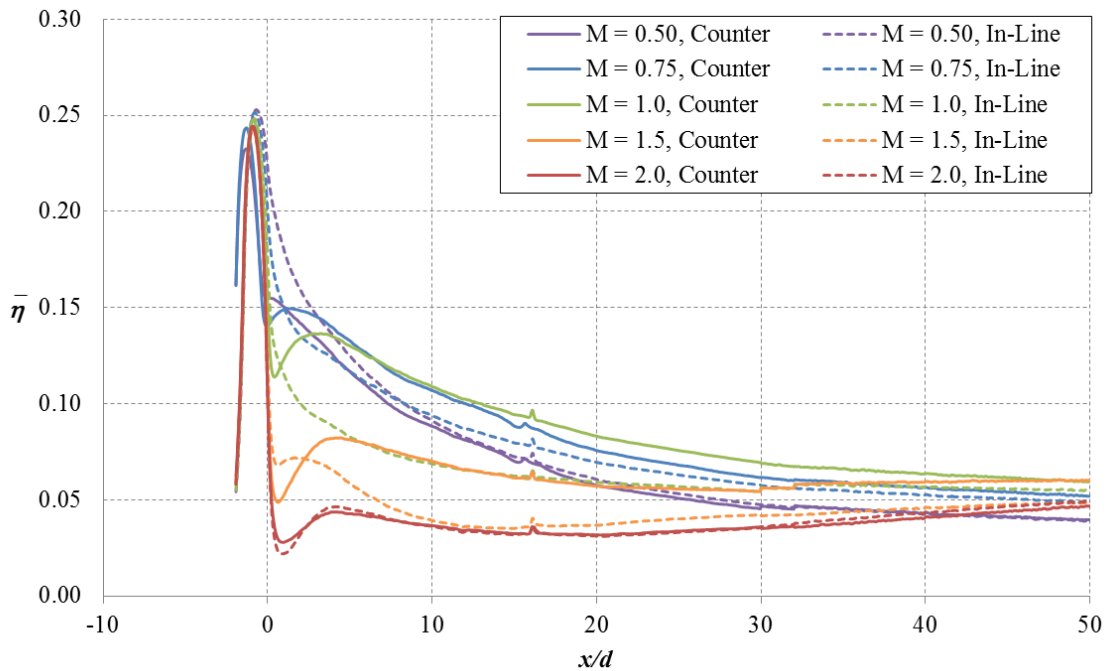
Figure 3.10: Laterally averaged data for perpendicular ribs configuration.

The difference can be attributed to the individual performances of the holes. It is worth noting that although the momentum flux ratio is defined as an average across the holes, individual holes in a row can be susceptible to deviations in the amount of coolant ejected. The addition of ribs in the channel creates localized pressure gradients which can affect the coolant mass flux exiting the hole, thus creating hole-to-hole variances in blowing ratio. Pre-rib hole (defined as a hole immediately upstream of a rib) inlets experience a higher localized pressure which drives more coolant through the holes. Post-rib hole (defined as a hole downstream of a rib) inlets located within the separation zone are subjected to lower localized pressure resulting in less coolant entering the hole. Viewed in isolation, the differences in localized channel pressure and the resulting exiting coolant mass flux should influence the downstream adiabatic effectiveness. Examples of pre- and post-rib hole adiabatic effectiveness can be thought of in reference to cooling holes in a standard smooth-walled case. At low blowing ratios below the standard optimum coolant mass flux range, pre-rib holes operating under higher localized channel pressure would be expected to attain higher downstream adiabatic effectiveness values based on their ability to provide more coolant to the surface. At high blowing ratios above the standard optimum range, the significantly deleterious effects of jet separation from the surface would be expected to diminish due to post-rib holes operating under lower localized channel pressure, thus resulting in higher adiabatic effectiveness values.

Considering again the perpendicular ribs case, the cause of the effectiveness disparity of the alternate crossflow directions seen in Figures 3.9 and 3.10 is readily apparent when inspecting the performance of individual holes. The performances of each hole separately are presented in terms of $\bar{\bar{\eta}}$ in Figure 3.11. The in-line crossflow (backward deflecting), post-rib hole experiences a small decrease in spatially averaged

adiabatic effectiveness for blowing ratios M=1.5 and M=2.0 but is relatively unaffected by crossflow direction for the remaining blowing ratios. For the in-line crossflow with backward deflecting ribs, the pre-rib experiences decreasing effectiveness values for increasing blowing ratios. However, for the counter crossflow with forward deflecting ribs, the pre-rib shows effectiveness increases for increasing blowing ratio before sharply declining at M>1.0. Therefore, it can be concluded that the pre-rib hole is extremely sensitive to crossflow direction and is the dominant factor in overall performance. However, no broad generalizations can be made for the positive effects of forward directing ribs and pre-rib holes, as both the aligned and aligned, over-hole configurations have decreased effectiveness values (Figures 3.12 and 3.13). In fact, among all three different rib configurations, neither the pre-rib nor the post-rib hole consistently outperformed the other. This suggests that the variances in internal local pressure experienced by the pre- and post-rib hole inlets alone cannot adequately explain the differences in effectiveness values for the rib cases tested. Although local internal pressure affects hole-to-hole blowing ratios, the flow coolant flow rate through a hole is probably not exclusively dependent on local static pressures. The internal channel flow field, particularly when considering the three-dimensional complexity of flow over ribs, most likely affects the flow volume entering holes. Furthermore, although the amount of coolant exiting a hole is well known for its influence on adiabatic effectiveness, literature has also suggested that adiabatic effectiveness can be affected jet flow structures and exit velocity profiles (Walters and Leylek (1997) and Thole et al. (1997)). This has also been proven to originate from the manner in which coolant enters a hole, a condition that varies among the rib cases for pre- and post-rib holes due to the different positioning of the ribs in relation to the holes. Therefore, because variances in internal local pressure cannot consistently predict a cooling hole's effectiveness, it is likely that the internal

channel flow field, exit velocity profiles, or jet flow structures also had a significant impact on an individual hole's performance.
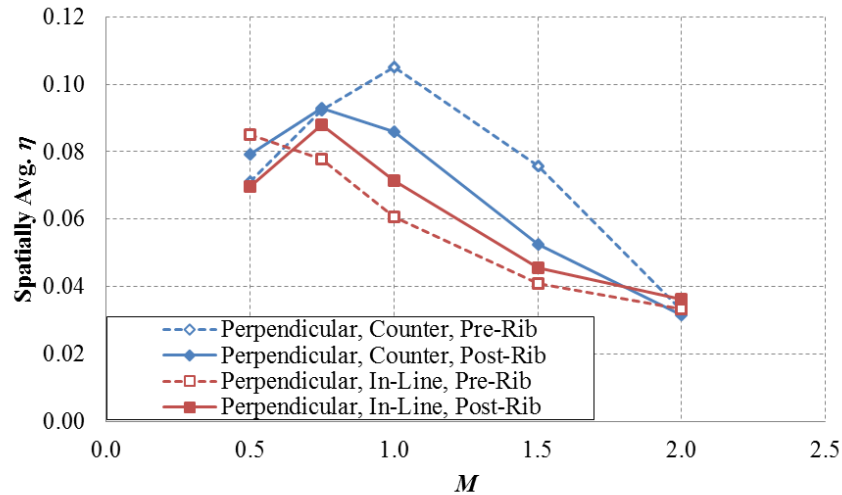
Figure 3.11: Spatially averaged data for individual holes - perpendicular rib configuration.

Effectiveness measurements taken for the aligned, over-hole rib configuration showed that a hole which intersects a rib still maintains moderate levels of effectiveness. Spatially averaged η distributions from Figure 3.9 show that comparisons between the aligned and aligned, over-hole rib configurations are relatively small.
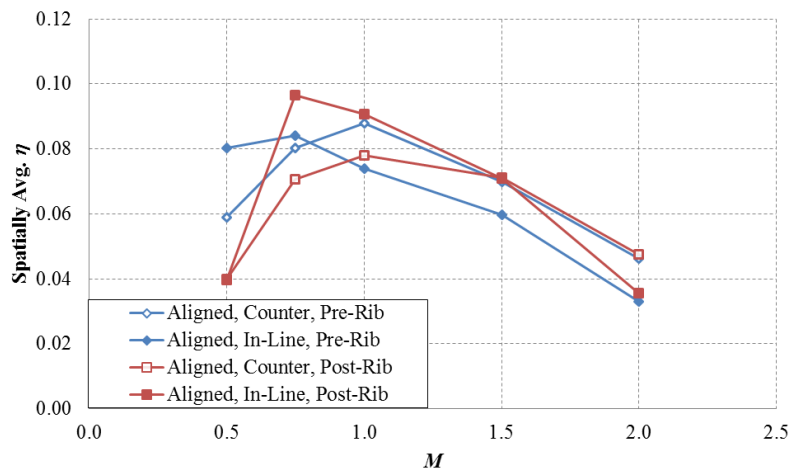
Figure 3.12: Spatially averaged adiabatic effectiveness for individual holes - aligned case.

85
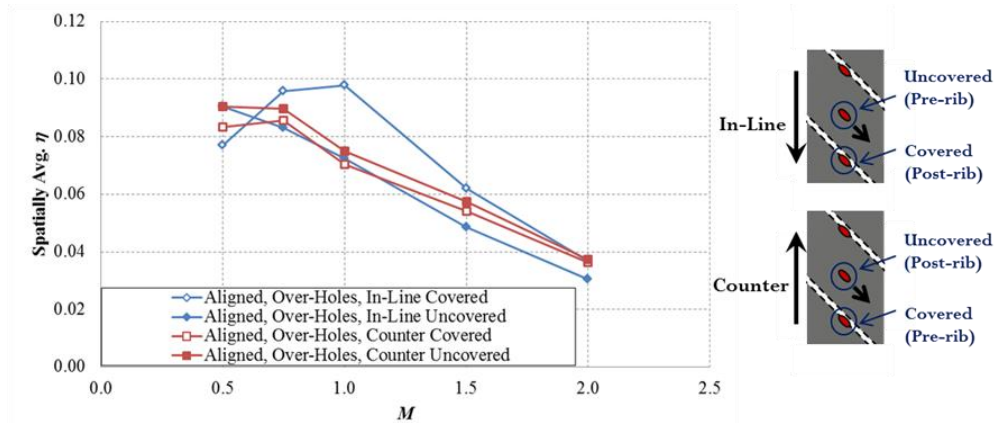
Figure 3.13: Spatially averaged adiabatic effectiveness for individual holes - aligned, over-holes case.

Aligned, over-hole configurations had similar or better peak effectiveness than aligned rib configurations and, with the notable exception of the perpendicular counter crossflow case, also compared favorably to the rest of the rib configurations. Families of curves for both aligned configurations can be found in Appendices C.4, C.5, and C.6. The aligned, over-hole tests actually outperformed all other crossflow configurations at a blowing ratio of M=0.50. Note that alternating crossflow direction makes little difference to the effectiveness levels except at *M*=1.0. The increased effectiveness can be explained by examining the performance of the individual holes and can be attributed to the in-line crossflow, covered hole (defined as the hole which intersects the rib) as seen in Figure 3.13. Interestingly, despite being located partially in the rib and immediately in its separation region, this hole produced the highest levels of effectiveness. Examination of jet contours at a blowing ratio of M=1.0 yield the conclusion that the hole in question produced wider and longer jet resulting in greater effectiveness (Figure 3.14).
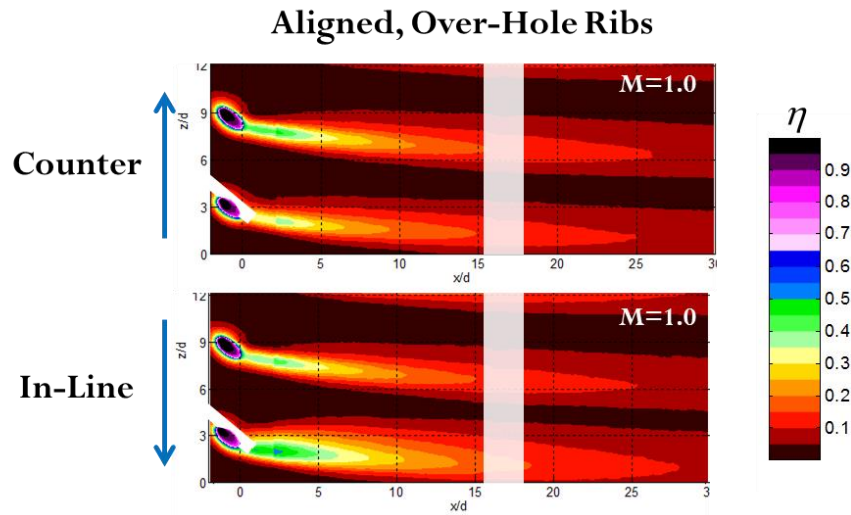
Figure 3.14: Contour plots displaying adiabatic effectiveness at *M*=1.0 - aligned, over-holes case.

A comprehensive compilation of η contours for individual jets for all tests is shown in Figure 3.15. Optimum blowing ratios for the peak effectiveness levels were chosen for each respective configuration. Therefore, the counter crossflow aligned and perpendicular rib configurations have jets at M=1.0 while the remaining jet profiles are representative of a blowing ratio of M=0.75. The transparent white rectangular bars covering 15.5<*x/d*<17 for the aligned, over-holes rib configuration (4) have been inserted as a result of emissivity errors. Spackle was used to fill in the seam at the intersection of the test coupon and downstream flat plate, and although localized emissivity errors were introduced, the results of the test were not negatively affected. Additionally for the aligned, over-holes rib configuration, a discontinuity appears at *x/d*=2 due to the change in conduction correction techniques. Data for *x/d*<2 has not been regarded as reliable due to large conduction errors, so the three-dimensional conduction correction was only applied for data *x/d*≥2 (Appendix C.3). Duplicate jets for the plenum condition (1) have been arranged side-by-side for easier comparison to the other configurations. The in-hole contour levels for the plenum jet differ from the remaining compilation due to a change

in camera angle. A camera calibration for the new angle was performed. With the exception of the pre-rib jet for the aligned, over-hole configuration, all jets resulting from a "forward" deflection of the ribs outperformed their "backward" counterparts. Neither consistently increased jet width nor streamwise coverage could explain the increased effectiveness. As stated before, generalizations based upon hole positioning or crossflow direction cannot be made as no consistent trends for either supposition exist. The degree to which jets are shifted away from the centerline is also independent of any generalizations. However, it is evident why the counter smooth-walled case produced the highest levels of effectiveness. The jet is wider and travels further downstream than any other jet in the compilation. The pre-rib jet for the counter (forward deflecting) perpendicular ribs is the next best performing jet, containing skewed profiles that travel slightly less far downstream but are comparably wide. Note that the two most skewed jet contours consisting of the counter smooth- walled and perpendicular ribs configurations are the most effective out of the entire compilation. Despite its reduced effectiveness when compared to the smooth-walled counter crossflow case, counter perpendicular rib is best performing jet among all other rib configurations, and its counterpart post-rib jet is among those who cover the farthest distance downstream.
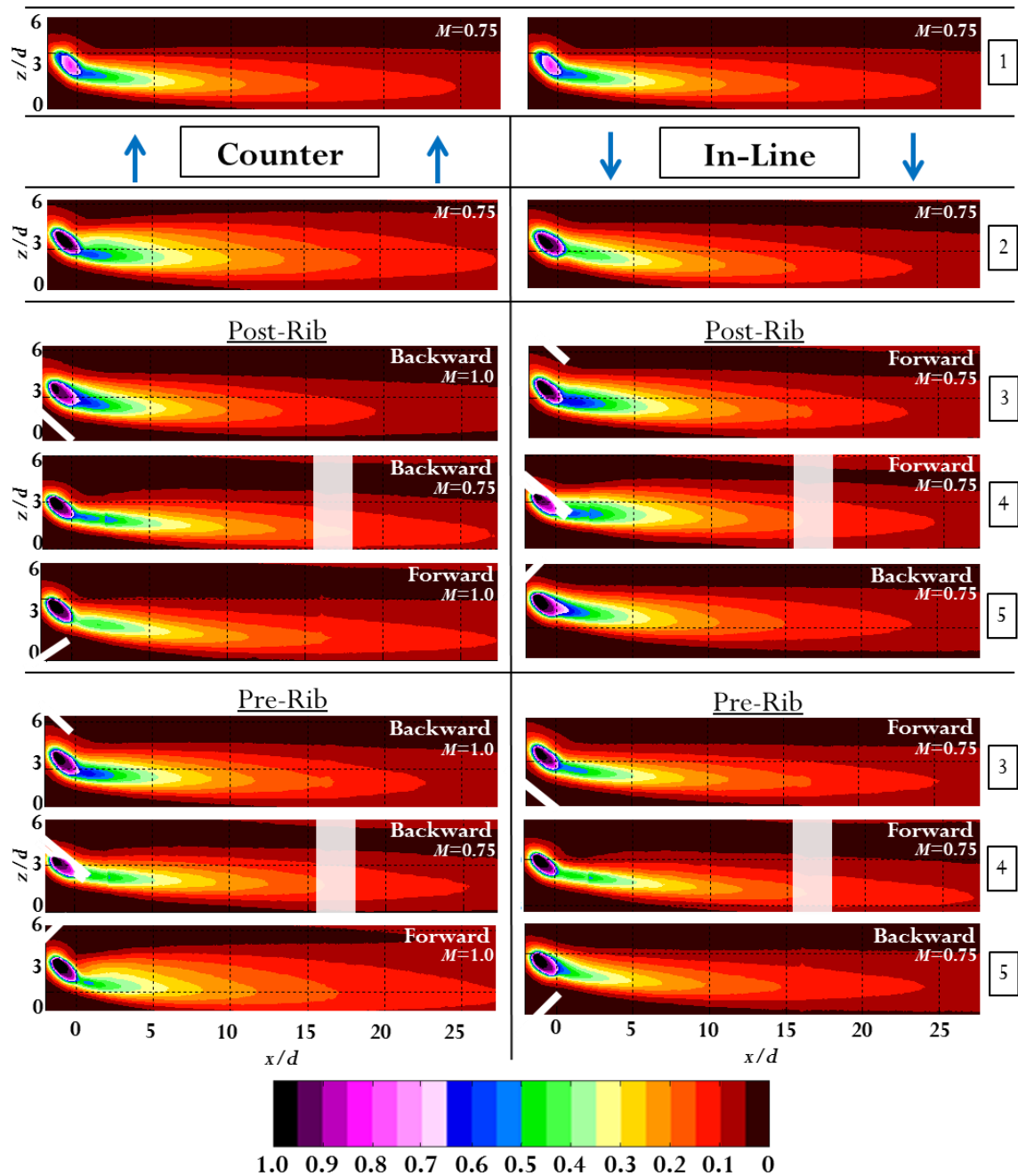
Figure 3.15: Contour comparisons for optimum blowing ratios for (1) plenum, (2) smooth-walled, (3) aligned, (4) aligned over-hole, and (5) perpendicular. The plenum jet (1) has been duplicated for easier comparison against the other jets. Rectangular bars over configuration (4) have been inserted due to localized emissivity errors.

3.4 EXPERIMENTAL CROSSFLOW RESULTS AND COMPARISON TO LITERATURE

Given that very few experimental studies available in literature have investigated the effects of crossflow on adiabatic effectiveness, comparisons of this study's measurements to literature are limited. However, Sakai and Takahashi (2011) performed a crossflow study with an axial hole including tests consisting of 30° forward and backward deflecting ribs. A spatially averaged η summary of the findings can be found in Figure 3.16 for a limited blowing ratio range of 0.4≤M≤0.75. Similar to the findings in this study, forward deflecting ribs performed better than backward ribs. However, the forward deflecting ribs resulted in higher effectiveness levels than the smooth-walled case. The current study found that at comparative blowing ratios, smooth-walled performed similarly or better than rib configurations. Furthermore, the peak effectiveness levels for the forward deflecting ribs have shifted to lower blowing ratios. Sakai and Takahashi (2011) found that changing the relative position of the hole to the ribs had a mild effect on performance, agreeing with the results of this study and Kunze and Vogeler (2013). The combination of this study's conclusion that configurations can be highly sensitive to blowing ratios coupled with the relatively small range of blowing ratios tested in Sakai and Takahashi (2011) limit any additional comparisons.

The current study showed that the implementation of ribs can cause significant decreases in external adiabatic effectiveness when compared to the baseline, smooth-walled crossflow case. Therefore, gas turbine designers must weigh whether the film cooling performance penalty caused by ribs could be offset by the increased internal cooling performance resulting from a higher internal heat transfer coefficient. This necessitates quantifying the individual contributions to the overall cooling of the surface from both internal and external cooling. Furthermore, the degree to which ribs augment surface cooling must also be determined. These parameters were investigated in Dees

(2010) in which experiments were conducted on a matched Biot airfoil. The matched Biot model more accurately represents an actual gas turbine blade or vane by scaling the ratio of external convective heat transfer to conduction through the surface. This method produces a consistent temperature profile from the internal passageways, through the surface, and to the external side of the surface. Results showed that internal cooling was a significant contributor to overall effectiveness and that ribbed channels generally increase overall effectiveness as well. The study noted that localized regions were not affected by implementing ribs due likely to separated internal channel flow. Inserting data from this flat plate study into the Dees (2010) airfoil study and drawing accurate conclusions about the overall benefits of using internal ribs would be dubious. However, acknowledging the relative positive effects of ribs on internal cooling coupled with its relative negative effects on external film cooling, it is certainly possible for ribs to have an overall positive effect when used in combination with film cooling, especially for higher momentum flux ratios. Developing a simple yet accurate and comprehensive method of arriving at that conclusion would be likely difficult, as this study has shown that film cooling can be very sensitive to hole inlet conditions that cannot yet be quantified. Film cooling is also a significant contributor to the overall effectiveness; therefore it would be difficult to generally assess the value of rib implementation on a blade or vane for a variety of test configurations and conditions, as those conditions can significantly influence the film cooling performance. It is more likely that a simple analysis for axial holes could be developed, as there is more literature devoted to axial holes than compound angle holes.
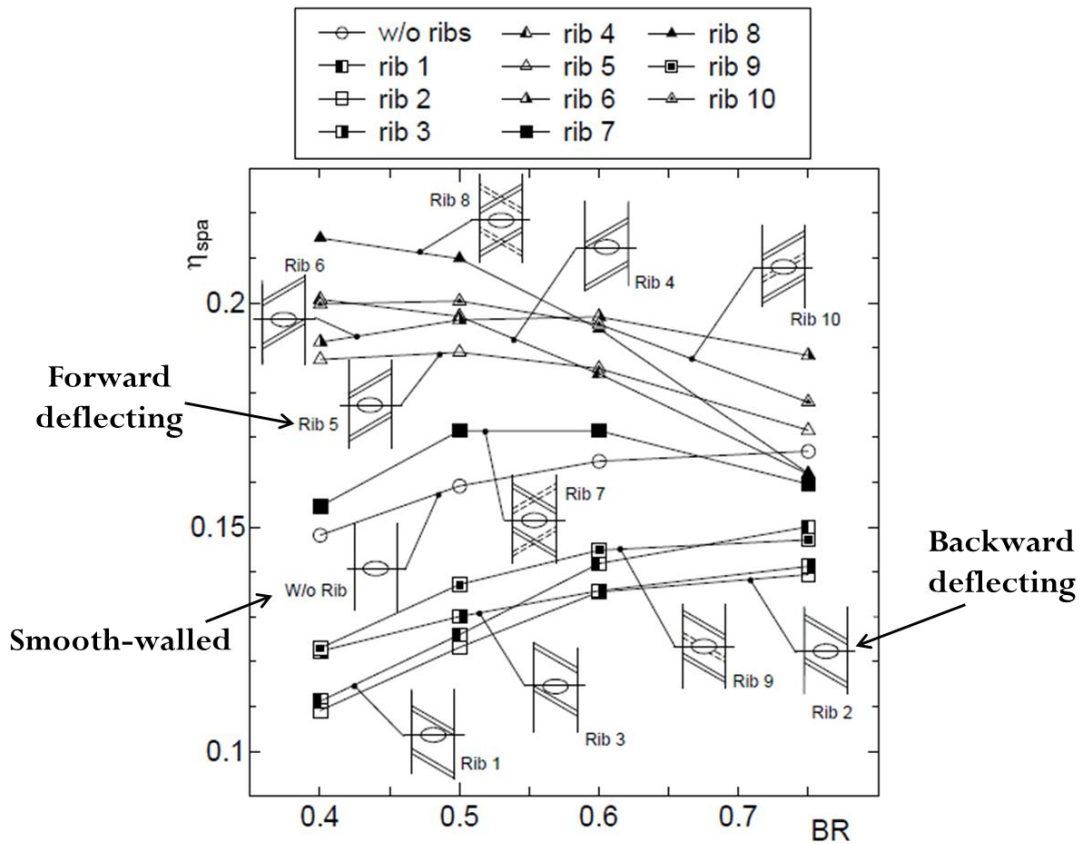
Figure 3.16: Spatially averaged adiabatic effectiveness experimental results for different rib cases, Sakai (2010).

Crossflow data from this cylindrical holes study should not be compared to tests with shaped holes. Gritsch et al. (2003) found that shaped holes responded quite differently to crossflow than cylindrical holes due to the highly disturbed flow field region inside of the diffuser section of the hole. As a result, accurate comparisons from compound angled shaped holes to cylindrical holes would likely not be achievable.

Considering previous literature, it is highly likely that the performance of the jets in this study was directly attributable to the manner in which coolant crossflow entered the holes. Taking the simplest crossflow smooth-walled case, the in-line crossflow should have entered the hole more smoothly and experienced fewer losses than the counter case. As shown by Thole et al. (1997), the sharp edges of the cooling hole inlet

caused entering coolant to form a separation zone within the hole and resulted in skewed exit profiles. Increased alignment of the coolant entry with the axis of the film cooling hole most likely reduced the separation zone and lead to diminished in-hole losses and turbulence. The coolant for the smooth-walled counter case was forced to enter the hole at a much sharper angle than the in-line case, most likely leading to more torturous in-hole vortices and a more skewed exit profile due to larger in-hole separation regions. It is possible that the in-hole vortices created a complex exit flow field that allowed coolant to better adhere to the surface. This supposition may be similar to the computational simulation from Agata et al. (2013) which showed that the vortical in-hole structures created a bifurcated "wall ward lump" of fluid that remained attached to the surface even for high blowing ratios (as described in Section 1.2.3). However, these claims cannot be verified without flow field measurements. Adami et al. (2002) showed in a CFD simulation that coolant spirals within the axial hole for 90° crossflow and that the combination of the blowing ratio, hole length, and hole diameter determined the exiting profile. This implies that it may be difficult to predict the exit profile due to its sensitivity to the operating conditions and geometries, especially when ribs are involved.

Nevertheless, physical manifestations of the jet contours in Figure 3.15 after exiting the hole may provide insights. The singularly skewed contours of the two best performing jets (smooth-walled counter and perpendicular ribs counter) imply that coolant exiting included complex vortical structures that enhanced coolant adherence to the surface and lateral spreading. It is possible that the increased effectiveness for these cases is the result of separation regions formed within the hole. Although the average momentum across the holes remains unchanged, skewed exit jet profiles can cause parts of the jet to have localized variances in momentum. A separation region on the downstream edge of the hole (with respect to the hole's axis) would cause low

momentum fluid to exit from the downstream edge of the hole, resisting separation and adhering more effectively to the surface. Simultaneously, high momentum fluid would leave from the upstream edge and more effectively shield the upstream mainstream flow from negatively interacting with the low momentum coolant on the surface. Results from the contour plots may justify these claims. Considering the smooth-walled configuration, the counter crossflow jet was more easily turned by the mainstream than its in-line crossflow counterpart, indicating diminished momentum of the coolant immediately above the surface.

As the in-hole losses have been previously shown by literature to be affected by the hole inlet conditions, an examination of the internal crossflow conditions is warranted. The different rib configurations affect the internal flow field as coolant interacts with the obstructions. Fluid encountering an angled rib will tend to leave the rib at a similar angle. Like the mainstream turning jets from compound angled holes, the bulk momentum of the crossflow will tend to straighten out the angled deflection of the coolant leaving the rib. A schematic is shown in Figure 3.17 to illustrate coolant deflections immediately following contact with the ribs. As coolant progresses down the rib pitch, it is likely that these deflection angles will rotate towards the smooth-walled cases due to the momentum of the bulk internal crossflow coolant (as depicted by the red, dashed arrows).
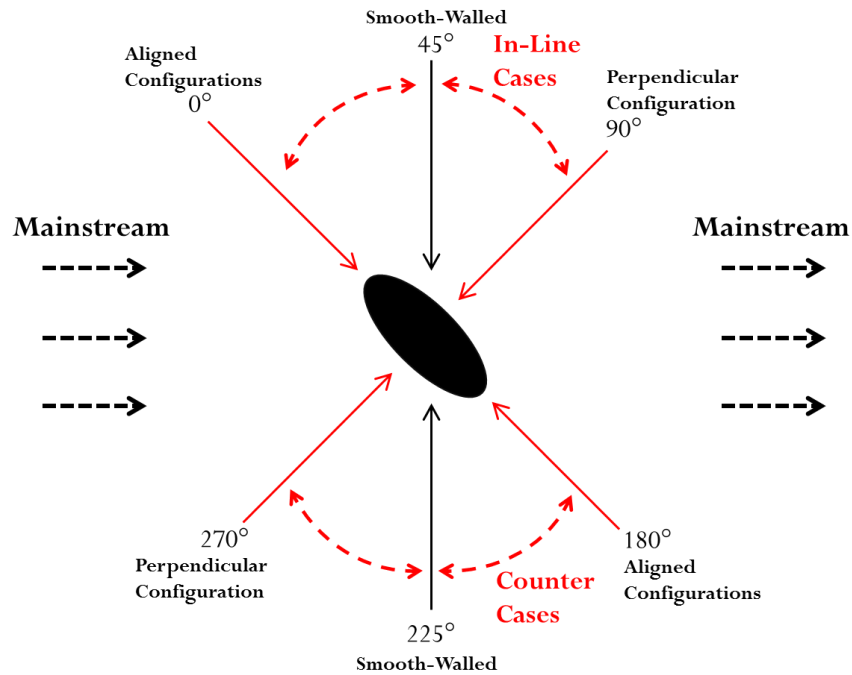
Figure 3.17: Schematic of possible internal coolant deflection angles in relation to the hole. The smooth wall cases are listed as references.

However, approaching this from a strictly two-dimensional standpoint is inherently flawed. The existence of ribs in the channel will tend to deflect the coolant in a certain direction for a limited distance, but previous literature has shown that the interplay of the bulk crossflow, separation regions, and wall effects create a highly complex three-dimensional flow field, especially when considering the possibility of reverse flow caused by separation regions (Casarsa and Arts (2005)). Without a proper inspection of the internal channel flow field, especially near the hole inlet, any reasoning given concerning the coolant entrance into the hole is merely speculative.

Chapter Four

Conclusions

4.1 SUMMARY AND ANALYSIS OF RESULTS

Film cooling effectiveness measurements were taken to investigate the combined effects of 45° compound angled holes, crossflow oriented perpendicular to the mainstream flow, and various rib configurations. Crossflow results were compared to a standard plenum condition. A total of nine experiments were performed and a database of the results was generated for comparisons. Literature has documented the effects of compound angle holes, and experiments more closely representing actual engine conditions have incorporated rib configurations in combination with crossflow for axial holes. However a void currently exists in literature, as there are no studies which have investigated the combined effects of internal crossflow with and without ribs for compound angle holes. Furthermore, no studies have examined any film cooling characteristics resulting from a rib configuration consisting of ribs which have been intersected by the film cooling holes. Adiabatic effectiveness was measured for all tests at blowing ratios from M=0.5 to 2.0 at a density ratio of DR=1.5. Film cooling holes were inclined at an angle of α=30° and spaced at a distance of p=6.25d.

The addition of a smooth-walled internal crossflow channel resulted in enhanced peak adiabatic effectiveness measurements when compared to the standard plenum configuration. Plenum-fed coolant holes had lower effectiveness values for all blowing ratios tested except the lowest case at M=0.50. The contour plots and laterally averaged effectiveness measurements generally indicated that greater separation with less jet reattachment contributed to the decreased effectiveness levels for the plenum configuration. The formation of beneficial in-hole vortices and a more skewed exit jet

96

profile for the crossflow case may have contributed to increased coolant adherence to the surface and subsequent effectiveness gains.

Similar to the performance when using a plenum inlet, peak effectiveness levels for the no-ribs crossflow case occurred at M=0.75. Effectiveness increased with increasing blowing ratio for M<0.75 as a result of increased coolant mass exiting the holes and covering the surface. Decreasing effectiveness levels occurred for M>0.75 as a result of increasing jet separation. The counter crossflow case attained a significantly higher maximum effectiveness than the in-line crossflow case, perhaps counterintuitively given that the coolant for the counterflow case had to make a much more severe turn into the cooling hole inlet. However, the counter crossflow case was also much more sensitive to blowing ratio and experienced steep declines in effectiveness following the optimal blowing ratio range, whereas the in-line case exhibited more sustained levels of effectiveness throughout the blowing ratios tested. The physical manifestations of the higher peak effectiveness values were seen in the jet profile contour plots, where the jet was considerably wider and traveled further downstream. It is possible that the increased separation region formed due to the higher turning angle of the coolant into the hole resulted in low momentum fluid exiting from the downstream portion of the hole, thereby allowing coolant to adhere better to the surface. Further examination of the jet contour plots would seem to validate this assumption. The counter crossflow contours exhibited less spanwise movement, indicating lower localized coolant momentum near the surface.

The addition of ribs generally decreased effectiveness levels for M>0.50 when compared to the no-ribs crossflow case. The no-ribs counter crossflow case had significantly higher peak effectiveness levels compared to all configurations. Even when considering the worse performing no-ribs case with in-line crossflow, all rib configurations but one either had similar or worse peak effectiveness levels. The rib

configuration that had the best peak effectiveness levels amongst all rib configurations and had better peak performance compared to the no-ribs in-line case was the perpendicular ribs, counterflow case. Examination of its pre-rib contour jet revealed striking similarities to the highest performing no-ribs counter jet, exhibiting skewed contours that none of the other jets possessed. It is possible that the highly skewed contours were caused by complex vortical structures originating from cooling hole inlet conditions.

Rib configurations containing ribs oriented in such a way as to deflect coolant towards the direction of mainstream flow performed better than the backwards deflecting ribs. Forward ribs also exhibited more sensitivity to blowing ratio than their counterparts. However, no other generalizations can be made to correlate film cooling effectiveness with hole location (pre- or post-rib) or direction of crossflow (counter or in-line crossflow) in relation to the hole. Variances in adiabatic effectiveness for the different configurations are most likely due to a combination of conditions. These may include variances in internal local pressure, internal channel flow fields, in-hole vortical structures, and exit velocity profiles. The latter two conditions are most likely strongly influenced by the development of the former two conditions.

In actual gas turbine blade construction, blade casting and hole tolerances may sometimes result in holes which intersect ribs. This study attempted to replicate such a circumstance by testing a rib configuration, termed aligned, over-holes, in which holes were partially drilled through ribs. This configuration demonstrated that a hole which intersects a rib still maintains moderate levels of effectiveness. Furthermore, the configuration's peak effectiveness levels were similar to the standard aligned rib configuration.

This study demonstrates that peak effectiveness can be attained through the optimization of crossflow direction relative to the compound angle direction and/or rib configuration. If a certain crossflow direction is known to augment effectiveness, gas turbine designers can use this knowledge to their benefit. Blades and vanes have serpentine passageways, meaning that the relative orientation of the crossflow to a compound hole will not always remain the same and will, in fact, alternate from one internal pass to the next. As a result, gas turbine designers can implement two different hole orientations, each a mirror-image of the other about the streamwise x/d axis, across the vane or blade to take full advantage of the crossflow. Lastly, significant differences in effectiveness as a result of crossflow direction for the no-ribs and perpendicular ribs were observed in this study, verifying the importance of hole inlet conditions in film cooling experiments.

4.2 RECOMMENDATIONS FOR FUTURE WORK

This study has investigated the end results of crossflow in combination with compound angled film cooling holes but cannot definitively provide the cause of the results. Studies, including this one, have stated that film cooling protection of the turbine blade can be optimized, and optimization requires an understanding of the relative importance of testing conditions, parameters, and geometries. Internal PIV flow field measurements and internal pressure readings would be valuable to isolate the characteristics responsible for the higher performing counter crossflow no-ribs and perpendicular ribs configurations. As these two tests contain some of the more valuable data, repeat tests for both crossflow cases should be conducted to verify their measurements. Local internal pressure measurements for pre- and post-rib holes would furthermore be useful in understanding the effect of ribs on hole-to-hole blowing ratio

variations. Designs could then address those characteristics and run variations on them for further experimentation. External flow field measurements could yield insights into the jet exit profile and the significance of downstream jet flow structures.

Additionally, perpendicular crossflow is representative of internal turbine blade cooling. Selected configurations from this study could be run in co- and counter-crossflow arrangements representative of vanes and compared to the results found in this study. A matched Biot study could be conducted to quantify the overall effects of implementing ribs in an attempt to determine if gas turbine blade or vane design would derive more benefit from using smooth-walled internal passageways.

Appendix A

This appendix contains pictures of the channel construction.

A.1: Picture of disassembled channel with silicone cord stock o-ring.
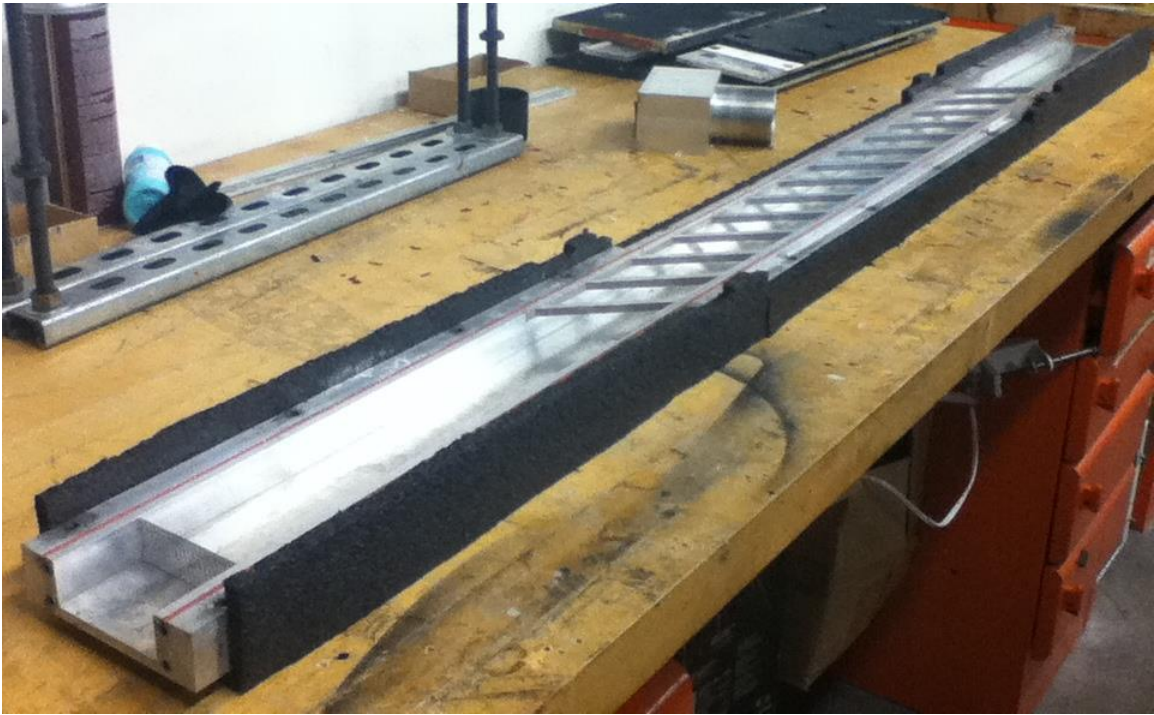
Figure A.2: Channel with rib plate

Appendix A.3.: Internal view of channel including the internal flow straightening screen

Appendix B

This appendix contains additional graphs concerning boundary conditions verification.
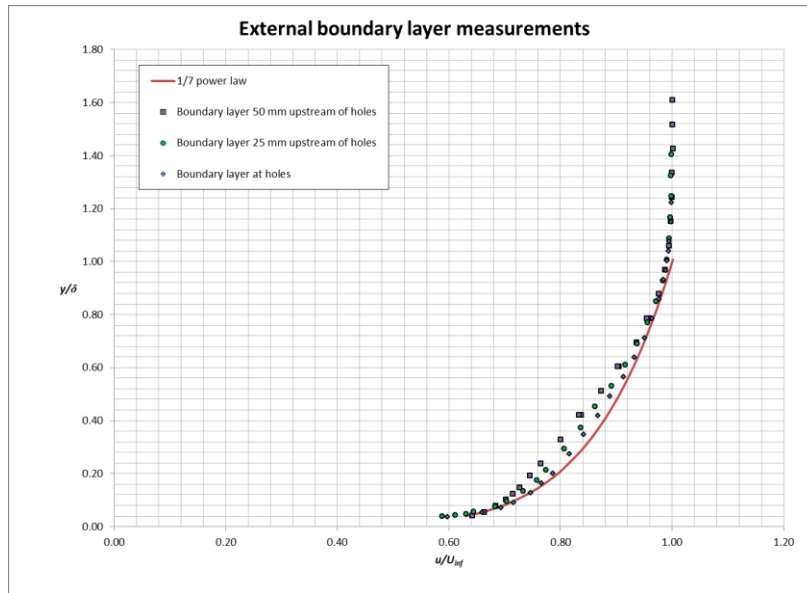
B.1: Boundary layer measurements at different streamwise locations
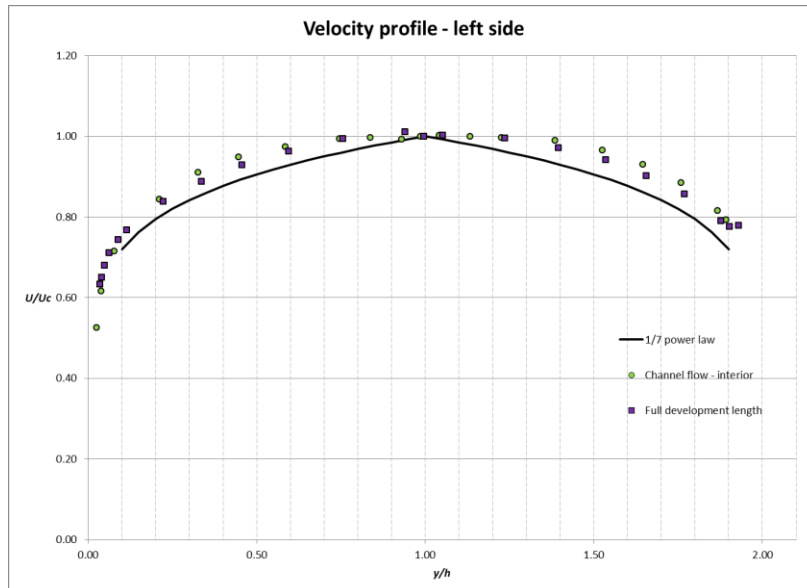
B.2: Internal channel velocity profile - left side

103

Appendix C

This appendix contains additional laterally averaged data and a contour plot depicting conduction correction zones for the aligned, over-holes case.
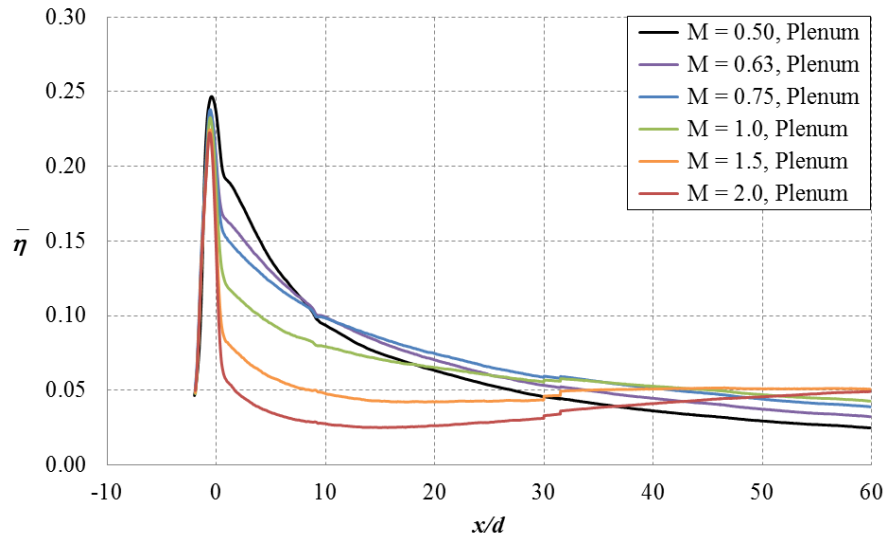
C.1: Laterally averaged adiabatic effectiveness curves for plenum case.
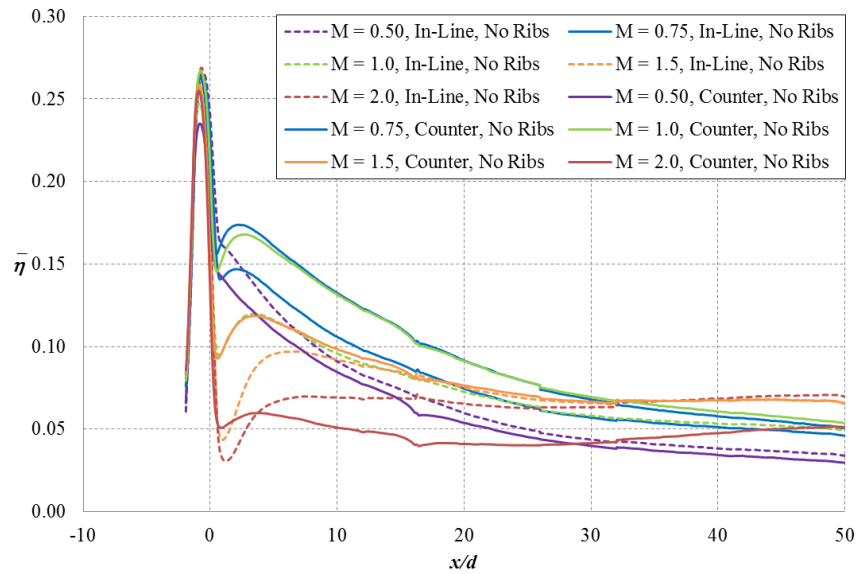
C.2: Laterally averaged adiabatic effectiveness curves for alternate crossflow directions - no ribs case.
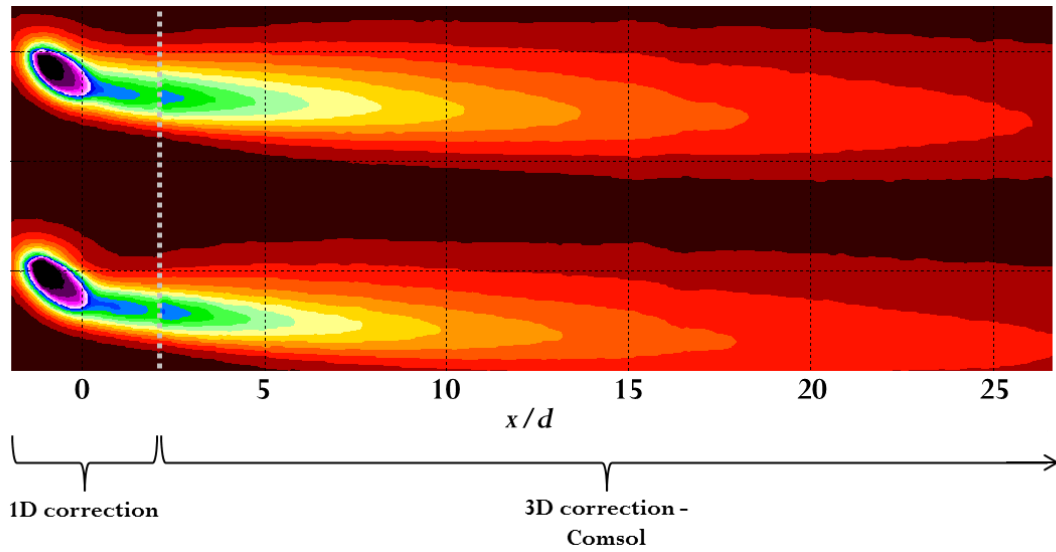
C.3: Conduction corrections applied to streamwise *x/d* ranges - aligned, over-holes case.
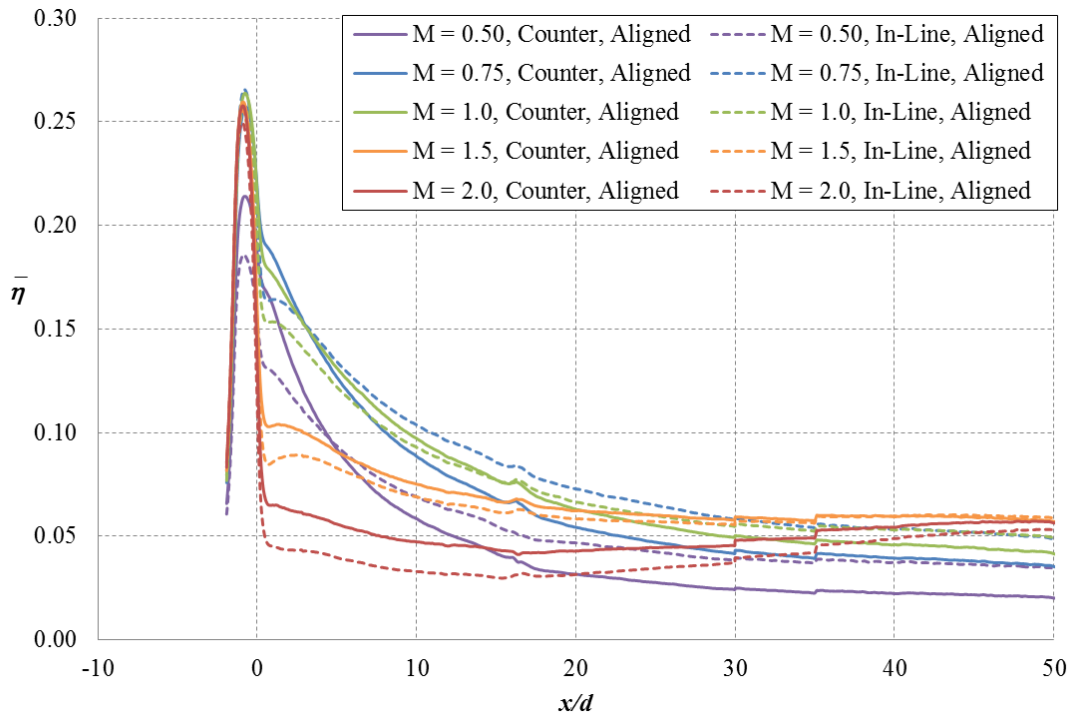
C.4: Laterally averaged adiabatic effectiveness curves for alternate flow directions - aligned case.

105
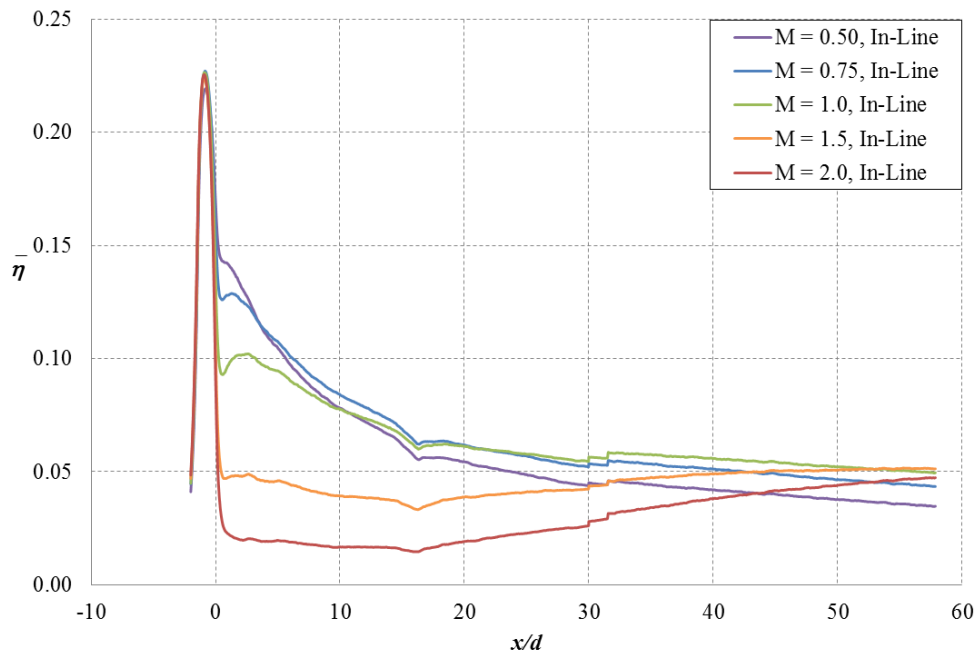
C.5: Laterally averaged adiabatic effectiveness curves for in-line crossflow direction - aligned, over-hole case
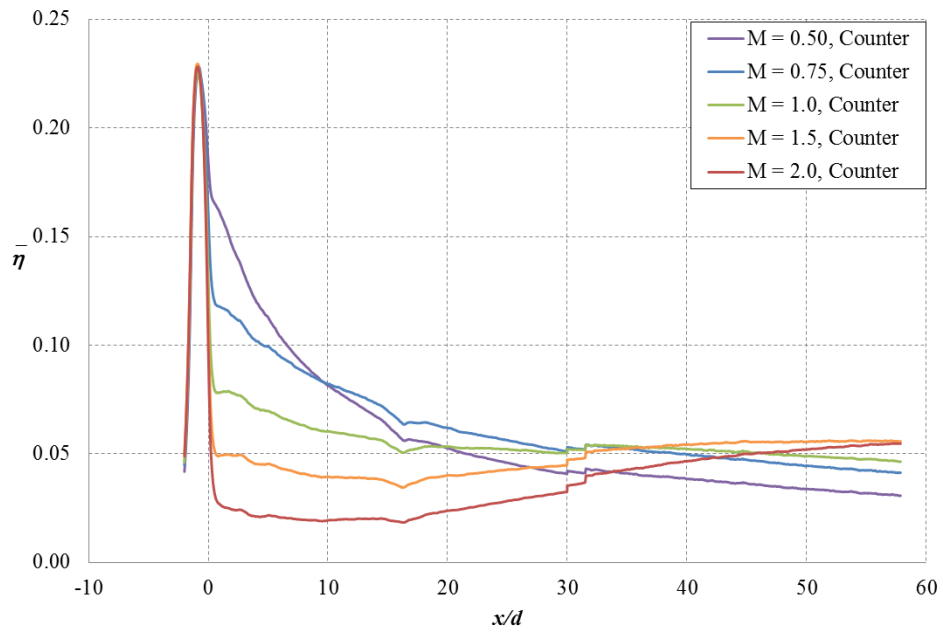
C.6: Laterally averaged adiabatic effectiveness curves for counter crossflow direction - aligned, over-hole case

106

Appendix D

This appendix contains total uncertainty analyses of blowing ratios and coolant mass flow rates.

Table D.1: Blowing ratio total uncertainty at M=0.50

Measured Parameter	Nominal Value	Measurement Uncertainty	Elemental Uncertainty
Cooling Hole Diamater, d_h (mm)	5.0	0.127	0.0245
Venturi Discharge Coefficient, $C_{d,V}$	0.953	0.0043	0.0394
Orifice Discharge Coefficient, $C_{d,o}$	0.61	0.0012	0.0185
Orifice Contraction Diameter, d_o (mm)	27.94	0.01	0.0072
Venturi Throat Diameter, d_V (mm)	36.83	0.01	0.0063
Mainstream Dynamic Pressure, P_{dyn} (Pa)	100.9	0.9	0.0022
Orifice Pressure Drop, ΔP_o (Pa)	870.9	0.42	0.0022
Orifice Inlet Coolant Temperature, T_o (K)	193.0	0.1	0.0012
Mainstream Temperature, T_∞ (K)	305.0	0.6	0.0005
Venturi Inlet Coolant Temperature, T_V (K)	220.0	0.1	0.0010
Venturi Pipe Diameter, $d_{p,V}$ (mm)	52.18	0.005	0.0006
Atmospheric Pressure, P_{atm} (Pa)	101350	500	0.0003
Orifice Pipe Diamater, $d_{p,o}$ (mm)	52.24	0.005	0.0002
Venturi Pressure Drop, ΔP_V (Pa)	-285.0	0.62	0.0000
Venturi Inlet Gage Pressure, P_V (Pa)	-285	0.62	0.0000
Orifice Inlet Gage Pressure, P_o (Pa)	1140	0.48	0.0000
Calculated M	**0.50**		
Uncertainty, δM	**0.05**		
Percent Uncertainty, $\delta M/M$	**10.7%**		

Table D.2: Blowing ratio total uncertainty at *M*=2.00

Measured Parameter	Nominal Value	Measurement Uncertainty	Elemental Uncertainty
Cooling Hole Diamater, d_h (mm)	5.0	0.127	0.0979
Venturi Discharge Coefficient, $C_{d,V}$	0.953	0.0043	0.0326
Orifice Discharge Coefficient, $C_{d,o}$	0.61	0.0012	0.0185
Orifice Contraction Diameter, d_o (mm)	27.94	0.01	0.0072
Venturi Throat Diameter, d_V (mm)	36.83	0.01	0.0052
Mainstream Dynamic Pressure, P_{dyn} (Pa)	100.9	0.9	0.0090
Orifice Pressure Drop, ΔP_o (Pa)	866.9	0.42	0.0022
Orifice Inlet Coolant Temperature, T_o (K)	193.0	0.1	0.0012
Mainstream Temperature, T_∞ (K)	305.0	0.6	0.0020
Venturi Inlet Coolant Temperature, T_V (K)	220.0	0.1	0.0008
Venturi Pipe Diamater, $d_{p,V}$ (mm)	52.18	0.005	0.0005
Atmospheric Pressure, P_{atm} (Pa)	101350	500	0.0004
Orifice Pipe Diamater, $d_{p,o}$ (mm)	52.24	0.005	0.0002
Venturi Pressure Drop, ΔP_V (Pa)	-317.0	0.62	0.0000
Venturi Inlet Gage Pressure, P_V (Pa)	-317	0.62	0.0000
Orifice Inlet Gage Pressure, P_o (Pa)	1610	0.48	0.0000
Calculated *M*	**2.00**		
Uncertainty, δM	**0.11**		
Percent Uncertainty, $\delta M/M$	**5.4%**		

Table D.3: Coolant mass flow rate total uncertainty at *M*=0.50

Measured Parameter	Nominal Value	Measurement Uncertainty	Elemental Uncertainty
Atmospheric Pressure, P_{atm} (Pa)	101350.0	500	2.17E-06
Orifice Inlet Gage Pressure, P_o (Pa)	1140.0	0.5	5.10E-08
Orifice Pressure Drop, ΔP_o (Pa)	870.9	0.4	5.25E-06
Venturi Inlet Gage Pressure, P_V (Pa)	-285.0	0.6	6.32E-08
Venturi Pressure Drop, ΔP_V (Pa)	100.1	0.4	4.01E-05
Orifice Inlet Coolant Temperature, T_o (K)	193.0	0.1	2.82E-06
Venturi Inlet Coolant Temperature, T_V (K)	220.0	0.1	2.34E-06
Orifice Discharge Coefficient, $C_{d,o}$	0.6	0.001	4.36E-05
Venturi Discharge Coefficient, $C_{d,V}$	1.0	0.004	9.29E-05
Orifice Contraction Diameter, d_o (mm)	27.9	0.01	1.70E-05
Orifice Pipe Diamater, $d_{p,o}$ (mm)	52.2	0.01	3.72E-07
Venturi Throat Diameter, d_V (mm)	36.8	0.01	1.49E-05
Venturi Pipe Diamater, $d_{p,V}$ (mm)	52.2	0.01	1.30E-06
Blowing Ratio *M*	0.50		
Calculated m_c (g/s)	**1.18**		
Uncertainty, δm_c (g/s)	**0.11**		
Percent Uncertainty, δm_c	**9.5%**		

Table D.4: Coolant mass flow rate total uncertainty at *M*=2.00

Measured Parameter	Nominal Value	Measurement Uncertainty	Elemental Uncertainty
Atmospheric Pressure, P_{atm} (Pa)	101350.0	500	1.07E-05
Orifice Inlet Gage Pressure, P_o (Pa)	1610.0	0.5	5.08E-08
Orifice Pressure Drop, ΔP_o (Pa)	866.9	0.4	5.28E-06
Venturi Inlet Gage Pressure, P_V (Pa)	-317.0	0.6	5.24E-08
Venturi Pressure Drop, ΔP_V (Pa)	68.6	0.4	4.84E-05
Orifice Inlet Coolant Temperature, T_o (K)	193.0	0.1	2.82E-06
Venturi Inlet Coolant Temperature, T_V (K)	220.0	0.1	1.94E-06
Orifice Discharge Coefficient, $C_{d,o}$	0.6	0.001	4.36E-05
Venturi Discharge Coefficient, $C_{d,V}$	1.0	0.004	7.70E-05
Orifice Contraction Diameter, d_o (mm)	27.9	0.01	1.70E-05
Orifice Pipe Diamater, $d_{p,o}$ (mm)	52.2	0.01	3.72E-07
Venturi Throat Diameter, d_V (mm)	36.8	0.01	1.23E-05
Venturi Pipe Diamater, $d_{p,V}$ (mm)	52.2	0.01	1.08E-06
Blowing Ratio *M*	2.00		
Calculated m_c (g/s)	**4.72**		
Uncertainty, δm_c (g/s)	**0.10**		
Percent Uncertainty, δm_c	**2.2%**		

BIBLIOGRAPHY

Adami, P., Martelli, F., Montomoli, F., Saumweber, C. "Numerical Investigation of Internal Crossflow Film Cooling." *ASME Turbo Expo.* Amsterdam, 2002.

Agata, Y., Takahashi, T., Sakai, E., Nishino, K. "Effect of Orientation of Internal Turbulence Promoting Ribs on Flow Characteristics for Film Cooling." *Thermal Science and Technology* 8, no. 1 (2013): 15-27.

Agata, Y., Takahashi, T., Sakai, E., Nishino, K. "Effects of Turbulence Promoters of Gas Turbine Blades on Film Cooling Performance." *Thermal Science and Technology* 7, no. 4 (2012): 603-618.

Andreopoulos, J., Rodi, W. "Experimental Investigation of Jets in a Crossflow." *Fluid Mechanics* 138 (1984): 93-127.

Bons, J.P., MacArthur, C.D., Rivir, R.B. "The Effect of High Freestream Turbulence on Film Cooling Effectiveness." ASME Paper 94-GT-51, 1994.

Boyd, E. J. "Parameters that Affect Shaped Hole Film Cooling Performance and the Effect of Density Ratio on Heat Transfer Coefficient Augmentation." Dissertation, The Universtiy of Texas at Austin, 2014.

Brauckmann, D., von Wolfersdorf, J. "Influence of Compound Angle on Adiabatic Film Cooling Effectiveness and Heat Transfer Coefficient for a Row of Shaped Film Cooling Holes." *ASME Turbo Expo.* Reno-Tahoe, 2005.

Bunker, S. R., Bailey, J. C. "Film Cooling Discharge Coefficient Measurements in a Turbulated Passage With Internal Crossflow." *Turbomachinery* 123 (2001): 774-780.

Burd, S. W., Simon, T. W. "The Influence of Coolant Supply Geometry on Film Coolant Exit Flow and Surface Adiabatic Effectiveness." *Proceedings of the 1997 ASME Turbo Expo.* 1997.

Casarsa, L., Arts, T. "Experimental Investigation of the Aerothermal Performance of a High Blockage Rib-Roughened Cooling Channel." *Turbomachinery* 127 (2005): 580-588.

Chanteloup, D. Bolcs, A. "Experimental Investigation of Heat Transfer in Two-Pass Coolant Pasages With Ribs and Film Cooling Hole Ejection." *ASME Design Engineering Technical Conferences and Computer and Information in Engineering Conference.* Montreal, 2002.

Chen, Y., Nikitopoulos, D.E., Hibbs, R., Acharya, S., Myrum, T.A. "Detailed Mass Transfer Distribution in a Ribbed Coolant Passage with a 180° Bend." *Heat and Mass Transfer* 43 (2000): 1479-1492.

Crabb, D., Durao, D. F. G., Whitelaw, J. H. "A Round Jet Normal to a Crossflow." *Fluids Engineering* 103 (1981): 142-152.

Cukurel, B., Selcan, C., Arts, T. "Film Cooling Extraction Effects on the Aero-Thermal Characteristics of Rib Roughened Cooling Channel Flow." *Turbomachinery* 135 (2013).

Dees, J. E. "Experimental Measurements of Conjugate Heat Transfer on a Scaled-up Gas Turbine Airfoil with Realistic Cooling Configuration." Dissertation, The University of Texas at Austin, 2010.

Ekkad, S. V., Zapata, D., Han, J. C. "Film Effectiveness Over a Flat Surface with Air and CO2 Injection Through Compound Angle Holes Using a Transient Liquid Crystal Image Method." *Turbomachinery* 119 (1997): 587-593.

Fawcett, R. J., Wheeler, A. P. S., He, L., Taylor, R. "Experimental Investigation Into Unsteady Effects on Film Cooling." *Turbomachinery* 134 (2012).

Feng, Z., Dou, Z., Wang, J. "Numerical Investigations of Cooling Enhancement With Internal Ribs and External Coolant Film." *Proceedings of ASME Turbo Expo.* Copenhagen, 2012.

Goldstein, R. J. *Fluid Mechanics Measurements.* 2nd. Washington, D.C.: Taylor & Francis, 1996.

Gritsch, M., Saumweber, C., Schulz, A., Wittig, S., Sharp, E. "Effect of Internal Coolant Crossflow Orientation on the Discharge Coefficient of Shaped Film-Cooling Holes." *Turbomachinery* 122 (2000): 146-152.

Gritsch, M., Schulz, A., Wittig, S. "Adiabatic Wall Effectiveness Measurements of Film-Cooling Holes With Expanded Exits." *Turbomachinery* 120 (1998).

Gritsch, M., Schulz, A., Wittig, S. "Effect of Crossflows on the Discharge Coefficient of Film Cooling Holes With Varying Angles of Inclination and Orientation." *Turbomachinery* 123 (2001): 781-787.

Gritsch, M., Schulz, A., Wittig, S. "Effect of Internal Coolant Crossflow on the Effectiveness of Shaped Film-Cooling Holes." *Turbomachinery* 125 (2003): 547-554.

Hale, C. A., Plesniak, M. W., Ramadhayani, S. "Film Cooling Effectiveness for Short Film Cooling Holes Fed by a Narrow Plenum." *Turbomachinery* 122 (2000): 553-557.

Han, J. C., Park, J. S., Lei, C. K. "Heat Transfer Enhancement in Channels With Turbulence Promoters." *Engineering for Gas Turbines and Power* 107 (1985): 628-635.

Hay, N., Henshall, S. E., Manning, A. "Discharge Coefficients of Holes Angled to the Flow Direction." *Turbomachinery* 116 (1994): 92-96.

Hay, N., Lampard, D., Benmansour, S. "Effect of Crossflows on the Discharge Coefficient of Film Cooling Holes." *Engineering for Power* 105 (1983): 243-248.

Heneka, C., Schulz, A., Bauer, H. "Effect of Internal Rib Configurations on the Discharge Coefficient of a 30°-Inclined Film Cooling Hole." *Heat Transfer Research* 41, no. 7 (2010): 769-786.

Kadotani, K., Goldstein, R. J. "On the Nature of Jets Entering a Turbulent Flow, Part A. Jet-Mainstream Interaction." *Engineering for Power* 101 (1979): 459-465.

Kelly, G. B., Bogard, D. G. "An Investigation of the Heat Transfer for Full-Coverage Film Cooling." ASME Paper GT2003-38716, 2003.

Kissel, H., Weigand, B., von Wolfersdorf, J., Neumann, S. O. "An Experimental and Numerical Investigation of the Effect of Cooling Channel Crossflow on Film

Cooling Performance." *Conference Proceedings of ASME Turbo Expo.* Montreal, 2007.

Kline, S. J., McClintock, F. A. "Describing Uncertainties in Single-Sample Experiments." *Mechanical Engineering* 75, no. 1 (1953): 3-8.

Kohli, A., Bogard, D. G. "Adiabatic Effectiveness, Thermal Fields, and Velocity Fields for Film Cooling With Large Angle Injection." *Turbomachinery* 119 (1997): 352-358.

Kunze, M., Vogeler, K. "Flow Field Investigations on the Effect of Rib Placement in a Cooling Channel With Film-Cooling." *Turbomachinery* 136 (2014).

Launder, B. E., York, J. "Discrete Hole Cooling in the Presence of Free Stream Turbulence and Strong Favorable Pressure Gradient." *Heat and Mass Transfer* 17 (1974): 1403-1409.

Le Brocq, P. V., Launder, B. E., Priddin, C. H. "Discrete Hole Injection as a Means of Transpiration Cooling: An Experimental Study." *Proc. Instn. Mechanical Engineers* 17 (1973): 149-157.

Lerch, A., Schiffer, H., Klaubert, D. "Impact on Adiabatic Film Cooling Effectiveness Using Internal Cyclone Cooling." *Proceedings of ASME Turbo Expo.* Vancouver, 2011.

Leylek, J. H., Zerkle, R. D. "Discrete-Jet Film Cooling: A Comparison of Computuational Results With Experiments." *Turbomachinery* 116 (1994): 358-368.

Ligrani, P. M., Ciriello, S., Bishop, D. T. "Heat Transfer, Adiabatic Effectiveness, and INjectant Distributions Downstream of a Single Row and Two Staggered Rows of Compound Angle Film-Cooling Holes." *Turbomachinery* 114 (1992): 687-700.

Ligrani, P. M., Wigle, J. M., Jackson, S. M. "Film-Cooling From Holes With Compound Angle Orientations: Part 2 - Results Downstream of a Single Row of Holes With 6d Spanwise Spacing." *Heat Transfer* 116 (1994): 353-362.

Lutum, E., Johnson, B. V. "Influence of the Hole Length-to-Diameter Ratio on Film Cooling With Cylindrical Holes." *Turbomachinery* 121 (1999): 209-216.

Mayhew, J. E., Baughn, J. W., Byerley, A. R. "The Effect of Freestream Turbulence on Film Cooling Adiabatic Effectiveness." *Heat and Fluid Flow* 24 (2003): 669-679.

—. "The Effect of Freestream Turbulence on Film Cooling Heat Transfer Coefficient and Adiabatic Effectiveness Using Compound Angle Holes." *Proceedings of ASME Turbo Expo.* Vienna, 2004.

McClintic, J. "Experimental Investigation of Overall Effectiveness and Coolant Jet Interactions on a Fully Cooled C3X Turbine Vane." Master's Thesis, University of Texas at Austin, 2013, 1-13.

McClintic, J. W., Klavetter, S. R., Anderson, J. B., Winka, J. R., Bogad, D. G., Dees, J. E., Laskowski, G. M., Briggs, R. "The Effect of Internal Cross-Flow on the Adiabatic Effectiveness of Compound Angle Film Cooling Holes." *ASME Turbo Expo.* Dusseldorf, 2014.

McGovern, K. T., Leylek, J. H. "A Detailed Analysis of Film Cooling Physics: Part II - Compound-Angle Injection With Cylindrical Holes." *Journal of Turbomachinery* 122 (2000): 113-120.

Montomoli, F., Massini, M., Salvadori, S., Martelli, F. "Geometrical Uncertainty and Film Cooling: Fillet Radii." *Turbomachinery* 134 (2012).

Papell, S. "Vortex Generating Flow Passage Design for Increased Film-Cooling Effectiveness and Surface Coverage." NASA Technical Memorandum, 1984.

Peng, W., Jiang, P. X. "Experimental Heat Transfer: A Journal of Thermal Energy Generation, Transport, Storage, and Conversion." *Experimental Heat Transfer* 25 (2012): 282-300.

Peterson, S. D., Plesniak, M. W. "Short-Hole Jet-in-Crossflow Velocity Field and its Relationship to Film-Cooling Performance." *Experiments in Fluids* 33 (2002): 889-898.

Pietrzyk, J. R., Bogard, D. G., Crawford, M. E. "Hydrodynamic Measurements of Jets in Crossflow for Gas Turbine Film Cooling Applications." *Turbomachinery* 111 (1989): 139-145.

Sakai, E., Takahashi, T. "Experimental and Numerical Study on Effects of Turbulence Promoters on Flat Plate Film Cooling." *Proceedings of ASME Turbo Expo.* Vancouver, 2011.

Saumweber, C., Schulz, A. "Comparison of the Cooling Performance of Cylindrical and Fan-Shaped Cooling Holes with Special Emphasis on the Effect of Internal Coolant Cross-Flow." *Proceedings of the ASME Turbo Expo.* Berlin, 2008.

Schmidt, D. L., Sen, B., Bogard, D. G. "Film Cooling With Compound Angle Holes: Adiabatic Effectiveness." *Turbomachinery* 118 (1996): 807-813.

Sen, B., Schmidt, D. L., Bogard, D. G. "Film Cooling With Compound Angle Holes: Heat Transfer." *Turbomachinery* 118 (1996): 799-806.

Shen, J. R., Wang, Z., Ireland, P. T., Jones, T. V., Byerley, A. R. "Heat Transfer Enhancement Within a Turbine Blade Cooling Passage Using Ribs and Combinations of Ribs With Film Cooling Holes." *Turbomachinery* 118 (1996): 428-434.

Sinha, A. K., Bogard, D. G., Crawford, M. E. "Film-Cooling Effectiveness Downstream of a Single Row of Holes With Variable Density Ratio." *Turbomachinery* 113 (1991): 442-449.

Taslim, M. E., Khanicheh, A. "Film Effectiveness Downstream of a Row of Compound Angle Film Holes." *Heat Transfer* 127 (2005): 434-440.

Thole, K. A., Gritsch, M., Schulz, A., Wittig, S. "Effect of a Crossflow at the Entrance to a Film-Cooling Hole." *Fluids Engineering* 119 (1197): 533-540.

Walters, D. K., Leylek, J. H. "A Detailed Analysis of Film-Cooling Physics: Part I - Streamwise Injection With Cylindrical Holes." *Turbomachinery* 122 (2000): 102-112.

Wilfert, G., Wolff, S. "Influence of Internal Flow on Film Cooling Effectiveness." *Turbomachinery* 122 (2000): 327-333.

Xiangyun, L., Tao, Z., Ding, S., Xu, G. "Experimental Investigation of Heat Transfer
Characteristics in a Variable Cross-Sectioned Two-Pass Channel With Combined
Film Cooling Holes and Inclined Ribs." *Applied Thermal Engineering* 50 (2013):
1186-1193.